ABSTRACT

Title of Dissertation: SPATIOTEMPORAL NONLINEAR OPTICAL EFFECTS IN MULTIMODE FIBERS

Sai Kanth Dacha
Doctor of Philosophy, 2022

Dissertation Directed by: Professor Thomas E. Murphy
Department of Electrical and Computer Engineering

The advent of the optical fiber in the second half of the 20th century has had numerous consequences not only for the advancement of telecommunication and information transfer technologies, but also for humanity as a whole. At the time of writing of this thesis, we live in a world that is defined by unprecedented and unparalleled access to information made possible by fiber optic cables that line the ocean beds. As the world becomes increasingly reliant upon the internet, the demand for access is outgrowing the pace at which the capacity of our fiber optic networks can be scaled up. In the past decade, a consensus has emerged among researchers in academia and the industry that we are now approaching the fundamental classical capacity limit of a conventional single mode fiber, namely the Shannon limit. This has spurred interest in multimode fibers that allow for hundreds of spatial modes to co-propagate, potentially allowing for at least an order of magnitude increase in capacity per fiber.

While multiplexing in the spatial domain has the potential to offer significantly higher capacities, linear and nonlinear mixing between the spatial modes of a fiber are expected to play

an important role in determining the capacity and performance of spatially multiplexed telecommunication systems. So far, multimode fibers have mostly been relegated to low-power short-distance links, as a result of which nonlinear propagation effects in the presence of multiple spatial modes has received relatively little attention. This thesis adds to a growing body of literature that is increasingly interested in uncovering the physics of multimodal propagation in the nonlinear regime.

Although the need for spatial multiplexing is important factor driving research interest in this topic, experiments in recent years have revealed a plethora of complex spatiotemporal nonlinear phenomena occurring in multimode fibers, including Kerr-induced beam self-cleaning, parametric instability processes and the existence of multimode solitons. This has sparked great interest in understanding multimodal nonlinearity from a fundamental and applied physics perspective. Nonlinear multimode fiber optics is also of central importance for the development of high power fiber-coupled lasers as the larger core size of multimode fibers allow for far higher power throughput than current state-of-the-art lasers based on single mode fibers.

Most literature reported thus far in multimodal nonlinear optics focuses on complex phenomena occurring when hundreds of spatial modes co-propagate in the nonlinear regime. While that has proven to be a fascinating field of study, there have not been many studies on experimental investigation of intermodal nonlinear effects in the presence of a small number of spatial modes. Furthermore, nonlinear phenomena in multimode fibers are 'spatiotemporal' in nature, meaning that the spatial and time-domain waveforms are intertwined, and the two degrees of freedom cannot be separated. Conventional measurement techniques are not capable of resolving such a multimodal beam in space and time simultaneously. Finally, most research involving nonlinear optical effects has thus far focused on linearly polarized modes in conventional fibers,

and nonlinear effects involving vector orbital angular momentum modes remains relatively understudied.

In this thesis, we seek to study nonlinear optical effects involving a small number of selectively excited scalar as well as vector spatial modes, and to develop experimental techniques capable of resolving the output in both space, frequency and time. To this end, we design, prototype and fabricate devices and methods aimed at exciting a small number of spatial modes of a fiber. In particular, we adopt methods from integrated photonics such as focused ion beam milling and metasurface devices to selectively excite modes of a fiber in an efficient manner. Spatial and temporal resolution of the output beam is achieved by the development of a new technique that involves raster-scanning of a near-field scanning optical microscopy probe, coupled with a high speed detector, along the output end-face of the fiber.

Using these methods, we uncover and report our observations of spatiotemporal nonlinear phenomena that are unique to multimodal systems. We first demonstrate nonlinear intermodal interference of radially symmetric modes in step-index and parabolic index fibers. We then apply the same spatiotemporal measurement technique to observe the Kerr-induced beam self-cleaning phenomenon in a parabolic index fiber. And finally, we discuss our discovery of a spin-orbit coupled generalization of the well-known nonlinear polarization rotation phenomenon.

SPATIOTEMPORAL NONLINEAR OPTICAL EFFECTS IN MULTIMODE FIBERS

by

Sai Kanth Dacha

Dissertation submitted to the Faculty of the Graduate School of the
University of Maryland, College Park in partial fulfillment
of the requirements for the degree of
Doctor of Philosophy
2022

Advisory Committee:
Prof. Thomas E. Murphy, Chair/Advisor
Prof. Phillip A. Sprangle
Dr. Kenneth J. Ritter
Prof. Mohammad Hafezi
Dr. Giuliano Scarcelli

Preface

As its title suggests, this is a thesis on the study of spatiotemporal nonlinear optical effects in multimode fibers. In order to describe a spatiotemporal phenomenon in a meaningful way, it is desirable to be able to use graphic formats that are spatiotemporal in nature as well, such as videos. Unfortunately, despite all the scientific and technological progress humanity has made during the past half a century, we have not yet solved the most pressing problem of all: the lack of a convenient, simple and universal method to embed videos and animations into PDFs.

As a result, the reader is advised to refer to the 'Supplementary Videos' published alongside this thesis, which are referenced throughout this thesis. Although we have included static images that show snapshots of simulated and experimentally observed spatiotemporal phenomena, the video format is very helpful in making sense of the phenomena that we describe.

This document is dedicated to my family.

"The audacity of hope."

Acknowledgments

Graduate school can often be an intimidating, difficult and sometimes lonely journey. It has certainly been that way many a time for me. When I moved to the United States back in 2016 to pursue my Ph.D., I was barely 21, knew very few people in this country, and had not a lot of exposure to the broader world outside of my very humble upbringing. The fact that I have made it to the finish line is a testament to the kindness and generosity of many that I am fortunate to have in my life.

First and foremost, I am extremely grateful to my advisor Professor Thomas Murphy. Tom has not only been an amazing supervisor, one of the best teachers I've seen in optics and a brilliant researcher, but perhaps most importantly, he has been a considerate and empathetic advisor and mentor. He has given me enormous freedom to shape every detail, big and small, of this research effort, while also providing excellent guidance throughout the process. Time and again, I have seen him strike a seemingly perfect balance between leading a world class nonlinear photonics research program, being an award-winning teacher, serving as director of a research institute at one of the world's best universities, serving the broader science community, and being an active dad; all while treating everyone with unmatched patience and humility. Thank you, Tom, for being an inspiration, for providing me with exciting opportunities, and for all else that you do.

Much thanks goes to the folks at the Laboratory for Physical Sciences: Ken Ritter, Tim Horton, Karen Grutter. Thank you for hosting my research, and for all the technical and non-

technical support that you have provided these past many years! Thank you in particular to Ken Ritter, for bearing with me through the numerous times that I knocked on his office/lab door to ask for advice and help on all things OAM. Thank you to all the current and former members of the Photonics Research Laboratory, you have all made this a very memorable experience: Steven, Matt Chin, Ramesh, Yigit, Mehdi, Martin, Gyan, Tom Butler, Sumi, Trisha, Kunyi, Sarvenaz, François, Jayaprakash and Nicole. Steven, Matt Chin, Gyan, Michael, Tom Butler: I will dearly miss our lunch sessions and banter. Ramesh: thank you for all your help with the chemical etching, and for taking photos of me in a cleanroom outfit!

The work that I present in this thesis would not have been possible without the support of our collaborators and technical infrastructure at the University of Maryland. Special thanks to Wenqi Zhu and Amit Agrawal (NIST) for fabricating a metasurface q-plate for us so quickly in COVID times! Thanks to Amit Agrawal also for wonderful career advice and mentorship. Thank you to Prof. Siddharth Ramachandran & OFS Fitel LLC for providing the ring-core fiber used in this work. Thank you to the LPS Cleanroom and Model Shop facilities and AIM Lab, in particular Dr. Jiancun Rao for all the help with the FIB. Thank you also to all the staff at UMD Physics and IREAP, in particular to Josiland Chambers, Taylor Prendergast, Vivian Lu, Cassandra Mendez, Jane Wang, and Meredith Pettit for all that you do.

I would like to thank my committee members Dr. Ken Ritter, Prof. Phillip Sprangle, Prof. Mohammad Hafezi and Dr. Giuliano Scarcelli for taking the time out of your busy schedules to provide valuable feedback on this thesis and to participate in my defense. Special thanks to Prof. Sprangle for the valuable and illuminating conversations on modulation instability. Thank you to Prof. Rajarshi Roy for his ever-positive presence and support throughout my Ph.D. Thank you to the members of IREAP-ROLE; working with you all has helped me understand academia in a

more meaningful way: Amitava, Daniel, Roxanne, Taylor, Heidi, Carlos, Kevin, Marc.

During the Summer and Fall of 2021, I had an incredible time working at Bell Labs. Although the work that I did there has not been included in this thesis, I have grown greatly as a researcher thanks to it. A big thank you to my mentor Dr. René-Jean Essiambre. I will miss the many long evenings that we spent in the lab sharing stories and debugging problems with the photon counter, and I hope that we will work together soon again. Thank you to Nick Fontaine, Andrea Blanco-Redondo, Haoshuo Chen, Roland Ryf and Yuanhang Zhang for making my time at Bell Labs such a memorable one.

I would be remiss if I did not mention the many amazing teachers that I have had the fortune of having throughout my educational career. Thank you in particular to Prof. Deepa Venkitesh (IIT Madras), Dr. Gabriele Vajente (Caltech), KRK sir and Jayanthi ma'am.

I have been very lucky to have had amazing friends throughout my life, many of who have played a continual role in helping me get across the finish line. Thank you in particular to Lauren, Ananya, Vandana, Yogesh, Steven, Sandeep, Tharun, Susmija, Matt Chin, Sujata, Priyanka, Ani, Anwesh, Shruti, Sahithya, Rahul, Aditi, Shagun, Abhishek, Bhupi, Anupam, Saketh, Bala, Sweta, Pranav, Anindita, Linette, Shifali, Kaustubh, Saumitran, Rohit, Avira, Arushi, Rohith, Anuraag, Kushal, Vinay, Julia and many others that I'm sure I have missed mentioning here. I am grateful for the many cats that I have had the fortune of knowing these past six years: Jane, Sunlight, Moonlight, Luna and Sky, and also Luna the dog.

Most of all, I would like to thank my family for their love and support throughout this journey. Thank you, in particular, to my mom, dad and sister for their unconditional and unwavering support, love, and sacrifice. This piece of scientific work, however humble it may be, would not be possible without you.

Table of Contents

List of Tables

List of Figures

Description of Supplementary Videos

Note 1: Supplementary Videos 1 & 2 were part of the following manuscript that we published: Sai Kanth Dacha et al., Optica 7, 1796-1803 (2020) ©Optical Society of America.

Note 2: Supplementary Videos 3 - 6 were part of the following manuscript that we published: Sai Kanth Dacha et al., Opt. Exp. Vol. 30, No. 11, 18481-18495 (2022) ©Optical Society of America

- **Supplementary Video 1**: Experimental data showing spatiotemporally resolved nonlinear pulse evolution for two linearly polarized radially symmetric modes excited in a few-mode fiber. Each time-varying "pixel" in the video results from an experimental acquisition of the time-domain waveform using a near-field scanning optical probe coupled with a single-mode fiber.

- **Supplementary Video 2**: Numerical simulation of nonlinear pulse evolution for two linearly polarized radially symmetric modes excited in a few-mode fiber, obtained by integrating the multimode nonlinear Schrödinger equations.

- **Supplementary Video 3**: Numerical simulation of nonlinear time-dependent rotation of an unequal superposition of the $L = \pm 10$ spin-orbit anti-aligned (SO_{aa}) modes of a hollow ring-core fiber, obtained by integrating the multimode nonlinear Schrödinger equations.

- **Supplementary Video 4**: Numerical simulation of nonlinear rotation of *time-averaged* lobe patterns resulting from an unequal superposition of the $L = \pm 10$ spin-orbit anti-aligned (SO_{aa}) modes of a hollow ring-core fiber, obtained by integrating the multimode nonlinear Schrödinger equations. Note the opposite directions of rotation for the dominant $L = -10$ SO_{aa} case (left graphic) vs the dominant $L = +10$ SO_{aa} case (right graphic).

- **Supplementary Videos 5, 6**: Experimentally measured power-dependent rotation of *time-averaged* lobe intensity patterns for unequal superpositions of the $L = \pm 10$ spin-orbit anti-aligned (SO_{aa}) modes of a hollow ring-core fiber. Suppl. Vid. 5 shows the dominant $L = -10$ SO_{aa} case, while Suppl. Vid. 6 shows the dominant $L = +10$ SO_{aa} case. The direction of rotation can be seen to be opposite in the two cases, in agreement with numerical simulation results shown in Suppl. Vid. 4.

List of Abbreviations

BEC	Bose-Einstein Condensate
CCD	Charge Coupled Device
CMOS	Complementary Metal-Oxide Semiconductor
DFT	Discrete Fourier Transform
DGD	Differential Group Delay
EDFA	Erbium-Doped Fiber Amplifier
EM	Electromagnetic
FFT	Fast Fourier Transform
FIB	Focused Ion Beam
FMF	Few Mode Fiber
FWM	Four Wave Mixing
GMMNLSE	Generalized Multimode Nonlinear Schrödinger Equations
GNLSE	Generalized Nonlinear Schrödinger Equation
GVD	Group Velocity Dispersion
GRIN	Graded Index
HG	Hermite Gaussian
HWP	Half Wave Plate
IMFWM	Intermodal Four Wave Mixing
LC	Liquid Crystal
LG	Laguerre Gaussian
LP	Linearly Polarized (or) Linear Polarizer
MCF	Multicore Fiber
MDM	Mode Division Multiplexing
MI	Modulation Instability
MMF	Multimode Fiber

MMNLFO	Multimode Nonlinear Fiber Optics
MOPA	Master Oscillator Power Amplifier
NLFO	Nonlinear Fiber Optics
NLSE	Nonlinear Schrödinger Equation
NPR	Nonlinear Polarization Rotation
NSOM	Near-field Scanning Optical Microscopy
OAM	Orbital Angular Momentum
OCT	Optical Coherence Tomography
PB	Pancharatnam-Berry
PBS	Polarizing Beam Splitter
PMF	Polarization Maintaining Fiber
QWP	Quarter Wave Plate
RCF	Ring Core Fiber
SAM	Spin Angular Momentum
SDM	Space Division Multiplexing
SEM	Scanning Electron Microscopy
SLM	Spatial Light Modulator
SMF	Single Mode Fiber
SNR	Signal-to-Noise Ratio
SOI	Spin-Orbit Interaction
SPM	Self Phase Modulation
SRS	Stimulated Raman Scattering
SSFM	Split-Step Fourier Method
SWE	Scalar Wave Equation
TE	Transverse Electric
TM	Transverse Magnetic
TEM	Transverse Electromagnetic
WDM	Wavelength Division Multiplexing
WGA	Weakly Guiding Approximation
XPM	Cross Phase Modulation

"Ετεή δε ουδέν ίδμεν, Εν βυθώ γαρ η αλήθεια"

"We know nothing in reality, for truth lies in an abyss"

— Democritus of Abdera (460 BCE to 370 BCE),

on the unknowability of objective reality from

subjective human perceptions alone.

A Reflection on Diversity and Inclusion in Academia

I grew up in an unremarkable part of a moderately large city in India. My upbringing was what one might describe as a typical lower-middle-class Indian upbringing of the late 90s and early 2000s, which is code for deep socioeconomic hardships and not a lot of hope. My sister and I were raised through what were particularly difficult times for my family. For nearly a decade (although he still continues to do this), my father had to work $10+$ hr days on all 7 days of the week just to make ends meet, while my mother handled our education and upbringing. Neither of my parents are college graduates, and they knew all too well the enormous disadvantage that my sister and I would be at later in life if they didn't invest in our education. And so they did, even if at the cost of them having to work with no weekends off, and even if it meant that we never got to travel or afford experiences of any kind. It goes without saying that I would not be here writing this document if not for their hard work, and if not for their investment in my education.

When I got into IIT Madras for my undergraduate studies, I thought that that would mark a completely new chapter for me and my family. It did, but it also didn't. You see, when you grow up for 17 years of your life in a mostly uninteresting environment but suddenly find yourself surrounded by some of the smartest students in the country that come from a wide range of backgrounds – many of who seem to be exceptionally smart and/or are from far more affluent backgrounds than yours, even if only relatively – you begin to question if you really belong in that new environment. That has been my experience anyway. "Surely I don't belong with all these smart kids that went to much better schools than I did and have seen much more of the world than I had, right? I mean, that kid already has a personal computer of his own and knows

Python programming. What good am I? Or that other kid that somehow already has many friends here and feels like he really belongs here. I certainly don't feel that way, so once again, do I *really* belong here?"

As has been my experience, these types of thoughts have stuck with me throughout my educational career. Be it at IIT Madras, at my undergraduate summer internship at Caltech, or my stint here at the University of Maryland. Although I suspect that the overarching question of belongingness is one that will continue to bother me wherever I go next, I have been incredibly fortunate to have met people – classmates, professors, staff – at all of these places that have helped me overcome these feelings, helped me feel like I belonged, and helped me grow as human being and as a researcher. Even here in the U.S., many academic departments host a fair number of Indian and other international students, postdocs and faculty members, and I am certain that that goes a long way in making international students such as myself feel more welcome.

My moving to the U.S., though, has also opened my eyes to the complex legacy of racial injustice and economic inequality in this country. As I learnt more and more about slavery, segregation, the historic oppression and underrepresentation of people of African descent, I began to understand better why it is that the people that I see in academic departments and at conferences don't look anything like the racially and ethnically diverse overall population of the U.S. I continue to find it a little strange that I see more people that have a similar "background" as mine (i.e. upper caste Hindu Indian) in American academia than I see black American academics. All of this has led me to not only question if I am complicit in perpetuating this problem, but it also made me realize the deep systemic barriers that prevent so many black students (and also other non-white folk) from succeeding in academia.

Admittedly, even at the time of writing of this thesis, I have only been part of American

academia for six years, which is not a lot of time, but in these years alone, this country has witnessed enormous unrest and activism against forces of discrimination, violence and oppression. And I always found it strange that so many of us academics as well as academic institutions get away with pretending that we are isolated from the rest of society, when in reality we are as much part of the problem as any other institution. To me, it was telling that it took the massive public unrest following the murder of George Floyd for academic institutions across the country – and across the world – to take the problems of underrepresentation and systemic barriers more seriously. Needless to say, racism extends well beyond academia and it is not for us to solve it by ourselves, but as people that part of educational institutions, we are well-situated to help address the problem in a meaningful way.

I am grateful that I got to pursue my graduate degree at the University of Maryland – among many other reasons because this is a place that has taken a number of initiatives to address these issues, and has been proactive about making people feel more welcome. However, much work remains to be done. I for one have been heartened to see that numerous departments and research institutes at UMD alone have set up committees and task forces to assess what steps can be taken to ensure that people of all socio-economic backgrounds succeed.

Although my struggle with belongingness may have had a different origin than a black student's struggle with it, and although my people (upper caste Indian) are seemingly far better represented in academia and elsewhere compared to many others, I have still known at an individual level what it's like to question if you would be missed if you left one day, and to wonder whether you will ever see as much success as others. I would not wish that on anyone, let alone the constant micro- (and sometimes overt) aggressions that black (and increasingly, east Asian) peers of mine seem to face. During the past two years, I have sought to be part of initiatives

that work toward making academic departments, institutes and research groups more welcoming and inclusive spaces. In particular, I want to mention IREAP-ROLE, which is a team of volunteer students, staff and faculty at UMD's Institute for Research in Electronics and Applied Physics (IREAP) that is working toward identifying and undertaking meaningful initiatives at the research institute level to make this a more inclusive place for underrepresented racial and gender minorities.

As a founding member of IREAP-ROLE, I have grown some as a human being and as a researcher. I have had the opportunity to work alongside many others from who I have learnt a great deal. Both through my interactions with my peers as well as through my time at IREAP-ROLE, I have come to appreciate the very many ways, big and small, in which students, staff and researchers of underrepresented races and genders face differential treatment, systemic injustices, and at times blunt racism and sexism. Through this work, I have come to understand the role of my own socioeconomic privileges in helping me get here today much better, and I received a platform from which to advocate for better treatment of the graduate student body overall while highlighting the many mental health and financial hardships faced by far too many of us. Although the makeup of the committee has been fairly diverse, none of us has had a lot of experience of organizing around this particular issue within the academic context, and so this has made for a learning experience for all of us involved.

The point of me writing all this in my Ph.D. thesis is to highlight not only the importance and urgency of the issue at hand, but also the long overdue initiatives that many are beginning to work on. Education is the roadway to opportunity and a better life for many, especially for those that come from communities that have not had the luxury of generational wealth or ample socio-economic status. In my personal experience, the privilege and fortune of having access to

decent education has unequivocally been a key enabler in helping me get here today.

I believe that as people that work in academia, we have not only a great responsibility but also a great opportunity to play a key role in helping address the many injustices that our friends and peers continue to face. Scientific research and modern university education are fundamentally human endeavors. It is not a surprise that many major universities in the U.S., for example, have complex legacies of exploiting slave labor in the past. However, what *should be* surprising is our continued inaction in the face of clear evidence of injustice and wrongdoings. After all, aren't we supposed to be the custodians of evidence-based action?

Chapter 1: Introduction

As late as nearly 70,000 years ago, *Homo Sapiens* was merely an unremarkable human species confined to East Africa. At the time, we shared the planet with other human species, including *Homo Neanderthalis* and *Homo Erectus* among numerous others. Over the next 60,000 years, however, the seemingly unremarkable *Sapiens* went on to grow in numbers and occupy all corners of the world while our other human cousins faded away into extinction. The spectacular success of our species is a conundrum that has captivated the interest of historians and biologists for centuries. According to present day scientific consensus, the secret to our success appears to lie in our unique ability to communicate efficiently. Historians have argued that part of what has set *Sapiens* apart from all other human and non-human species is our ability to not only imagine that which does not exist, but also then communicate this imagined reality effectively across very large numbers through language and art.

That may seem like a strange first paragraph of a Ph.D. thesis in optics, but the connections between modern day scientific research in the optical sciences and the origins of our species run deep. Evolution has shaped us to understand the world around us and adapt. Coupled with our cognitive ability to ask existential questions, including that of our own origins, humanity has, over time, increasingly invested in understanding the forces that shape the natural world. As the modern field of physical sciences developed over the past half a millennium, scientists have

grown to appreciate the critical role that the forces of the physical universe continue to play in determining the very existence of life.

In particular, advances made since the days of James Clerk Maxwell in understanding one of the four known forces of our universe – namely the electromagnetic force – have not only answered many fundamental questions relating to the physical universe (and by extension the existence of structures that support complex life in it), but have also led to a remarkable streak of technological advancements that have altered our way of life dramatically. Within a span of a few hundred years, humanity went from having no real means of communicating swiftly across the vast planet that we have come to occupy to complete integration into our personal and social lives a network of fiber optic cables that lines the ocean beds. At the time of writing of this thesis, we are living through an age of unprecedented information access enabled in large part by electromagnetic waves, and it may not be a stretch to suggest that this new *artificial* capability of communication could prove to be as consequential as our natural ability did 70,000 years ago in determining the future of our species and our societies.

1.1 Motivation

The foundational inventions that have in large part made modern telecommunication systems possible are the laser [1], the erbium-doped fiber amplifier (EDFA) [2], and low loss single mode fibers (SMFs) [3] – two out of the three have been recognized by Nobel Prizes. The broadband amplification offered by the EDFA across the SMF's low loss spectral window, coupled with the development of advanced modulation formats and digital signal processing [4, 5], has enabled communication systems with large bandwidth, long range and high data rates. Fiber op-

tic systems therefore offered the capability to transmit large volumes of information across long distances in a cost-efficient manner – something that traditional coaxial cable systems are not capable of.

Fiber-based communication systems have proven to be a disruptive force not only within the confines of the telecommunications industry, but they have unlocked the internet era and have enabled a whole host of internet-based applications, services and businesses. As the technology improved and the achievable data rates per fiber grew, so did its adoption for commercial applications. The past two decades have seen an unprecedented globalization of entire industries, which has brought major changes to local and national economies. The possibility of on-demand 24×7 access to information, news, educational and entertainment streaming has created new businesses and industries that did not exist merely 20 years ago. Concurrent advances in computing systems has led to an explosion of new applications such as social media, cloud technology and distributed computing. The fiber optic enabled internet has also proven instrumental in modernizing the banking sector, and has even enabled the creation and adoption of cryptocurrencies [6].

This is far from an exhaustive list of major transformations that the internet has enabled. This remarkable success wherein we now have entire sectors of the economy dependent upon this technology, however, has also meant that the demand for internet access has dramatically gone up. With ever-increasing consumer demand for data-consuming applications such as video streaming and gaming, the finite bandwidth of the current fiber optic systems is being swiftly consumed.

Over the past two decades, researchers have progressively increased the information transmission capacity per fiber by utilizing the different modulation dimensions of the electric field propagating in an SMF: namely wavelength, polarization, amplitude, time and quadrature (i.e.

phase) [5, 7–9]. However, the degree to which each of these modulation dimensions can be utilized to increase the data rates is limited. For example, the polarization dimension is limited by the fact that any electromagnetic wave has only two orthogonal polarization states. The number of spectral channels available via wavelength division multiplexing (WDM) is limited by the spectral bandwidth of the fiber low loss window as well as the amplification bandwidth of optical amplifiers.

In his seminal paper published in 1948, Claude Shannon showed that the information transmission capacity of a memoryless channel scales in proportion to the bandwidth and to the logarithm of the signal-to-noise ratio (SNR) [10]. For a fixed bandwidth, channel capacity can be increased by improving the SNR. Increasing the signal power transmitted through the channel is one way of improving the SNR – and therefore the channel capacity – but only up to a certain point. As the signal power increases, the nonlinear response of the fiber medium becomes increasingly important. Nonlinear distortions can in principle be corrected by way of digital signal processing, but can be computationally expensive and not always possible. As a result, the growth of fiber optic technology over the past few decades has been matched by a simultaneous growth in the research area of nonlinear fiber optics (NLFO). Numerous research papers and textbooks [11] have been written about this subject, and we will revisit key concepts from NLFO throughout this thesis.

It has been reported that we are soon approaching a capacity crunch in long-haul communication networks owing to increased demand [12, 13]. The past decade has seen several demonstrations of fiber transmission close to the Shannon limit for single-moded systems, as shown in Fig. 1.1. Multiplexing in the spatial domain is expected to provide the necessary system capacity growth required to match demand over the next few decades [12, 13]. As a result, the study of

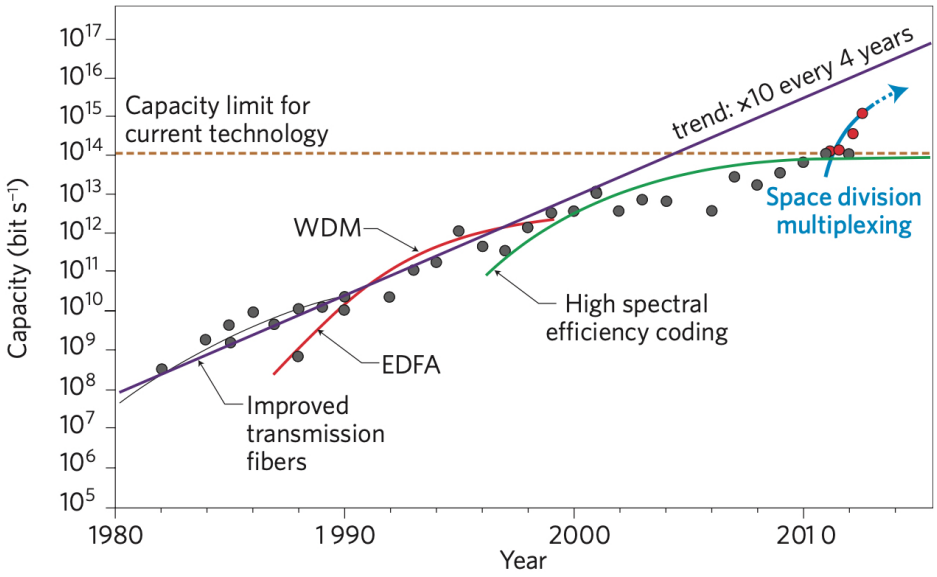

Figure 1.1: The evolution of transmission capacity in optical fibers (laboratory demonstrations). Space division multiplexing is expected to provide the next big leap in capacity per fiber. (Reprinted by permission from Nature Photonics: Richardson et al., Nat. Phot. 7, 354-362 (2013) © Nature)

optical transmission physics in multimode fibers (MMFs) has received renewed interest.

Researchers have developed a variety of different fibers for the purpose of spatial multiplexing. Broadly, they can be divided into two categories based on the number of cores: multicore fibers (MCFs) and single-core MMFs. Strictly speaking, MCFs also fall within the category of multimode fibers – i.e. fibers consisting of multiple spatial modes. However, it is helpful to make the distinction between single and multicore fibers owing to the difference in the degree to which the different spatial modes overlap. In this thesis, we will only focus on single core MMFs. We will revisit the different kinds of MMFs that are currently under study as well as their spatial mode properties in Chapter 2.

As in SMF systems, nonlinear impairments are also expected to play a significant role in

MMF-based space division multiplexed (SDM) systems. Consequently, the field of multimode nonlinear fiber optics (MMNLFO) has received considerable attention during this past decade. Because of the added spatial degree of freedom (in addition to time, amplitude, wavelength, phase and polarization), MMNLFO is considerably more complex than NLFO in SMFs, especially in fibers that support hundreds of co-propagating spatial modes. However, this added complexity has also made possible the observation of many unique phenomena occurring in MMFs that do not have a known analog in SMF-based NLFO. For example, a Kerr-induced beam cleanup phenomenon was recently reported [14, 15] wherein an initially speckled beam consisting of hundreds of spatial modes in a graded-index (GRIN) MMF "self cleans" into a Gaussian-like intensity pattern purely because of the fiber's third order Kerr nonlinearity and in the absence of any dissipative processes such as Raman scattering. Other experiments with a similar fiber uncovered a phenomenon similar to the well-known modulation instability that occurs in SMFs, namely spatiotemporal modulation instability [16]. In another recent experiment, the spatial self-imaging property of the modes of a GRIN MMF was found to lead to ultra broadband supercontinuum generation [17,18]. Similar to the case of SMFs, solitons have also been observed in multimoded fibers [19,20]. Other studies have not only demonstrated the existence of multimode solitons, but also reported the observation of supercontinuua resulting from dispersive wave generation in the presence of multimode solitons [21,22].

Many of these recently uncovered phenomena demonstrate the rich complexity in the physics of MMNLFO. All of the phenomena referenced above were observed using off-the-shelf commercially available equipment in commercially available fibers. In fact, these findings demonstrate that multiple nontrivial and counterintuitive phenomena can occur in the exact same fiber for only moderately different input excitation conditions. This diversity of possibilities

should be exciting to the scientific community well beyond that of nonlinear fiber optics – in fact well beyond that of optics itself. This may seem like a bold claim to make, but allow me to elaborate.

First, as mentioned previously, developing an understanding of nonlinear propagation of light in MMFs is of fundamental importance to future telecommunication systems. In particular, understanding and controlling the nonlinear transformation of multimodal light over long distances of fiber propagation will enable not only compensation schemes to mitigate nonlinearity-induced noise in MMF-based SDM systems, but it will also pave the way for the design and development of new multimode light sources, multimode amplifiers, repeaters and frequency converters. Notably, frequency converters and light sources based on multimodal nonlinearity is also expected to be of significant importance to quantum communication networks [23, 24].

Secondly, ultrashort pulsed and supercontinuum light sources based on MMNLFO are capable of providing high energy pulses over a broad spectral range [17, 25, 26], all in a compact device. In addition to all the typical use cases of ultrafast lasers, MMNLFO-based compact and fiber-coupled sources would be of special interest for applications such as biomedical optics [27], optical coherence tomography (OCT), frequency metrology, and prototyping and manufacturing [28, 29].

Thirdly, MMNLFO is also of interest from a fundamental physics perspective beyond the field of optics given the mathematical and analytical similarities shared by the theoretical frameworks describing multimodal nonlinearity and those that describe Bose-Einstein Condensates (BECs) and other condensation phenomena [30]. Specifically, multimodal nonlinearity can be described by the well known Gross-Pitaevskii Equation [17] – an equation that is well known to physicists studying BECs, bosonic gases and superfluids [30, 31]. From this perspective,

MMNLFO can serve as a versatile experimental playground for understanding the physics of various other systems.

In summary, the interest in MMNLFO comes from a variety of different perspectives and applications that cut across several modes of research: fundamental, applied as well as product-oriented. These reasons serve as motivation for the work that we have carried out over the past few years in this research field. With this broad motivation in mind, the following section outlines the specific goals of our work.

1.2 Research Objectives

Although the numerous phenomena referenced in the previous section do well to demonstrate the rich complexity of nonlinear optical effects occurring in MMFs, it remains true that MMNLFO is a relatively under-explored topic, especially compared to NLFO in SMFs. This thesis is the result of a humble attempt to address some of the many research gaps in the field, as well as to introduce new experimental tools and research perspectives while also shedding light (pun intended) on the physics of fundamental intermodal nonlinear interactions between individual modes. Although scientific research in the optical sciences is very often exploratory and open-ended in nature (and it has certainly been that way in this case), it is possible nonetheless to retrospectively come up with a list of broad research objectives that summarize the scope and reach of this work.

1. Most literature in the field – including many (if not all) of the phenomena described in the previous section – has thus far primarily focused on what I like to call the "macroscopic" thermodynamic picture that involves complex effects with large-scale variations in the spa-

tiotemporal field distribution. This is analogous to the classical thermodynamic study of gases. A lot of the terminology and mathematics used to analyze and explain these phenomena is, in fact, borrowed from classical thermodynamics (see [30, 32] for example). In this work, we focus on the "microscopic" picture. More specifically, we seek to advance the understanding of intermodal nonlinear interactions between a small number of spatial modes. In the gas analogy, studying the microscopic picture is equivalent to studying the interactions between individual gas molecules. Neither picture alone is sufficient in providing a complete understanding of a gas system. Understanding the physics of interactions between individual gas molecules is imperative to being able to predict macroscopic dynamics. Similarly, the macroscopic picture alone is not sufficient in developing a complete understanding of MMNLFO. Understanding the nonlinear interactions between individual modes in a rigorous and quantitative manner wherein numerical models can be validated is imperative to understanding and predicting the macroscopic picture of optical thermodynamics. This forms our first research objective.

Although this aspect of MMNLFO has not received sufficient attention, there are several new studies nonetheless that explore nonlinear interactions between individual fiber modes such as self-phase modulation (SPM), cross-phase modulation (XPM) and four-wave mixing (FWM) [33–36].

2. Our second research objective relates to the fact that most of the extraordinary phenomena observed thus far (referenced above) have been measured using conventional experimental techniques that do not resolve in space and time/frequency simultaneously. This would not be a problem in SMF systems wherein the spatial dimension does not exist (i.e. there

is only one spatial mode), leaving the time and frequency domains to be measured using well-known techniques and commonly available instruments. This would also not be a problem in cases where there are no temporal or spectral dynamics – such as in the linear propagation regime in MMFs and other multimoded waveguides. In MMNLFO, however, nonlinear dynamics occur within a single pulse duration across a 2-dimensional beam. As a result, spatiotemporal and/or spatio-spectral measurement techniques are required in order to accurately characterize these effects. In this work, we demonstrate new experimental techniques to resolve the output beam in space and time simultaneously.

3. Our final research objective relates to orbital angular momentum (OAM) [37] fiber modes. Most literature in the field studies nonlinear optical effects involving linearly polarized (LP) modes in step-index and graded-index MMFs. In recent years, however, new kinds of optical fibers have been developed that support stable propagation of fiber modes that carry a well-defined OAM [38–40]. These fibers are of great interest for a variety of applications ranging from classical and quantum communication to atomic physics. Nonlinear optical physics involving OAM modes, however, remains understudied. An important thrust of our research over the past couple of years has involved understanding the linear and nonlinear propagation properties of OAM modes in vortex fibers reported in [39]. Because of the significant differences between the scalar LP modes and the circularly polarized (i.e. vector) and complex OAM modes, we have sought to push the boundary of knowledge in MMNLFO in the context of nonlinearly interacting vector modes.

While this list is not an exhaustive one, it serves its purpose of priming the reader to the kinds of problems that we attempt to tackle in this work. We will revisit each of these broad

research objectives in the upcoming chapters.

1.3 Organization of Thesis

This thesis focuses on the study of nonlinear pulse propagation in the presence of a small number of interacting spatial modes. We explore multiple kinds of fibers as well as mode bases, and report multimodal nonlinear phenomena that have not been reported before. Throughout the process, we work out the theory, model the pulse propagation numerically, develop new and custom-designed experimental tools, perform unique measurements of multimodal nonlinearity and compare experimental observations with theory and simulations. This thesis is organized so as to allow for a comprehensive description of this work in a systematic manner.

Chapter 1 covers the motivation, background and research objectives, and also lists relevant literature.

Chapter 2 focuses on the basics of wave propagation. This includes a description of the different kinds of optical fibers that we use and their mode properties, as well as a theoretical description of nonlinear optics in MMFs. Some notes on numerical modeling tools are also included.

In Chapters 3-6, we describe a number of experiments that we have carried out throughout the course of my Ph.D. In each of these chapters, we discuss the new experimental tools that we built, and the well-known tools and techniques that we adapted for our purposes, to help shed light on the unique spatiotemporal nature of multimodal nonlinear effects.

In Chapter 3, we describe our very first experiments examining spatially-resolved power-dependent temporal interference patterns observed when multiple radially symmetric modes of a

parabolic GRIN fiber co-propagate in the nonlinear regime.

In Chapter 4, we observe a similar effect in a step-index FMF, except with these experiments being much more controlled and rigorous, allowing for quantitative comparison between simulation and experiment. We discuss a unique phase mask technique that we implemented to control the modes that were excited, and also describe the new spatiotemporal characterization tool that we developed to report the first spatiotemporal measurements of multimodal nonlinearity.

In Chapter 5, we briefly turn our attention back to parabolic GRIN fibers to discuss Kerr-induced beam self-cleaning. Although detailed study of such phenomena involving hundreds of spatial modes has not been the focus of this thesis, we nevertheless discuss measurements that we performed wherein we implement our spatiotemporal characterization tool to measure this phenomenon in a spatially and temporally resolved manner.

In Chapter 6, we discuss our work on examining nonlinear optical effects involving OAM fiber modes. We first describe our discovery and experimental observations of a spatiotemporal generalization of the well-known nonlinear polarization rotation effect.

Finally, Chapter 7 offers some concluding perspectives and a brief discussion on potentially interesting future directions for this work.

Chapter 2: Wave Propagation in Multimode Optical Fibers

2.1 Overview

In this chapter, we review the basics of nonlinear wave propagation in multimode fibers. In Section 2.2, we first present a description of the spatial mode theory beginning from Maxwell's Equations, and discuss a general method for solving for the spatial modes of a circularly symmetric fiber. Because this is a topic that is well-covered in several textbooks, we won't dwell on the details, but instead focus on providing a concise summary of the mathematical background needed to understand the research undertaken, highlighting the aspects that are unique to the multimode case.

We will then discuss random linear mode coupling, what causes linear coupling and how it can be understood and minimized. We then describe the different types of optical fibers used in this work, and describe their spatial mode properties. This will also give us an opportunity to discuss the different mode representation bases and the differences between different bases. Although the choice for the mode basis may not be too important in understanding the "macroscopic" effects, it is crucial for gaining meaningful insight into the intermodal nonlinear interactions at the individual mode level. We close the section with a note on mode solving tools.

In Section 2.3, we review some basics of nonlinear optical physics in fibers before discussing analytical modeling of nonlinear pulse propagation in MMFs. We introduce the nonlin-

ear Schrödinger equations (NLSEs) for multiple co-propagating spatial modes, and go over the different nonlinear effects that can be described by the $\chi^{(3)}$ tensor. We conclude the chapter by briefly discussing numerical tools for solving coupled NLSEs.

2.2 Spatial Modes

For the discussion presented here on general mode theory, [41, 42] are excellent resources; the former consists of a beginner-friendly description of mode theory, whereas the latter provides a more complete and rigorous version. For the discussion on OAM mode theory, we will mostly follow [42] and [43].

2.2.1 Waveguide Mode Theory

Electromagnetic (EM) waves propagating in a medium can be mathematically described using 3-dimensional vectors for the electric and magnetic fields, $\vec{\mathcal{E}}(x, y, z)$ and $\vec{\mathcal{H}}(x, y, z)$, where x, y and z represent the cartesian coordinates. In a waveguide, $\vec{\mathcal{E}}$ and $\vec{\mathcal{H}}$ can be broken down into two parts: one that represents the fraction of the EM wave guided along the waveguide, and another that represents the fraction that is radiated from of the waveguide. The guided portion can then be expressed as a weighted sum of a finite set of bound spatial modes in the waveguide. These modes can be thought of as similar to the modes of a guitar string, or the wave functions of an electron in a potential well. They represent transverse resonances of the EM fields within the waveguide boundaries. They are derived as the solutions to the source-free Maxwell's equations.

Denoting the electric and magnetic fields describing the j^{th} mode by $\mathbf{E}_j(x, y, z)$ and $\mathbf{H}_j(x, y, z)$, and taking advantage of the translational invariance (i.e. cylindrical symmetry) of an optical fiber,

$\mathbf{E}_j$ and $\mathbf{H}_j$ can be expressed as follows:

$$\mathbf{E}_j(x, y, z) = \mathbf{e}_j(x, y)e^{i\beta_j z} \tag{2.1a}$$

$$\mathbf{H}_j(x, y, z) = \mathbf{h}_j(x, y)e^{i\beta_j z} \tag{2.1b}$$

where β_j is the z eigenvalue of Maxwell's equations in the waveguide, and is known as the propagation constant of the j^{th} mode. Note that in this representation, for the sake of succinctness, we have dropped the time dependence of the fields $e^{-i\omega_0 t}$, where ω_0 is the carrier frequency of the EM wave. Note additionally that although the z dependence of the EM fields is factored out as $e^{i\beta_j z}$, the remaining parts $\mathbf{e}_j(x, y)$ and $\mathbf{h}_j(x, y)$ are still 3-dimensional vectors and have components along the z axis. Further, having identified z as the propagation axis, it is useful to separate out the transversal and longitudinal components as follows:

$$\mathbf{e}_j(x, y) = \mathbf{e}_{t,j}(x, y) + e_{z,j}(x, y)\hat{\mathbf{z}} \tag{2.2a}$$

$$\mathbf{h}_j(x, y) = \mathbf{h}_{t,j}(x, y) + h_{z,j}(x, y)\hat{\mathbf{z}} \tag{2.2b}$$

We start our analysis from the vector wave equations listed below. Chapter 30 in reference [42] consists of a full derivation of these wave equations beginning from Maxwell's equations:

$$\{\nabla_t^2 + n^2k^2 - \beta_j^2\}\mathbf{e}_j = -\{\nabla_t + i\beta_j\hat{\mathbf{z}}\}\{\mathbf{e}_{t,j}.\nabla_t \ln(n^2)\} \tag{2.3a}$$

$$\{\nabla_t^2 + n^2k^2 - \beta_j^2\}\mathbf{h}_j = -\nabla_t \ln(n^2) \times \{(\nabla_t + i\beta_j\hat{\mathbf{z}}) \times \mathbf{h}_j\} \tag{2.3b}$$

where $n = n(x, y)$ is the refractive index profile of the fiber cross section, $k = 2\pi/\lambda$ is the free-space wavenumber, λ is the free-space wavelength of light, ∇_t (with the subscript t) refers to the gradient operator along the transverse coordinates (i.e. x and y), and $\hat{\mathbf{z}}$ is the cartesian unit vector along the z direction.

By substituting Eqs. 2.2 into the source-free Maxwell's equations, the transversal and longitudinal components of the electric and magnetic fields can be expressed in terms of each other as follows [42]:

$$\mathbf{e}_t = -\left(\frac{\mu_0}{\varepsilon_0}\right)^{1/2} \frac{1}{kn^2}\hat{\mathbf{z}} \times (\beta\mathbf{h}_t + i\nabla_t h_z) \tag{2.4a}$$

$$\mathbf{h}_t = \left(\frac{\varepsilon_0}{\mu_0}\right)^{1/2} \frac{1}{k}\hat{\mathbf{z}} \times (\beta\mathbf{e}_t + i\nabla_t e_z) \tag{2.4b}$$

$$e_z = \frac{i}{\beta}(\nabla_t.\mathbf{e}_t + (\mathbf{e}_t.\nabla_t)\ln(n^2)) \tag{2.4c}$$

$$h_z = \frac{i}{\beta}\nabla_t.\mathbf{h}_t \tag{2.4d}$$

where we have momentarily dropped the index j for simplicity. The term $\nabla_t \ln(n^2)$ in Eqs. 2.3 and 2.4 incorporates polarization phenomena due to the waveguide structure. In order to see this, consider the case of an EM wave propagating in an unbounded medium of uniform refractive index everywhere ($n(x, y) = n_1$; i.e. effectively free space). Substituting $\nabla_t \ln(n^2) = 0$ into Eqs. 2.4 yields the following expressions for the longitudinal field components: $e_z = \frac{i}{\beta}\nabla_t.\mathbf{e}_t$

and $h_z = \frac{i}{\beta}\nabla_t.\mathbf{h}_t$. Both of these components are equal to 0 in a uniform medium, as the field components in a uniform medium have no dependence on x and y by definition of uniformity.

Put simply, the modal fields in a uniform medium are transverse electromagnetic (TEM) waves, and their transversal components satisfy the relation $\mathbf{h}_t = (\varepsilon_0/\mu_0)^{1/2} n_1 \hat{\mathbf{z}} \times \mathbf{e}_t$ in accordance with Eqs. 2.4. The propagation constant can further be found to be a constant $\beta = n_1 k$, independent of $\mathbf{e}_t$ (i.e. the state of polarization of the beam). In a wave-guiding structure, however, $\nabla_t \ln(n^2) \neq 0$, and the modes are no longer TEM waves. Eqs. 2.3 also suggest a dependence of the right hand side (and thereby β_j) on the transverse electric field vector $\mathbf{e}_t$, i.e. the polarization of the beam. In other words, the dependence of a mode's linear propagation properties on its polarization results from the presence of a non-uniform cross-sectional refractive index profile. This is to say that even a circularly symmetric fiber can, in principle, be birefringent. Although this might sound like a stretch at first sight, as we will see later, specialized fiber designs take advantage of this polarization dependence to create a large effective index difference between modes that have identical intensity profiles but opposite polarizations in a circularly symmetric fiber [39, 43].

Eqs. 2.3 give us a qualitative appreciation of the connection between a mode's state of polarization and its linear propagation properties, but further insight can be gained by solving Eqs. 2.3 for a given refractive index profile. However, the full vector wave equations are difficult to solve analytically for most refractive index profiles, and a perturbative approach is often adopted to analyze the modal fields of optical fibers. Such an approach comprises of setting $\nabla_t \ln(n^2) = 0$ in the right hand side of Eqs. 2.3 – i.e. solving the so called "scalar wave equation" (SWE) – and then adding a corrective term to the modal fields and propagation constants. (It is worth noting that for fibers with piecewise uniform refractive index profiles, $\nabla_t \ln(n^2) = 0$ everywhere

except at the boundaries. For such cases, the scalar wave equation simply assumes that the field and its gradient are continuous everywhere, and the vector wave method is different only in that appropriate boundary conditions are applied when solving Maxwell's equations.)

Similar to perturbative approaches from quantum mechanics that the reader might be familiar with, this approach is valid when the "perturbation" from the case for which the scalar wave equation is fully valid – namely propagation in a uniform medium – is small. Suppose that the index profile of the fiber were to be expressed as:

$$n^2(x,y) = n_{co}^2(1 - 2\Delta f(x,y)) \tag{2.5}$$

where n_{co} is the core refractive index, $\Delta = (1/2)(1 - n_{cl}^2/n_{co}^2)$ is the index height parameter, n_{cl} is the cladding refractive index and $f(x,y)$ describes the index profile function. The perturbative approach is valid in the regime of $\Delta \ll 1$, which holds true for most commercially available optical fibers. This is known as the "weakly guiding approximation" (WGA). In the WGA, the transversal mode field profiles are given by the solutions to the SWEs solved with appropriate boundary conditions. However, the first order correction addresses the longitudinal components as well as the modal propagation constants. Unlike in the uniform medium case, the longitudinal components are non-zero but small in comparison to the transversal components. They are given by Eqs. 2.4 but with the $\nabla_t \ln(n^2)$ terms absent:

$$e_{z,j} = \frac{i}{\beta} \nabla_t . \mathbf{e}_{t,j} \tag{2.6a}$$

$$h_{z,j} = \frac{i}{\beta} \nabla_t . \mathbf{h}_{t,j} \tag{2.6b}$$

Additionally, unlike in a uniform medium, the propagation constants are not independent of the modal field polarization. The 0^{th} order approximation for β_j in the WGA is given by $\tilde{\beta}_j$, which satisfies the SWEs

$$\{\nabla_t^2 + n^2k^2 - \tilde{\beta}_j^2\}\mathbf{e}_{t,j} = 0 \tag{2.7a}$$

$$\mathbf{h}_{t,j} = n\left(\frac{\varepsilon_0}{\mu_0}\right)^{1/2}\hat{\mathbf{z}} \times \mathbf{e}_{t,j} \tag{2.7b}$$

The perturbative "polarization correction" to the propagation constant is given by [42, 43]:

$$\delta\beta \approx \frac{a(2\Delta)^{3/2}}{2V}\frac{\int_{A_\infty}(\nabla_t.\mathbf{e}_t)\mathbf{e}_t.\nabla_t f(x,y)dA}{\int_{A_\infty}\mathbf{e}_t^2 dA} \tag{2.8}$$

where we have once again dropped the modal index j for simplicity of notation. $V = (2\pi a/\lambda)(n_{co}^2 - n_{cl}^2)^{1/2}$ is the waveguide parameter, a is a typical linear dimension in the fiber cross-section (typically the core radius), and $\int_{A_\infty}$ represents integration over an infinite cross-section.

We now consider the case of a circular fiber. The refractive index profile can be expressed in cylindrical coordinates r and ϕ as:

$$n^2(R) = n_{co}^2(1 - 2\Delta f(R)) \tag{2.9}$$

where $R = r/a$, and n_{co} is the maximum index (typically that of the core). As mentioned before, under the WGA, the transverse field components $\mathbf{e}_t$ and $\mathbf{h}_t$ are obtained by solv-

ing the SWE. When written in cylindrical coordinates, the terms in ∇_t^2 suggest separable solutions for the transverse components $e_x(r,\phi)$ and $e_y(r,\phi)$ of the form $\Psi = F_l(r)\cos(l\phi)$ and $\Psi = F_l(r)\sin(l\phi)$, where $l = 0, 1, ...$ is the azimuthal mode order and $F_l(r)$ satisfies the following differential equation [42]:

$$\left(\frac{d^2}{dr^2} + \frac{1}{r}\frac{d}{dr} + k^2 n^2(r) - \frac{l^2}{r^2} - \tilde{\beta}^2\right) F_l(r) = 0 \tag{2.10}$$

This can be written in dimensionless form by defining $\tilde{U} = a(k^2 n_{co}^2 - \tilde{\beta}^2)^{1/2}$:

$$\left(\frac{d^2}{dR^2} + \frac{1}{R}\frac{d}{dR} + \tilde{U}^2 - \frac{l^2}{R^2} - V^2 f(R)\right) F_l(R) = 0 \tag{2.11}$$

The polarization correction terms can then be expressed (see Tables 2.1, 2.2 and 2.3) in terms of two integrals that are defined as follows:

$$I_1 = \frac{(2\Delta)^{3/2}}{4aV} \int_0^\infty R F_l \frac{dF_l}{dR}\frac{df}{dR} dR \Big/ \int_0^\infty R F_l^2 dR \tag{2.12a}$$

$$I_2 = \frac{l(2\Delta)^{3/2}}{4aV} \int_0^\infty F_l^2 \frac{df}{dR} dR \Big/ \int_0^\infty R F_l^2 dR \tag{2.12b}$$

For a given refractive index profile specified by $f(R)$, the radial equation Eq. 2.11 can be solved to obtain the radial part of the modal solutions. For simple refractive index profiles such as the step profile, Eq. 2.11 can be solved analytically. For more complex profiles, however, numerical tools are needed to solve for the modes (see Sections 2.2.6 and 2.2.7).

Before we introduce the modes, a couple of notes on notation. First, the radial equation Eq. 2.11 can have multiple solutions depending upon the refractive index profile described by

$f(R)$ and the value of the azimuthal mode index l. The radial solutions for a given value of l are labeled by the radial index m. Each mode therefore is specified by two indices, l and m. Second, we follow the conventional hybrid mode notation used in Reference [42]. For any $l \neq 0$ and for a given m, there are 4 possible modes, arising from two orthogonal azimuthal solutions and two orthogonal polarization states. These modes are labeled as EH or HE depending upon the relative magnitudes of the E and H fields describing the mode. Modes within each EH or HE group are further classified into "$even$" or "odd" modes based on whether the azimuthal variation of the e_x is described by a $\cos$ or $\sin$. (The $even$ and odd mode classification can also be done based on the azimuthal function of e_y without loss of generality.) Furthermore, for the special case of $l = 1$, the z component of either the electric or magnetic fields of two of the modes come out to be 0. These modes are appropriately labeled "transverse electric" (TE) and "transverse magnetic" (TM). Using Eqs. 2.6, 2.7 and 2.8, we are now ready to introduce the mode fields in terms of the radial parts F_l and azimuthal parts $\cos(l\phi)$ and $\sin(l\phi)$. Table 2.1 lists the modes for the special case of $l = 0$, and Tables 2.2 and 2.3 list the modes for $l \geq 1$.

Table 2.1: $l = 0$ Modes of a Circular Fiber. (Reproduced with permission from *Optical Waveguide Theory* by Snyder, A. W. and Love, J. D. (1983) © Springer)

Mode	$\mathbf{e}_t$	$\mathbf{h}_t$	e_z	h_z	$\delta\beta$
HE_{1m}^{ev}	$\hat{\mathbf{x}}F_0$	$n_{co}\left(\frac{\varepsilon_0}{\mu_0}\right)^{1/2}\hat{\mathbf{y}}F_0$	$i\frac{(2\Delta)^{1/2}}{V}G_0\cos(\phi)$	$in_{co}\left(\frac{\varepsilon_0}{\mu_0}\right)^{1/2}\frac{(2\Delta)^{1/2}}{V}G_0\sin(\phi)$	I_1
HE_{1m}^{odd}	$\hat{\mathbf{y}}F_0$	$-n_{co}\left(\frac{\varepsilon_0}{\mu_0}\right)^{1/2}\hat{\mathbf{x}}F_0$	$i\frac{(2\Delta)^{1/2}}{V}G_0\sin(\phi)$	$-in_{co}\left(\frac{\varepsilon_0}{\mu_0}\right)^{1/2}\frac{(2\Delta)^{1/2}}{V}G_0\cos(\phi)$	I_1

Table 2.2: Transverse Components of $l \geq 1$ Modes of a Circular Fiber. (Reproduced with permission from *Optical Waveguide Theory* by Snyder, A. W. and Love, J. D. (1983) © Springer)

Mode	$\mathbf{e}_t$	$\mathbf{h}_t$
$HE^{ev}_{l+1,m}$	$(\hat{\mathbf{x}}\cos(l\phi) - \hat{\mathbf{y}}\sin(l\phi))F_l$	$n_{co}\left(\frac{\varepsilon_0}{\mu_0}\right)^{1/2}(\hat{\mathbf{x}}\sin(l\phi) + \hat{\mathbf{y}}\cos(l\phi))F_l$
$HE^{odd}_{l+1,m}$	$(\hat{\mathbf{x}}\sin(l\phi) + \hat{\mathbf{y}}\cos(l\phi))F_l$	$-n_{co}\left(\frac{\varepsilon_0}{\mu_0}\right)^{1/2}(\hat{\mathbf{x}}\cos(l\phi) - \hat{\mathbf{y}}sin(l\phi))F_l$
$TM_{0,m}$ $(l = 1)$	$(\hat{\mathbf{x}}\cos(\phi) + \hat{\mathbf{y}}\sin(\phi))F_1$	$-n_{co}\left(\frac{\varepsilon_0}{\mu_0}\right)^{1/2}(\hat{\mathbf{x}}sin(\phi) - \hat{\mathbf{y}}\cos(\phi))F_1$
$TE_{0,m}$ $(l = 1)$	$(\hat{\mathbf{x}}\sin(\phi) - \hat{\mathbf{y}}\cos(\phi))F_1$	$n_{co}\left(\frac{\varepsilon_0}{\mu_0}\right)^{1/2}(\hat{\mathbf{x}}\cos(\phi) + \hat{\mathbf{y}}\sin(\phi))F_1$
$EH^{ev}_{l-1,m}$ $(l > 1)$	$(\hat{\mathbf{x}}\cos(l\phi) + \hat{\mathbf{y}}\sin(l\phi))F_l$	$-n_{co}\left(\frac{\varepsilon_0}{\mu_0}\right)^{1/2}(\hat{\mathbf{x}}\sin(l\phi) - \hat{\mathbf{y}}\cos(l\phi))F_l$
$EH^{odd}_{l-1,m}$ $(l > 1)$	$(\hat{\mathbf{x}}\sin(l\phi) - \hat{\mathbf{y}}\cos(l\phi))F_l$	$n_{co}\left(\frac{\varepsilon_0}{\mu_0}\right)^{1/2}(\hat{\mathbf{x}}\cos(l\phi) + \hat{\mathbf{y}}\sin(l\phi))F_l$

Table 2.3: Longitudinal Components of $l \geq 1$ Modes of a Circular Fiber. (Reproduced with permission from *Optical Waveguide Theory* by Snyder, A. W. and Love, J. D. (1983) © Springer)

Mode	e_z	h_z	$\delta\beta$
$HE^{ev}_{l+1,m}$	$i\frac{(2\Delta)^{1/2}}{V}G_l^- \cos((l+1)\phi)$	$in_{co}\left(\frac{\varepsilon_0}{\mu_0}\right)^{1/2}\frac{(2\Delta)^{1/2}}{V}G_l^- \sin((l+1)\phi)$	$I_1 - I_2$
$HE^{odd}_{l+1,m}$	$i\frac{(2\Delta)^{1/2}}{V}G_l^- \sin((l+1)\phi)$	$-in_{co}\left(\frac{\varepsilon_0}{\mu_0}\right)^{1/2}\frac{(2\Delta)^{1/2}}{V}G_l^- \cos((l+1)\phi)$	$I_1 - I_2$
$TM_{0,m}$ $(l=1)$	$i\frac{(2\Delta)^{1/2}}{V}G_1^+$	0	$2(I_1 + I_2)$
$TE_{0,m}$ $(l=1)$	0	$in_{co}\left(\frac{\varepsilon_0}{\mu_0}\right)^{1/2}\frac{(2\Delta)^{1/2}}{V}G_1^+$	0
$EH^{ev}_{l-1,m}$ $(l>1)$	$i\frac{(2\Delta)^{1/2}}{V}G_l^+ \cos((l-1)\phi)$	$-in_{co}\left(\frac{\varepsilon_0}{\mu_0}\right)^{1/2}\frac{(2\Delta)^{1/2}}{V}G_l^+ \sin((l-1)\phi)$	$I_1 + I_2$
$EH^{odd}_{l-1,m}$ $(l>1)$	$i\frac{(2\Delta)^{1/2}}{V}G_l^+ \sin((l-1)\phi)$	$in_{co}\left(\frac{\varepsilon_0}{\mu_0}\right)^{1/2}\frac{(2\Delta)^{1/2}}{V}G_l^+ \cos((l-1)\phi)$	$I_1 + I_2$

where I_1 and I_2 are defined in Eqs. 2.12, and $G_l^{\pm}$ is defined as $G_l^{\pm} = \frac{dF_l}{dR} \pm \frac{l}{R}F_l$.

As an interesting aside, the TE, TM, EH and HE modes can be visualized in the ray picture in the form of meridional and skew rays. Chapter 11 in Reference [42] provides a discussion on this.

2.2.2 Linear Mode Coupling & Mode Basis States

Before we begin a discussion on the types of multimode fibers used in this work and their spatial modes, it is worth taking a pit stop to discuss the role of the polarization correction terms to the modal propagation constants Eqs. 2.8. Recall from Section 2.2.1 that there are 4 possible modes for a given value of l and m as listed in Tables 2.1, 2.2 and 2.3. For the case of $l > 1$, as Table 2.3 shows, the two HE modes are degenerate with each other, and similar is true for the two EH modes. This degeneracy arises from having equal values of $\delta\beta$. However, the two mode pairs are not degenerate with each other. In other words, for a given value of $l > 1$ and m, there are 4 modes that can be divided into two mode pairs where the modes of a particular pair are degenerate with each other. The propagation constant difference between the two mode pairs is given by $\delta\beta_{EH} - \delta\beta_{HE} = 2I_2$.

In an ideal fiber with no imperfections, two spatial modes would not mix with each other even if they were degenerate with each other, owing to the orthogonality of the modes. That is to say that if light were coupled into one spatial mode of an ideal fiber, then it would stay in that spatial mode for infinitely long propagation lengths. Optical fibers in the real world, however, consist of deformations and perturbations that cause coupling between the different spatial modes [44–46].

Intuitively, the mixing of modes in a real world can be understood as follows. The spatial modes discussed here are mathematical constructs to describe the resonant modes of an ideal fiber. However, these constructs are only approximate not only because we have made numerous simplifying assumptions (for example the WGA), but also because we have not incorporated any transversal or longitudinal random perturbations into our model. Of course, incorporating these

perturbations accurately into a numerical model is impractical if not impossible, because these perturbations might be drastically different from one fiber to another, and also depend sensitively on the physical geometry in which the optical fiber is laid out. Put differently, the mathematical constructs of spatial modes are almost always developed for ideal fibers that operate with no external perturbations. These constructs, therefore, do not fully accurately describe the true EM field resonances of a real-world fiber. As a result, the presence of real-world perturbations shows up as "coupling" between our imperfect mathematical constructs.

Mode coupling was first studied in the early 1970s when MMFs were used for optical communication [44–46]. In recent decades, interest in SDM in MMFs has revived an interest in the topic. Mode coupling has been studied using two models: the field coupling model and the power coupling model [47]. The field coupling model accounts for the complex-valued modal fields, while the power coupling model only accounts for real-valued modal powers. A deeper discussion on theoretical approaches to modeling mode coupling is beyond the scope of this thesis, especially as many questions remain unanswered in the field, and at this point we do best to cite other works (see References [43, 47, 48]) that carry a more complete review of available literature. However, we discuss here a particular aspect of modal coupling that is important for our work.

It has been shown phenomenologically that the amount of mode coupling depends upon the effective index separation of any two modes as $\propto \Delta n_{eff}^{-p}$ where $p > 4$ [46]. Other works have modeled the efficiency of mode coupling as $\propto e^{\Delta\beta z}$ [49, 50]. Whichever model may be more accurate, it has been shown conclusively that a small effective index separation leads to higher coupling among modes [45].

In order to see why this is the case, it is worth recalling that a conventional cylindrically

symmetric single-mode fiber supports two degenerate polarization modes. Although the two polarization modes would not couple in an ideal fiber with no perturbations, they do couple in real fibers, leading to an uncontrolled evolution of the polarization state of light in SMFs. Polarization maintaining fibers (PMFs) address this issue by introducing a strong birefringence corresponding to an index difference between the polarization states of $\approx 10^{-4}$ (in conventional SMFs, this difference is $\approx 10^{-}7$ [7]). The large difference in propagation constants (i.e. effective indices) because of strong birefringence means that the relative phase between the two polarization states rapidly increases as light propagates through the fiber. More accurately, so long as the beat length corresponding to the birefringence is much shorter compared to the typical spatial disorder length scale, the coupling remains minimal.

2.2.2.1 LP Mode Basis

As we noted above, for a given $l > 1$ and m, the modes of a circularly symmetric fiber can be divided into two mode pairs whose difference in propagation constants is given by $2I_2$. For most commercially available fibers, this leads to an effective index difference between the two mode pairs that is of the order of 10^{-5}, which turns out to be sufficient to couple the two mode pairs [51]. The modes resulting from this coupling can be seen by neglecting the polarization correction term Eq. 2.8 altogether. When this is done, there is no constraint on the field directions, and the modes can now be expressed in linear polarized form as, for example, $F_l(r)\cos(l\phi)\hat{\mathbf{x}}$ instead of the forms shown in Table 2.2. These form the so called linearly polarized "LP" fiber modes.

Fig. 2.1 (from Reference [51]) illustrates this phenomenon. The LP modes can be ex-

pressed in terms of the HE and EH mode basis, up to a normalization constant, as follows:

$$LP_{lm,a}\hat{\mathbf{x}} = HE^{ev}_{l+1,m} + EH^{ev}_{l-1,m} \tag{2.13a}$$

$$LP_{lm,b}\hat{\mathbf{x}} = HE^{odd}_{l+1,m} + EH^{odd}_{l-1,m} \tag{2.13b}$$

$$LP_{lm,a}\hat{\mathbf{y}} = HE^{odd}_{l+1,m} - EH^{odd}_{l-1,m} \tag{2.13c}$$

$$LP_{lm,b}\hat{\mathbf{y}} = EH^{ev}_{l-1,m} - HE^{ev}_{l+1,m} \tag{2.13d}$$

Note that for $l = 0$, the LP and the HE-EH mode bases are equivalent, and the LP_{0m} modes are indeed true modes of the fiber. For $l > 0$, however, LP_{lm} modes are *not* true modes of the fiber. This is because the constituent $HE_{l+1,m}$ and $EH_{l-1,m}$ modes are not truly degenerate. In other words, although the LP modes (resulting from transformations of Eqs. 2.13) can be used as a *representational* mode basis, they do not constitute a set of true propagation modes. In fact, the $LP_{21,a}$ "mode", for example, has a z-varying field and intensity pattern because of the beat length between the HE and EH modes. This behavior is highly unlike a true propagation mode of a fiber. One must therefore be careful in assessing whether or not LP modes form a good mode basis to describe multimodal propagation in a fiber.

2.2.2.2 OAM Mode Basis

As we discussed above, for conventional fibers such as step-index and parabolic index fibers, the LP modes basis arises from the near degeneracy of all 4 modes for a given l and m. However, it has been shown in recent years that the refractive index profile of the fiber $n(r)$ can

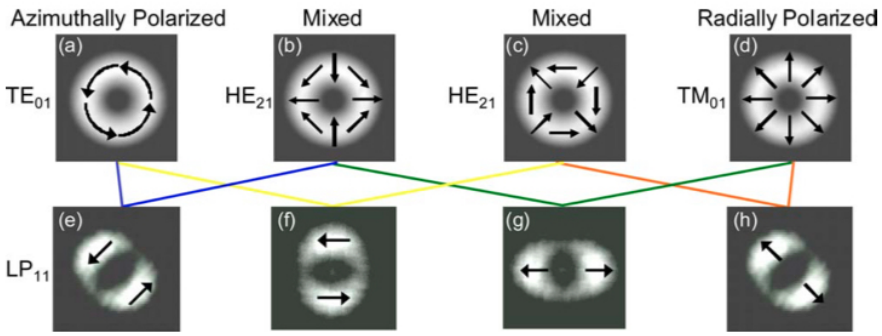

Figure 2.1: Intensity profiles of first order mode group in a fiber. Arrows describe the local state of polarization. (Top row) Vector modes that are the exact solutions for a fiber. (Bottom row) Unstable LP modes commonly obtained at a fiber output. Specific linear combinations of pairs of top row modes yield specific LP modes. (Reprinted by permission from Optica Publishing Group: Ramachandran et al., Opt. Lett. 34, 2525-2527 (2009) © Optica Publishing Group))

be tailored to *break* this near degeneracy. In other words, the two HE and EH mode pairs in conventional step and parabolic index fibers have effective indices separated by only $\approx 10^{-5}$. With a specially designed $n(r)$, however, this separation has increased by nearly a hundred fold to $\approx 10^{-3}$ [38, 39, 51]. These fibers are referred to in literature by various names: vortex fibers, ring core fibers (RCFs) and OAM fibers. The name "ring core" refers to the ring shaped refractive index profile that these fibers consist of, and the name 'OAM' arises from the fact that the most natural basis set of propagation modes in these fibers consist of a well-defined orbital angular momentum per photon. We will revisit these fibers and their spatial modes in more detail in upcoming sections, but for now, we introduce the OAM mode basis.

Although light propagating in a given fiber can be expressed using any basis set, the most natural choice is often one that best describes the unique properties of the fiber and its modes. For RCFs, this is the OAM basis. The OAM basis is defined by the following transformations (up to a normalization constant):

$$\mathbf{V}_{l,+} = HE^{ev}_{l+1} + iHE^{odd}_{l+1} \tag{2.14a}$$

$$\mathbf{V}_{-l,-} = HE^{ev}_{l+1} - iHE^{odd}_{l+1} \tag{2.14b}$$

$$\mathbf{V}_{l,-} = EH^{ev}_{l-1} + iEH^{odd}_{l-1} \tag{2.14c}$$

$$\mathbf{V}_{-l,+} = EH^{ev}_{l-1} - iEH^{odd}_{l-1} \tag{2.14d}$$

where $l > 0$. We have momentarily dropped the radial index m for simplicity, but specify that all modes involved are of the same radial index m. The subscripts $\pm l$ now refers to the topological charge, which signifies the OAM content of the mode as we will explain below. The subscripts $+$ and $-$ signify right and left circular polarization (LCP and RCP) states of the modes.

The key difference between the hybrid HE/EH mode basis and the OAM mode basis is the phase relationship between the transverse and longitudinal mode components. In the hybrid mode basis, the transverse components can be constrained to be purely real-valued, in which case the longitudinal fields are purely imaginary (or vice versa). As a consequence, in cases where one can ignore the longitudinal fields, the hybrid modes are locally linearly polarized (albeit with spatially varying orientation of the linear polarization, unlike the LP modes that are uniformly linearly polarized). In the OAM mode basis, however, the transverse fields are locally circularly polarized, leading to a different phase relationship between the transverse and longitudinal fields compared to the hybrid mode case.

In order to see that the modes in Eqs. 2.14 have a well-defined OAM, it is instructive to first note that the transversal and longitudinal components of these modes all contain an azimuthal

variation $e^{\pm l\phi}$. This can be seen using Eqs. 2.6 together with Eqs. 2.14. Additionally, one can calculate the time-averaged OAM flux for each mode given by the spatial integral:

$$\langle \Phi_{\mathscr{M}} \rangle = \int \int \left\langle \vec{\mathscr{M}}.d\vec{A} \right\rangle \tag{2.15}$$

where the angular momentum density $\mathscr{M}$ is given by:

$$\vec{\mathscr{M}} = \frac{1}{c^2}\vec{r} \times (\mathbf{E} \times \mathbf{H}) = \frac{1}{c^2}\vec{r} \times \vec{\mathscr{S}} \tag{2.16}$$

where $\vec{\mathscr{S}}$ denotes the Poynting vector. We will not show the derivation here, but it has been shown that $< \Phi_{\mathscr{M}} >$ for a mode in the OAM basis is proportional to $(\pm l \pm 1)$ [43], where the ± 1 refers to the two possible states of circular polarization, i.e. "spin angular momentum" (SAM). Each photon in such a mode has an orbital angular momentum of $\pm l\hbar$ [37]. Note that this is a unique property of the OAM mode basis, and the HE-EH modes do not have a well-defined orbital angular momentum.

The first two modes specified in Eqs. 2.14 are the so called "spin-orbit aligned" (SO_a) modes, while the last two form the "spin-orbit anti-aligned" (SO_{aa}) modes. The terms 'aligned' and 'anti-aligned' refer to the relative alignment or anti-alignment of OAM and SAM. Because the two HE (or EH) modes are degenerate with one another, the two SO_a (or SO_{aa}) modes are degenerate with each other as well.

2.2.3 Types of Multimode Fibers

Here, we briefly introduce the different kinds of MMFs that are available commercially and/or are of interest at a research level. Fig. 2.2 shows illustrations of cross-sectional structure

and corresponding refractive index profiles of some commonly used optical fibers, all of which are capable of guiding multiple spatial modes simultaneously. These fibers, and others that we haven't listed here, all have unique linear and nonlinear mode propagation properties. The differences in their modal properties arise from a number of factors, including cross-sectional structure and size, refractive index profile, number of cores, and in some cases the light guiding mechanism itself.

Although the study of linear and nonlinear propagation in these fibers makes for a very interesting research area, in this work we only focus on single core circularly symmetric fibers such as the step and graded-index FMF/MMFs and hollow RCFs. These fibers were chosen owing to their relevance to a broad range of topics including long-range telecommunication, spatial division multiplexing, high power fiber laser development and quantum optical science.

We now focus our attention on each of the three fibers studied in this work, depicted in Fig. 2.2(a)-(c). We discuss the mode properties in these fibers and show numerically generated mode images.

2.2.4 Step-Index FMF

A step-index multimode fiber consists of a cross-sectional refractive index profile that has a step-like function, as shown in Fig. 2.2(a). Because the step profile consists of two regions of constant refractive index each (namely core and cladding), Eq. 2.11 can be solved analytically to analyze the modes. We begin by noting that the refractive index profile of a step-index fiber is expressed as:

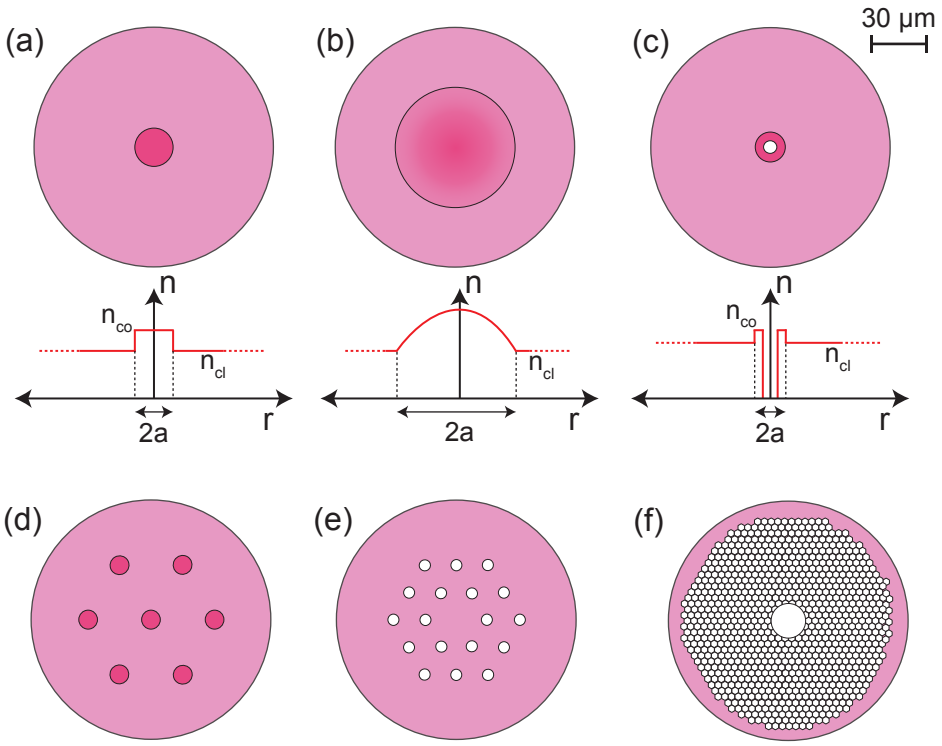

Figure 2.2: Different kinds of MMFs/FMFs and their refractive index profiles, of which (a)-(c) were used in this work. (a) Step-index FMF, (b) parabolic index MMF, (c) hollow ring-core fiber, (d) multicore fiber, (e) photonic crystal fiber, (f) hollow core fiber

$$n^2(R) = \begin{cases} n_{co}^2, & \text{for } 0 < R < 1 \\ n_{cl}^2, & \text{for } R > 1 \end{cases} \tag{2.17}$$

where, as before, $R = r/a$. Eq. 2.11 can then be rewritten as:

$$R^2\frac{d^2F_l}{dR^2} + R\frac{dF_l}{dR} + (\tilde{U}^2R^2 - l^2)F_l = 0, \quad \text{for } \ 0 < R < 1 \tag{2.18a}$$

$$R^2\frac{d^2F_l}{dR^2} + R\frac{dF_l}{dR} - (\tilde{W}^2R^2 + l^2)F_l = 0, \quad \text{for } \ R > 1 \tag{2.18b}$$

where $\tilde{U}^2 = a^2(k_0^2 n_{co}^2 - \tilde{\beta}^2)$, $\tilde{W}^2 = a^2(\tilde{\beta}^2 - k_0^2 n_{cl}^2)$ and $\tilde{U}^2 + \tilde{W}^2 = V^2$. Guided modes in the fiber correspond to $\tilde{\beta}$ such that $n_{cl}k_0 < \tilde{\beta} \leq n_{co}k_0$. This follows from the bounds on the refractive index of the fiber itself $n_{cl} \leq n(r) \leq n_{co}$, and from the fact that for a non-absorbing waveguide, the maximum phase velocity cannot exceed the maximum speed of light in the waveguide structure without losing power to radiative losses [41, 42].

The solutions to Eq. 2.18(a), for $0 < R < 1$, can be identified to be the Bessel functions of the first and second kind $J_l(S)$ and $Y_l(S)$, where $S = \tilde{U}R$. The $Y_l(S)$ solution can be rejected by noting that $|Y_l(S)| \to \infty$ as $S \to 0$ (i.e. when $R \to 0$). Similarly, the solutions to Eq. 2.18(b), for $R > 1$, can be identified to be the modified Bessel functions $K_l(S')$ and $I_l(S')$ where $S' = \tilde{W}R$. However, $I_l(S')$ can be rejected as well, since $I_l(S') \to \infty$ as S' (i.e. R) $\to \infty$. That leaves us with the following solutions for $\Psi(r, \phi)$:

$$\Psi(r,\phi) = \begin{cases} \frac{A_{norm}}{J_l(\tilde{U})} J_l(\tilde{U}r/a)\cos(l\phi) \quad \text{or} \quad \frac{A}{J_l(\tilde{U})} J_l(\tilde{U}r/a)\sin(l\phi), & \text{for } 0 < r < a \\ \frac{A_{norm}}{K_l(\tilde{W})} K_l(\tilde{W}r/a)\cos(l\phi) \quad \text{or} \quad \frac{A}{J_l(\tilde{W})} K_l(\tilde{W}r/a)\sin(l\phi), & \text{for } r > a \end{cases} \tag{2.19}$$

where we have assumed continuity at $r = a$, and A_{norm} is a normalization constant. Imposing the condition of continuity at $d\Psi/dr$ at $r = a$ leads to

$$\tilde{U}\frac{J_l'(\tilde{U})}{J_l(\tilde{U})} = \tilde{W}\frac{K_l'(\tilde{W})}{K_l(\tilde{W})} \tag{2.20}$$

where J_l' and K_l' represent first derivatives of J_l and K_l with respect to r. Although we will not show the full derivation here (see Reference [41]), the equation above can be rewritten in terms of the normalized propagation constant $b = \tilde{W}^2/V^2$ to yield:

$$V(1-b)^{1/2}\frac{J_{l-1}[V(1-b)^{1/2}]}{J_l[V(1-b)^{1/2}]} = -Vb^{1/2}\frac{K_{l-1}[Vb^{1/2}]}{K_l[Vb^{1/2}]} \tag{2.21}$$

where $l \geq 1$. For $l = 0$:

$$V(1-b)^{1/2}\frac{J_1[V(1-b)^{1/2}]}{J_0[V(1-b)^{1/2}]} = Vb^{1/2}\frac{K_1[Vb^{1/2}]}{K_0[Vb^{1/2}]} \tag{2.22}$$

Eqs. 2.21 and 2.22 are transcendental in b, and the solutions to them give universal curves for the dependence of b on V. For a given value of $l \geq 0$, the number of modes supported by the fiber is given by the number of solutions to Eq. 2.21 or 2.22. The total number of modes supported in the fiber is obtained by simply counting the number of modes supported for increasing values of $l \geq 0$. For step index fibers with a large a, an approximate number of available spatial modes (including polarization degeneracy) is given by [52]:

$$N \approx \frac{V^2}{2} \tag{2.23}$$

Note that Eqs. 2.19 only provide an equation for $\Psi(r, \phi)$, which in our notation simply refers to a cartesian component of the transverse part of the mode, i.e. e_x or e_y. It does not specify the phase relation with which these components superpose to give rise to the modal electric field. However, as we mentioned in Section 2.2.2, the effective index separation between the different HE and EH mode pairs is low enough for the modes to mix in practical fibers, resulting in the LP modes. We therefore adopt the LP_{lm} basis for step-index MMFs for the purposes of this work.

For the specific work that we describe in subsequent chapters, we adopt a step-index few

mode fiber with a core diameter of $2a = 20\ \mu m$. This fiber is often called a "few" mode fiber as opposed to a "multi" mode fiber because the number of spatial modes allowed in this fiber at typical laser wavelengths is in the 10s as opposed to 100s.

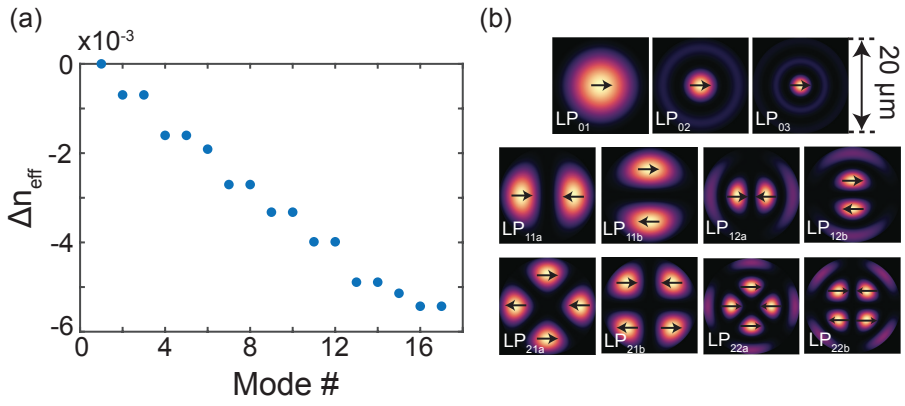

Figure 2.3: Linearly polarized spatial modes of a $2a = 20\ \mu m$ step-index FMF. (a) Distribution of modal effective indices relative to fundamental mode ($\hat{\mathbf{x}}$-polarized modes only), (b) Numerically generated intensity profiles of some $\hat{\mathbf{x}}$-polarized LP modes. Arrows represent the local state of polarization.

Fig. 2.3(b) shows the intensity profiles of the $\hat{\mathbf{x}}$-polarized LP_{lm} modes of the step-index FMF used in this work. The arrows all point along the x coordinate, and the opposite facing directions denotes opposite phase of the electric field. Fig. 2.3(a) shows a plot of modal effective indices. Notice that the only modes with the same propagation constant are those with the same l and m. This is unlike what happens in parabolic index fibers, as we will soon see. This is an important property of step-index fibers that has implications for nonlinear phenomena by way of phase matching and group velocity mismatch.

2.2.5 Parabolic Index MMF

A graded index (GRIN) fiber has a core refractive index profile that varies with the radial coordinate r as follows:

$$n^2(R) = \begin{cases} n_{co}^2\Big(1 - 2\Delta R^q\Big), & \text{for } 0 < R < 1 \\ n_{cl}^2, & \text{for } R > 1 \end{cases} \tag{2.24}$$

where q is usually designed to be equal to 1.98 to minimize intermodal dispersion. However, for the purposes of theoretical analysis, it is useful to set $q = 2$, thereby giving us the parabolic index MMF. It is helpful to make yet another simplifying assumption to solve for the modes easily, namely *extending* the parabola to infinity and simply working with:

$$n^2(r) = n_{co}^2(1 - 2\Delta R^2) \tag{2.25}$$

where R is allowed to be > 1 [41].

Similar to the case of step-index fibers, the modes of a parabolic index fiber are obtained by inserting the refractive index profile Eq. 2.25 into Eq. 2.11. We will not show the derivation here, but only list the final solution. (References [41,42] carry a full discussion, for the interested reader.) The radial solution to Eq. 2.11 for the parabolic index profile is given by:

$$F_l(r) = r^l e^{-\zeta^2 r^2/2} L_{m-1}^l(\zeta^2 r^2) \tag{2.26}$$

where $L_n^k(\kappa)$ are the associated Laguerre polynomials, and are given by:

$$L_n^k(\kappa) = \sum_{p=0}^{n} \frac{\Gamma(n+k+1)}{(n-p)!\Gamma(p+k+1)p!}\kappa^p \tag{2.27}$$

ζ is given by:

$$\zeta = \left(\frac{n_1 k_0 \sqrt{2\Delta}}{a}\right)^{1/2} = \frac{\sqrt{V}}{a} \tag{2.28}$$

with $k_0 = 2\pi/\lambda_0$ representing the free space wavenumber at the laser wavelength λ_0.

Similar to the case with step-index fibers, the HE and EH modes for commercially available GRIN fibers are found to be nearly degenerate as well, facilitating strong mixing between the 4 HE and EH modes for a given l and m. We therefore adopt the LP mode basis once again.

The modal propagation constants evaluate to:

$$\tilde{\beta}_{lm} = k_0 n_{co}\left(1 - \frac{2(2m+l-1)}{k_0 n_{co}}\sqrt{\frac{2\Delta}{a}}\right)^{1/2} \tag{2.29}$$

By defining $M = 4m + 2l - 2$ as the *principal mode number*, we see that the modes with the same principal mode number have the same propagation constant. The modes of a parabolic index fiber can be binned into mode groups, with modes in each group consisting of the same propagation constant and group velocity. Furthermore, another interesting feature of the parabolic index profile is seen by approximating $\tilde{\beta}_{lm}$ as follows:

$$\tilde{\beta}_M \approx k_0 n_{co}\left(1 - \frac{M}{2k_0 n_{co}}\sqrt{\frac{2\Delta}{a}}\right) \tag{2.30}$$

Fig. 2.4(b) shows the intensity profiles of a select few $\hat{\mathbf{x}}$-polarized LP modes of a $2a = 62.5$ μm GRIN fiber. Fig. 2.4(a) shows the distribution of modal effective indices (which relate to the

propagation constants as $n_{eff} = \tilde{\beta}/k_0$) as a function of the mode number. Together with Eq. 2.30, the plot shows not only that modes of different l and m can have the same propagation constant, but that the difference in propagation constants between the different mode groups is constant.

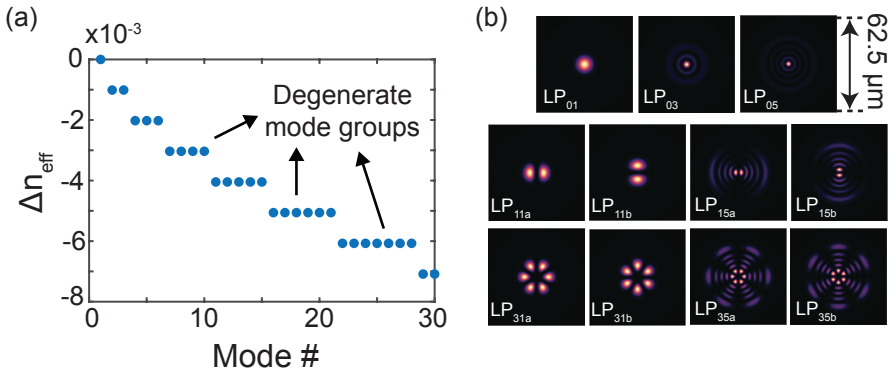

Figure 2.4: Linearly polarized spatial modes of a $2a = 62.5\ \mu m$ parabolic GRIN MMF. (a) Distribution of modal effective indices relative to fundamental mode ($\hat{\mathbf{x}}$-polarized modes only), (b) Numerically generated intensity profiles of some $\hat{\mathbf{x}}$-polarized LP modes.

This is a remarkable feature that has profound consequences for nonlinear phenomena in parabolic index MMFs. For example, the distribution of propagation constants helps phase match many four wave mixing (FWM) processes that would not be phase matched in step-index fibers. This is an important reason why complex nonlinear phenomena such as the Kerr-induced beam self-cleaning [14, 15] is only observed in parabolic GRIN fibers and not in step-index fibers. Similarly, the equal spacing of modal propagation constants gives rise to a well-known periodic self imaging effect as depicted in Fig. 2.5, where the multimodal beam exhibits a periodicity in its transverse profile as a function of z. The period is given by $z_{si} = 4\pi k_0 n_{co}\sqrt{a/2\Delta}$. This has been shown to cause a nonlinear instability phenomenon known as geometric parametric instability

(GPI) [17].

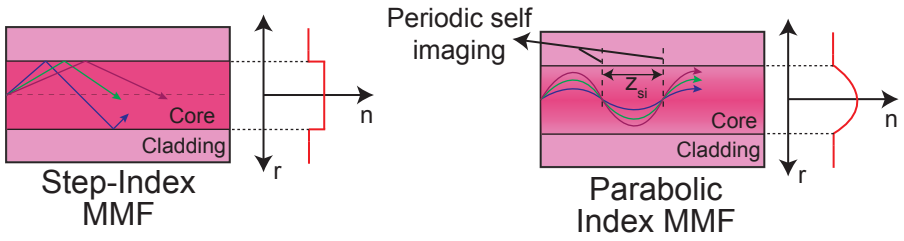

Figure 2.5: Illustration depicting periodic self imaging occurring in a parabolic index GRIN fiber. By contrast, this phenomenon does not occur in step-index fibers with an irregular distribution of modal propagation constants. z_{si} represents the self imaging period.

2.2.6 Hollow Ring Core Fiber

The final type of fiber that we study here is the so called hollow ring core fiber. As shown in Fig. 2.6(a), these fibers have a unique refractive index profile. This is a specialty fiber that is not available commercially, and the fiber used in this study was designed and provided by Prof. Siddharth Ramachandran's group at Boston University, and fabricated by OFS-Fitel LLC (see References [26, 39]).

The sharp drop in refractive index of the fiber core medium from ≈ 1.5 to 1 (i.e. air) creates the necessary index gradient to produce an index separation between the HE and EH mode pairs that is much larger than what would be obtained in a conventional solid-core fiber. The index profile of this fiber produces a strong dependence of the modal propagation constant on the *complex* vectorial spatial mode according to Eqs. 2.3 and 2.8. We emphasize the term *complex* because of the complex nature of the OAM modes described in Eqs. 2.14. For an OAM mode of a given topological charge $\pm l$, Eqs. 2.3 and 2.8 yield different propagation constants depending

upon the mode's state of polarization, which is described by the complex phase relation between the cartesian components. Equivalently, for a mode of a given state of circular polarization (LCP or RCP), the propagation constant depends upon the sign of the topological charge. This is known as the "spin-orbit coupling" effect [39, 40]. This leads to the aforementioned grouping of the 4 modes of a given l and m into spin-orbit "aligned" and "anti-aligned".

Fig. 2.6(b) shows the intensity, polarization and phase profiles for a set of 4 OAM modes with $l = 2$ and $m = 1$. We have adopted a modified notation $SO^{\pm l}_{a(a)}$ to describe a spin-orbit (anti-)aligned mode with a topological charge $\pm l$ ($l > 0$), and we have dropped the radial index m for simplicity. These modes images were generated using a numerical vector finite difference mode solver described in [53].

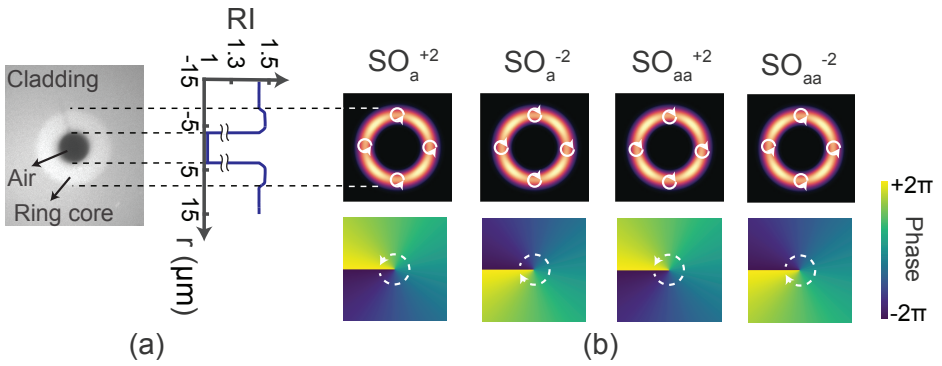

Figure 2.6: Orbital Angular Momentum modes of a hollow ring-core fiber. (a) Optical micrograph of the fiber cross section, and the cross-sectional refractive index profile of the fiber, (b) Numerically generated intensity and phase profiles of $l = 2$, $m = 1$ OAM modes. The top row images show intensity profiles, where the overlaid circular arrows depict the helicity of polarization. The bottom row images show the spatial distribution of phase, which provides the OAM.

2.2.7 A Note on Mode-Solving Tools

The spatial modes of simple refractive index profiles, like the step-index and parabolic index fibers, can be solved for analytically using the WGA. Analytical solutions exist for other index profiles that can be analyzed under the WGA as well. Reference [42] carries a discussion on modal analysis for circularly asymmetric fiber cross-sections such as homogeneous function profiles and separable profiles, and also provides methods for incorporating material anisotropy.

For refractive index profiles where the WGA may not hold, however, numerical mode-solving tools are extremely useful in generating and visualizing the spatial modes. For the hollow RCF used in this work, we used the publicly available vector finite-difference mode-solver described in Reference [53]. However, vector finite-difference solvers are typically developed for integrated photonics waveguides and therefore work using the cartesian coordinate system. While this makes them universally applicable for integrated waveguides as well as fibers, care must be taken to use such mode-solvers in the fiber context, specifically in imposing the correct mode symmetry boundary conditions depending upon the fiber's refractive index profile.

Commercial numerical mode solving tools are also available. Lumerical's MODE Solutions®is a useful finite-difference eigen-mode solver for calculating the modes of an arbitrary fiber index profile, including high index contrast profiles such as the hollow RCF, and is typically integrable with their finite-difference time domain propagation simulation tools.

Reference [54] discusses a full vectorial mode solver based on a discrete Hankel Transform, and also contains a brief review of other tools available, including recently developed ones, for the interested reader.

2.3 Multimodal Pulse Propagation Physics

Having established the concepts of spatial modes, in this section, we delve into linear and nonlinear propagation of optical pulses in multimode fibers. While most fundamental concepts introduced here will be familiar to those that are familiar with single mode fiber nonlinear optics, as we will see in Chapter 4, the added spatial dimension brings about unique phenomena that do not have an analog in SMFs.

We first review pulse propagation in the linear regime, and discuss material and waveguide dispersion, differential group delay and group velocity dispersion. We then introduce the fundamentals of nonlinear optical physics in the context of optical fibers, and present the nonlinear Schrödinger equations. We conclude the chapter with a discussion on self-phase modulation (SPM), cross-phase modulation (XPM), four-wave mixing (FWM) and phase matching considerations for FWM.

2.3.1 Linear Propagation Effects

2.3.1.1 Material Dispersion

Light propagating through a dielectric medium interacts with the bound electrons in the medium in a frequency dependent manner. That is to say that each frequency component of light travels with a different speed in the medium. This frequency dependence of light propagation in a material is captured by expressing the speed of light in the medium in terms of its frequency-dependent refractive index:

$$v(\omega) = \frac{c}{n_{eff}(\omega)} = \frac{k_0 c}{\beta(\omega)} \tag{2.31}$$

where c is the vacuum speed of light, $n_{eff}(\omega)$ represents the frequency-dependent effective refractive index of the medium, k_0 is the vacuum wave number and $\beta(\omega)$ is the frequency-dependent propagation constant. $v(\omega)$ is known as the *phase velocity*, as it refers to the speed at which a plane wave – which is a monochromatic EM field of constant phase – propagates through the medium.

An optical pulse consists of a spectrum of frequencies of light propagating together. The information carried by the pulse travels at the *group velocity*, which is defined as follows [7]:

$$v_g(\omega) = \left(\frac{d\beta}{d\omega}\right)^{-1} = \frac{c}{d(\omega n)/d\omega} = \frac{c}{n_g} \tag{2.32}$$

where n_g is the group index:

$$n_g(\omega) = \frac{d(\omega n)}{d\omega} \tag{2.33}$$

For a given medium, $n(\omega)$ can be approximated using the well-known Sellmeier equation:

$$n^2(\omega) = 1 + \sum_{i=1} \frac{B_i \omega_i^2}{\omega_i^2 - \omega^2} \tag{2.34}$$

where ω_i are the resonance frequencies of the medium and B_i are the material constants. These parameters are estimated from experimental knowledge of material absorption resonances [7].

2.3.1.2 Waveguide Dispersion

The material dispersion effects outlined above reflects the frequency dependence of light propagation in any material, including the core of an optical fiber, and therefore applies to all modes propagating in a fiber in a similar manner. In addition to this effect, the waveguiding nature of an optical fiber also introduces a variation in propagation time and propagation constant from one spatial mode to another. This is known as waveguide dispersion, and can be understood intuitively using the ray picture as arising from the difference in ray paths traced by the modes. This can be seen, for example, in the dependence of the modal propagation constant $\tilde{\beta}_{lm}$ in a parabolic GRIN fiber on the azimuthal and radial indices l and m in Eq. 2.29.

2.3.1.3 Modeling Chromatic Dispersion

As mentioned above, optical pulses propagating in a multimode waveguide are subject to two different kinds of dispersion: material dispersion and waveguide dispersion. The combined effects of these are modeled via a Taylor series expansion of the modal propagation constant around the frequency of interest ω_0:

$$\beta^{(p)}(\omega) = n(\omega)\frac{\omega}{c} = \beta_0^{(p)} + \beta_1^{(p)}(\omega - \omega_0) + \frac{1}{2}\beta_2^{(p)}(\omega - \omega_0)^2 + ... \tag{2.35}$$

where the superscript (p) refers to the propagation constant of mode p. Note that the mode index p is merely a substitute for specifying the double indices l and m, for ease of notation. We will adopt this simpler mode indexing from now on, and specify the l and m where needed. In the equation above, n^{th} Taylor coefficient $\beta_n^{(p)}$ is given by:

$$\beta_n^{(p)} = \left(\frac{d\beta_n^{(p)}}{d\omega^n}\right)_{\omega=\omega_0} \tag{2.36}$$

Each of the Taylor coefficients has a physical significance. $\beta_0^{(p)}$ is the propagation constant of the mode at frequency ω_0. Note that at $\omega = \omega_0$, $\beta^{(p)}(\omega_0) = \beta_0^{(p)}$ is same as the propagation constant that we denoted as $\tilde{\beta_{lm}}$ in Section 2.2.1.

$\beta_1^{(p)}$, the first order coefficient, is the inverse of group velocity, as we saw in Eq. 2.32. Each mode has a different group velocity v_g, as a result of which a multimodal optical pulse spreads temporally as it propagates through a fiber. This is known as differential group delay (DGD).

The second order coefficient $\beta_2^{(p)}$ indicates the frequency-dependent variation of the group velocity around $\omega = \omega_0$. This is referred to as group velocity dispersion (GVD). $\beta_2 > 0$ is commonly known as the "normal" dispersion regime, while $\beta_2 < 0$ is known as the "anomalous" dispersion regime. The sign of β_2 signifies whether the β_2 term contributes to the spreading or compression of an optical pulse. As a result, the regime of dispersion at the operating wavelength is known from SMF NLFO to be crucially important to many nonlinear optical dynamics. For example, in SMF systems, solitons occur only in the anomalous dispersion regime as the effects of GVD and Kerr nonlinearity balance each other. Similarly, the appearance of spectral sidebands arising from modulation instability in the single mode propagation regime only occurs in the anomalous dispersion regime [11]. (Note, however, that this is no longer true when multiple spatial modes co-propagate [34, 36].)

For the purposes of this thesis, we only limit our discussion to the second order Taylor expansion. Third and higher orders of dispersion, in most cases, only need to be included when operating close to the zero dispersion wavelength of a fiber, where $\beta_2 = 0$ [11]. In our work,

we are justified in neglecting higher orders as we operate far away from the zero dispersion wavelength.

2.3.1.4 Propagation Losses

As with any waveguide, light propagating in a multimode fiber undergoes attenuation due to scattering and material absorption. This is typically modeled by allowing the medium's index of refraction to have a nonzero imaginary part:

$$n = n_{re} - in_{im} \tag{2.37}$$

where n_{re} and n_{im} are the real and imaginary parts of the refractive index. The field attenuation parameter is then given by [7]:

$$\alpha = k_0 n_{im} \tag{2.38}$$

such that the field magnitude after propagation through a length L_{prop} is given by $E(L) = E_0 e^{-\alpha L_{prop}}$. This attenuation parameter can be expressed in dB units as $\alpha_{dB} = 8.686\alpha$ [7]. At the wavelengths that we operate at (1064 nm and 1550 nm), $\alpha_{dB} < 1$ dB/km, and the typical fiber lengths in our experiments are only a few meters. As a result, the net attenuation experienced by the propagating EM wave is negligible for our purposes.

2.3.2 Nonlinear Pulse Propagation

2.3.2.1 Optical Nonlinearity

In classical electrodynamics described by Maxwell's equations, two electromagnetic waves pass through each other unaffected. This is also largely true of the quantum electrodynamic description of light, where two photons can interact in vacuum only when mediated by other (virtual) particles [55]. How, then, does one understand the light-light interaction that is characteristic of every nonlinear optical phenomenon? How do we explain, for example, cross-phase modulation where one light beam modulates the phase of another?

Admittedly, the way that I have phrased these statements is somewhat ambiguous. This is intentional, as it drives home the key point that is at the heart of nonlinear optics: the propagation medium serves as a "mediator" of sorts, facilitating light-light interaction. From this perspective, it is clear that the relationship between the electric field and the induced polarization in the medium is of central importance. In general, the induced polarization vector $\tilde{\mathbf{P}}$ depends upon the electric field vector $\tilde{\mathbf{E}}$, in the frequency domain, as [11]:

$$\tilde{\mathbf{P}}(\omega) = \varepsilon_0 \tilde{\chi}^{(1)}(\omega).\tilde{\mathbf{E}}(\omega) \tag{2.39}$$

where $\tilde{\chi}^{(1)}$ is known as the linear susceptibility tensor. Note that we have used the $\sim$ on top of the polarization and electric field vectors to denote the fact that the vectors are in the frequency domain, and so as to not confuse them for the time domain vectors we introduced in Section 2.2.1. In the Einstein summation notation, the equation above can be rewritten as:

$$\tilde{P}_j = \varepsilon_0 \tilde{\chi}^{(1)}_{jk} \tilde{E}_k \tag{2.40}$$

The susceptibility tensor relates to the refractive index of the medium as:

$$n^2(\omega) = 1 + \tilde{\chi}^{(1)}(\omega) \tag{2.41}$$

In the time domain, the relationship between the polarization and electric field vectors is no longer a simple product, but is rather described by a convolution integral:

$$P_j(t) = \varepsilon_0 \int_{-\infty}^{\infty} \chi_{jk}(\tau) E_k(t-\tau) d\tau \tag{2.42}$$

where $\chi(\tau)$ and $\tilde{\chi}(\omega)$ are Fourier transforms of each other.

It is clear from Eq. 2.40 that the relationship between the induced polarization vector and the electric field vector is a linear one. While this relationship holds when the optical intensity is low, the most general relationship between the two vectors involves the addition of higher order terms – for example, quadratic and cubic products of the electric field. On a physical level, the classical anharmonic oscillator model [11, 56] serves as a useful tool in understanding the nonlinear relationship between $\tilde{\mathbf{P}}$ and $\tilde{\mathbf{E}}$. (Strictly speaking, however, the anharmonic oscillator model is not an accurate description of the physics, and a semi-classical picture wherein the electric field is treated classically and the atoms in the medium quantum mechanically is a more accurate description. Reference [56] carries a discussion on this, for the interested reader.)

The more general relationship between $\tilde{\mathbf{P}}$ and $\tilde{\mathbf{E}}$, therefore, is given by:

$$\tilde{\mathbf{P}} = \varepsilon_0(\tilde{\chi}^{(1)} \cdot \tilde{\mathbf{E}} + \tilde{\chi}^{(2)} : \tilde{\mathbf{E}}\tilde{\mathbf{E}} + \tilde{\chi}^{(3)} \vdots \tilde{\mathbf{E}}\tilde{\mathbf{E}}\tilde{\mathbf{E}} + ...) \tag{2.43}$$

where $\tilde{\chi}^{(n)}$ is the nth order susceptibility tensor, and the products depicted by $\cdot$, : and $\vdots$ represent tensor products. In general, $\tilde{\chi}^{(n)}$ is a tensor of rank $(n+1)$ describing the nth order nonlinear relationship between $\tilde{\mathbf{P}}$ and $\tilde{\mathbf{E}}$.

As mentioned before, $\tilde{\chi}^{(1)}$ describes the linear response of a material, including refractive index $n(\omega)$ and attenuation α. $\tilde{\chi}^{(2)}$ describes second order nonlinear effects such as second harmonic generation, and sum- and difference-frequency generation [11]. $\tilde{\chi}^{(3)}$ represents third order nonlinear processes such as third harmonic generation, self- and cross-phase modulation and four-wave mixing.

In centrosymmetric materials such as SiO_2 (which is the most commonly used material for the core of an optical fiber), the second order nonlinear susceptibility tensor $\tilde{\chi}^{(2)}$ is zero. As a result, third order nonlinearity is the most significant contributor to the nonlinear response of the material [11, 56]. Although higher order responses exist, they can safely be neglected for the types of fibers and peak powers of optical pulses used in this work. We can therefore express the polarization in the fiber medium as a sum of the medium's linear and nonlinear (i.e. third order) contributions:

$$\tilde{\mathbf{P}} = \tilde{\mathbf{P}}_L + \tilde{\mathbf{P}}_{NL} \tag{2.44}$$

where $\tilde{\mathbf{P}}_L = \varepsilon_0\tilde{\chi}^{(1)} \cdot \tilde{\mathbf{E}}$ and $\tilde{\mathbf{P}}_{NL} = \varepsilon_0\tilde{\chi}^{(3)} \vdots \tilde{\mathbf{E}}\tilde{\mathbf{E}}\tilde{\mathbf{E}}$. In the Einstein summation notation, the third order nonlinear polarization can be expressed as:

$$\tilde{P}_j^{(3)} = \varepsilon_0 \tilde{\chi}_{jklm}^{(3)} \tilde{E}_k \tilde{E}_l \tilde{E}_m \tag{2.45}$$

2.3.2.2 Intensity Dependent Refractive Index

Before we begin our discussion on the multimode nonlinear Schrödinger equations, we briefly review a well-known nonlinear effect known as 'nonlinear refraction'. As we mentioned before, the induced polarization in a medium can be expressed as being proportional to the electric field in the medium according to Eq. 2.40. The proportionality constant is related to the refractive index as Eq. 2.41.

It turns out that this can also be done in the presence of $\tilde{\chi}^{(3)}$ terms as follows:

$$\tilde{\mathbf{P}} = \varepsilon_0 (\tilde{\chi}^{(1)} + \tilde{\chi}^{(3)} |\tilde{\mathbf{E}}|^2) \tilde{\mathbf{E}} \tag{2.46}$$

The difference here is that the proportionality factor is no longer a constant, and depends upon the intensity (which is proportional to $|\tilde{\mathbf{E}}|^2$). Following the definition of linear refractive index in Eq. 2.41, we can now define the intensity dependent – i.e. nonlinear – refractive index:

$$n(|\mathbf{E}|^2) = n + n_2 I \tag{2.47}$$

where n_2 is known as the nonlinear index coefficient for cubic nonlinearity, and it is proportional to $\tilde{\chi}^{(3)}$.

2.3.2.3 Generalized Multimode Nonlinear Schrödinger Equations

Having discussed the basic description of a medium's nonlinear response, we switch gears and begin our discussion of nonlinear propagation of a multimodal optical pulse. Pulse propagation in SMFs has been studied for decades using the nonlinear Schrödinger equation (NLSE) for a slowly varying pulse envelope [11]. Over time, additional terms were included to the single mode NLSE to describe higher order dispersion and stimulated Raman scattering (SRS) [57, 58], as well as the frequency dependence of the medium's nonlinear response by way of a time derivative operator called the self-steepening term [59]. This resulted in a modified NLSE, referred to in literature as the 'generalized' NLSE (GNLSE).

In a landmark paper published in 2008, the single mode GNLSE was extended to the case of multiple co-propagating and nonlinearly interacting spatial modes in a fiber [60], resulting in the generalized *multimode* nonlinear Schrödinger equations (GMMNLSEs). The GMMNLSEs are derived by inserting Eq. 2.44 into Maxwell's equations:

$$\nabla \times \mathbf{E} = -\mu_0 \frac{\partial}{\partial t}\mathbf{H} \tag{2.48a}$$

$$\nabla \times \mathbf{H} = \varepsilon_0 n^2 \frac{\partial}{\partial t}\mathbf{E} + \frac{\partial}{\partial t}\mathbf{P}_{NL} \tag{2.48b}$$

where $\mathbf{P}_{NL}$ is the time domain cubic nonlinearity polarization vector, and is given by:

$$\mathbf{P}_{NL}(x,y,z,t) = \varepsilon_0 \chi^{(3)} \mathbf{E}(x,y,z,t) \int_{-\infty}^{\infty} R(t-t')|\mathbf{E}|^2 dt' \tag{2.49}$$

where we have assumed that the material's cubic nonlinear response is $\chi^{(3)}(t)$ is near instantaneous [11] – i.e. represented by a time-invariant tensor $\chi^{(3)}$ and delta functions in time, which were integrated over to result in Eq. 2.49. This assumption typically amounts to neglecting the contributions of molecular vibrations to $\chi^{(3)}(t)$, i.e. Raman scattering, which are typically slower. However, for silica fibers, the Raman response occurs over a time scale of 60-70 fs, yielding this assumption to be approximately correct for pulses longer than ~ 1 ps [11]. For such cases, the response function $R(t)$ is expressed as:

$$R(t) = (1 - f_R)\delta(t) + f_R h_R(t) \tag{2.50}$$

where $h_R(t)$ is the Raman response function and f_R is its fractional contribution to $R(t)$. For silica fibers, $f_R \approx 0.18$.

The electric field $\mathbf{E}$ at some longitudinal position z can be expressed in terms of the bound modes of a multimode fiber according to Eq. 2.1 as:

$$\mathbf{E}(x, y, z, t) = \sum_p \mathbf{e}_p(x, y) A_p(z, t) e^{-i\omega t} \tag{2.51}$$

where the $e^{i(\beta_0^{(p)} z)}$ accumulation of z-dependent phase is absorbed into the definition of the slowly-varying pulse envelope $A_p(z, t)$ for the pth mode. As before, $\mathbf{E}_p(x, y, z)$ refers to the full electric field vector corresponding to mode p, $\mathbf{e}_p(x, y)$ is the modal electric field profile describing the transversal variation of the transverse and longitudinal components.

The GMMNLSEs are obtained by substituting Eq. 2.51 into Eq. 2.49. We will not show the derivation here as it is beyond the scope of this thesis, but the reader is encouraged to review the derivations in References [60] and [61]. The GMMNLSEs are given by:

$$\partial_z A_p(z,t) = i\Big(\beta_0^{(p)} + i(\beta_1^{(p)} - \beta_1^{(1)})\partial_t + \sum_{n\geq 2} i^n \frac{\beta_n^{(p)}}{n!}\partial_t^n\Big)A_p(z,t) + i\frac{n_2\omega}{c}\mathscr{N} \tag{2.52}$$

where $\beta_n^{(p)}$ is, as before, the nth order Taylor expansion coefficient of $\beta^{(p)}$, ∂_z and ∂_t denote the partial derivatives with respect to z and t respectively. Note that the subtraction terms involving $\beta_0^{(1)}$ and $\beta_1^{(1)}$ signify that the equations are written in the frame of reference of the fundamental mode. The nonlinear term $\mathscr{N}$ is given by:

$$\mathscr{N} = \mathscr{N}_1 + \mathscr{N}_2 \tag{2.53}$$

where:

$$\mathscr{N}_1 = \sum_{hkm} 2Q_{phkm}^{(1)} A_p(z,t) \int R(t')A_k(z,t-t')A_m^*(z,t-t')dt' \tag{2.54a}$$

$$\mathscr{N}_2 = \sum_{hkm} Q_{phkm}^{(2)} A_p^*(z,t) \int R(t')A_k(z,t-t')A_m(z,t-t')e^{2i\omega_0 t'}dt' \tag{2.54b}$$

where the overlap integrals $Q_{phkm}^{(1)}$ and $Q_{phkm}^{(2)}$ are, in general, frequency dependent, and are expressed as:

$$Q_{phkm}^{(1)}(\omega) = \frac{\varepsilon_0^2 c^2 n_{co}^2 \int\int (\mathbf{e}_p^*(x,y,\omega)\cdot\mathbf{e}_m(x,y,\omega))(\mathbf{e}_k(x,y,\omega)\cdot\mathbf{e}_h^*(x,y,\omega))dxdy}{12N_p(\omega)N_h(\omega)N_k(\omega)N_m(\omega)} \tag{2.55a}$$

$$Q_{phkm}^{(2)}(\omega) = \frac{\varepsilon_0^2 c^2 n_{co}^2 \int\int (\mathbf{e}_p^*(x,y,\omega)\cdot\mathbf{e}_h^*(x,y,\omega))(\mathbf{e}_m(x,y,\omega)\cdot\mathbf{e}_k(x,y,\omega))dxdy}{12N_p(\omega)N_h(\omega)N_k(\omega)N_m(\omega)} \tag{2.55b}$$

where $N_j(\omega)$ is the mode normalization constant defined as:

$$\int\int (\mathbf{e}_j(x,y,\omega) \times \mathbf{h}_k^*(x,y,\omega)) \cdot \hat{\mathbf{z}} dxdy = 2\delta_{jk} N_j^2(\omega) \tag{2.56}$$

Eq. 2.52 is the full GMMNLSE that includes Kerr and Raman nonlinearities as well as higher order dispersion terms up to an arbitrary order. Self-steepening terms were neglected as we do not work with ultrashort pulses and only focus on nanosecond pulses in this thesis. We now further simplify Eq. 2.52 by making the following assumptions that apply for the experiments that we report in Chapter 4:

- Firstly, we neglect the contribution by stimulated Raman scattering as we work with very short ($\sim$ 1 m long) fibers and nanosecond pulses with peak powers below $\sim 15 - 20$ kW. This amounts to setting $f_R = 0$ in Eq. 2.50.

- Because we work in a regime where the output optical spectra that we report in Chapter 4 remain narrow and the majority of the power remains at the input laser frequency ω_0, we evaluate the modal field profiles $\mathbf{e}_j$ as well as the overlap coefficients $Q^{(1)}_{phkm}$ and $Q^{(2)}_{phkm}$ only at ω_0.

- We also limit our discussion to the second order Taylor coefficient of dispersion $\beta_2^{(p)}$ as we operate far from the zero dispersion wavelength of our fiber [11].

- And finally, we adopt the following mode normalization:

$$\int\int |\mathbf{e}_p(x,y)|^2 dxdy = 1 \tag{2.57}$$

where we follow the dot product convention for a general 3 dimensional vector with complex components $\mathbf{v}$:

$$|\mathbf{v}|^2 = \mathbf{v}^* \cdot \mathbf{v} = |v_x|^2 + |v_y|^2 + |v_z|^2 \tag{2.58}$$

With this mode normalization, the instantaneous optical power (in Watts) in the pth mode at some position z along the fiber is given by:

$$PW_p(z,t) = \frac{n_{eff,p} c \varepsilon_0}{2} |A_p(z,t)|^2 \tag{2.59}$$

where we denote optical power by PW to avoid confusion with the notation for the induced polarization P from Section 2.3.2.1. Note that the relation in Eq. 2.59 is different from what is typically used in literature and in SMF NLFO, where the instantaneous power is given simply by $|A_p(z,t)|^2$. This is a result of the way in which we have chosen to normalize the spatial modes in Eq. 2.57. Either picture is equally correct so long as the mode normalization and the expression for instantaneous power are consistent with each other.

We now rewrite the simplified GMMNLSEs that we use for the remainder of this thesis, based on the aforementioned simplifications:

$$\partial_z A_p(z,t) = i\left(\beta_0^{(p)} + i\delta\beta_1^{(p)}\partial_t - \frac{\beta_2^{(p)}}{2}\partial_t^2\right) A_p(z,t) + i\frac{n_2\omega_0}{c}\mathcal{N}_{phkm} A_h^* A_k A_m \tag{2.60}$$

where $\delta\beta_1^{(p)} = \beta_1^{(p)} - \beta_1^{(1)}$. The nonlinear term $\mathcal{N}_{phkm}$ is now given by:

$$\mathscr{N}_{phkm} = \frac{2}{3}\int\int(\mathbf{e}_p^* \cdot \mathbf{e}_m)(\mathbf{e}_k \cdot \mathbf{e}_h^*)dxdy + \frac{1}{3}\int\int(\mathbf{e}_p^* \cdot \mathbf{e}_h^*)(\mathbf{e}_k \cdot \mathbf{e}_m)dxdy \tag{2.61}$$

where, as mentioned before, $\mathbf{e}_j$ are now assumed to not depend on ω.

We now discuss the significance of the various terms that emerge from $\mathscr{N}_{phkm}A_h^*A_kA_m$, before concluding the chapter with a note on numerically solving the GMMLSEs Eqs. 2.52 and 2.60.

2.3.2.4 Self-Phase Modulation

We first examine the role of the $\mathscr{N}_{phkm}A_h^*A_kA_m$ terms that take the shape $|A_p|^2A_p$. In order to understand the significance of the $|A_p|^2A_p$ terms, it is helpful to consider the single mode propagation regime. For the purpose of this illustration, we also assume that the pulse has a narrow bandwidth so as to allow us to neglect cross-coupling terms between different frequencies. The NLSE including Kerr nonlinear effects then reduces to:

$$\partial_z A = -i\frac{\beta_2}{2}\partial_t^2 A(z,t) + i\frac{n_2\omega_0}{cA_{eff}}|A|^2A \tag{2.62}$$

where A_{eff} refers to the effective area of the single spatial mode, and is simply the inverse of $\mathscr{N}_{phkm}$ for $p = h = k = m$. To see the effect of $|A|^2A$ term, let us neglect for a moment the β_2 term. That leaves us with:

$$\partial_z A = i\frac{n_2\omega_0}{cA_{eff}}|A|^2A \tag{2.63}$$

This equation can be solved analytically upon recognizing that $|A|^2(z,t)$ is a constant as a

function of z. This can be shown by calculating the derivative $\frac{d}{dz}|A|^2$ and seeing that it is equal to 0. The analytical solution to the single mode NLSE above then simply becomes:

$$A(z,t) = A(0,t)e^{i\gamma|A|^2 z} \tag{2.64}$$

where $\gamma = \frac{n_2\omega_0}{cA_{eff}}$. As the solution shows, the $|A|^2A$ term results in a phase modulation of $A(z,t)$. In other words, the pulse modulates its own phase – as a result of the nonlinear response of the material – as it propagates through the fiber. This is known as 'self phase modulation' (SPM).

SPM has the effect of introducing a chirp in the pulse. This is seen by recognizing that $|A|^2(t)$ is time-varying for non-square pulses. As a result, the pulse at some position z acquires a time-dependent phase given by $\Gamma(t) = \gamma|A|^2(t)z$. The total phase of the pulse, upon adding the contributions from the $e^{i(\omega_0 t - \beta z)}$ term that we factored out becomes:

$$\Phi(t) = \Gamma(t) + \omega_0 t - \beta z \tag{2.65}$$

The instantaneous frequency is then given by the time derivative of the phase. This yields:

$$\Omega(t) = \partial_t\Phi(t) = \omega_0 + \partial_t\Gamma(t) \tag{2.66}$$

Unless the pulse has a shape such that $\partial_t\Gamma(t) \propto \partial_t|A|^2(t) = 0$, this result shows that SPM has the effect of not only chirping the pulse in the time domain, but also that of adding new frequencies in the spectral domain. It is worth emphasizing that the additional frequencies generated due to SPM are only generated because the nonlinear coefficient of the material $n_2 \neq 0$. Also, the

additional frequencies generated due to nonlinearity are dependent upon the instantaneous power given by $PW(t) \propto |A|^2(t)$, where, as before, we denote the power in the signal by PW. This dependence on power is a signature of all nonlinear effects, including SPM.

2.3.2.5 Cross-Phase Modulation

Having discussed the effect of SPM arising from the $|A_p|^2 A_p$ terms in the NLSE, we now examine the role of $|A_h|^2 A_p$ terms where $h \neq p$. Similar to the SPM terms, the $|A_h|^2 A_p$ terms result in a phase modulation of A_p. However, in this case, the modulating phase is given by:

$$\Gamma_p(t) = 2\gamma' |A_h|^2(t) z \tag{2.67}$$

where $\gamma' = \frac{n_2 \omega_0}{c} \mathscr{N}_{hhpp}$, and the multiplicative factor 2 arises from the fact that multiple combinations of $phkm$ can yield to the same $\mathscr{N}_{phkm}$ values as well as to $|A_h|^2 A_p$ terms. Here, because the phase of one spatial mode is modulated by the power in a different mode, this phenomenon is known as 'intermodal cross phase modulation', or simply 'cross phase modulation' (XPM). Note that a similar effect also occurs between two co-propagating beams that are at different frequencies or in orthogonal polarization states, for example in SMFs [11].

It is also worth noting that intermodal XPM cannot lead to the exchange of energy between two modes because of the same arguments as we used in the SPM case – namely that $\frac{d}{dz}|A|_p^2$ can still be shown to be equal to 0.

2.3.2.6 Intermodal and Intramodal Four Wave Mixing

All other terms remaining in the NLSE that do not take the form of SPM or XPM terms are commonly referred to as "four wave mixing" (FWM) terms. This is because these terms can lead to the interaction of 4 potentially different waves through the $\mathscr{N}_{phkm}A_h^*A_kA_m$ terms. Unlike the SPM and XPM terms, however, FWM terms can lead to the exchange of energy between different spatial modes.

FWM terms can take the form, in the NLSE for $\partial_z A_p$, of $A_h^*A_kA_m$ where $h \neq k \neq m$, or more commonly, $A_p^*A_h^2$ where $h \neq p$. In the presence of such terms, it can be shown that $\frac{d}{dz}|A|_p^2 \neq 0$, meaning that energy can flow out of or into the interacting modes from or to other modes.

In order to see the conditions under which FWM terms lead to exchange of energy, it is useful to perform the variable substitution $A_p(z,t) \rightarrow A_p(z,t)e^{i\beta_0^{(p)}z}$. We will not dwell on the derivation here, but the nonlinear terms in the NLSEs Eq. 2.60 can be shown to then take the form $\mathscr{N}_{phkm}A_h^*A_kA_me^{i\Delta\beta_{phkm}z}$ [62], where the $\Delta\beta_{phkm}$ is referred to as the 'phase mismatch' and is given by:

$$\Delta\beta_{phkm} = \beta_0^{(k)} + \beta_0^{(m)} - \beta_0^{(p)} - \beta_0^{(h)} \tag{2.68}$$

For some $\Delta\beta_{phkm} \neq 0$, there is "beat length" for the nonlinear FWM term that is given by $1/\Delta\beta_{phkm}$. If the propagation length z is such that $\Delta\beta_{phkm}z \gg 1$, then the $e^{i\Delta\beta_{phkm}z}$ term amounts to a rapidly varying phase term that averages out to 0. In other words, the $A_h^*A_kA_m$ term corresponding to that $\Delta\beta_{phkm}$ is not phase matched.

Note that in reality, the phase mismatch term is more accurately given by:

$$\Delta\beta_{phkm} = \beta_0^{(k)} + \beta_0^{(m)} - \beta_0^{(p)} - \beta_0^{(h)} + \Delta\beta_{NL} \tag{2.69}$$

where the term $\Delta\beta_{NL}$ accounts for the fact that all the $\beta_0^{(p)}$s are usually calculated in the low power regime, but at higher powers the index profile of the fiber itself – and by extension the propagation constants of the modes that it supports – is modified by the nonlinearity via the intensity-dependent index change discussed in Section 2.3.2.2. However, in most cases, this term can be neglected at either low input powers or if the resulting change in propagation constants for all 4 modes cancel out.

Note that in the above, we have assumed that we are working with long optical pulses that are spectrally narrow. In such a case, all the FWM processes involve multiple spatial modes. This is known as 'inter-modal four wave mixing' (IMFWM). In the presence of spectrally broad pulses, however, FWM processes can occur all within one spatial mode but involve different frequencies, or with different frequencies from different spatial modes. In such as case, the FWM process needs to be matched in phase as well as energy, requiring:

$$\omega_1 + \omega_2 - \omega_3 - \omega_4 = 0 \tag{2.70a}$$

$$\Delta\beta = \beta_0(\omega_1) + \beta_0(\omega_2) - \beta_0(\omega_3) - \beta_0(\omega_4) + \Delta\beta_{NL} = 0 \tag{2.70b}$$

where we adopt a simple numbering of the 4 waves involved, to avoid confusion with the $phkm$ notation that we have thus far used for spatial modes all at the same frequency.

Within the scope of this thesis, we do not focus on this type of intramodal + intermodal FWM, as we work with spectrally narrow pulses, but References [63, 64] are recommended readings on this subject.

2.3.2.7 Raman Scattering

Although we do not investigate nonlinear phenomena in this work in a regime where the Raman terms play a significant role, it is worthwhile to discuss it here nevertheless. When a photon is incident on a molecule in a given propagation medium, the molecule can scatter the photon in an inelastic manner – i.e. in a manner that does not conserve the energy of the photon. This results in the photon that emerges from the collision to have a lower energy (equivalently, frequency) as compared to the incident photon. This process is known as Raman scattering.

As we mentioned in Sections 2.3.2.1 and 2.3.2.3, this process is modeled by the delayed Raman response function $h(t)$. By its inelastic nature, Raman scattering is a dissipative process. It has been demonstrated that Raman scattering is at the core of many nonlinear phenomena, for example single mode and multimode Raman solitons [65, 66] and Raman beam cleanup in parabolic GRIN fibers [67].

2.3.3 Tools for Solving the NLSEs

Numerically solving the coupled NLSEs Eqs. 2.52 or 2.60 can be greatly useful in gaining insight into the many complex processes that are allowed by the equations. For the work presented in this thesis, we have developed and adopted a numerical code that can solve for the spatial modes of a fiber with any given refractive index profile, and simulate the nonlinear

propagation by solving Eqs. 2.60 using the well-known split-step Fourier method (SSFM). Open source code packages for SSFM are available [68].

SSFM involves integrating half a step of the linear terms in the frequency domain, then performing a Fourier transform and integrating the nonlinear terms in the time domain, then performing an inverse Fourier transform and integrating another half a step of the linear terms in the frequency domain. Because of the availability of numerical Fourier transform algorithms using the discrete Fourier transform (DFT) on most programming platforms including Python and MATLAB®, such as the fast Fourier transform (FFT) algorithm, the SSFM is a very efficient method when working with a small number of modes ($\sim$ 1-30).

In the presence of higher number of modes, the number of cross-coupling terms scales as the 4^{th} power of the number of modes. This is because the nonlinear coupling terms in Eqs. 2.52 contain 4 indices. In such cases, it becomes computationally advantageous to simulate the nonlinear propagation using the (3+1)D GNLSE involving the full 3-dimensional electric field vector (discussed, for example, in [17]). Note that solving the (3+1)D equation is also most useful when working with spectrally broad pulses. In the modal equations, one has to solve for modes as various different frequencies and calculate cross-coupling terms for all possible combinations of spatial modes and frequencies. This is avoided by simply solving for the nonlinear evolution of the full (3+1)D electric field and resolving for modes as needed at the end of the propagation.

In other cases, however, when the number of spatial modes present is large but the optical spectrum is not necessarily broad, it can still be helpful to solve the coupled NLSEs in an efficient manner. This is useful, for example, in simulating the Kerr-induced beam cleanup effect reported in References [14, 15]. For such use cases, a GMMNLSE solver based on a Massively Parallel Algorithm has been reported in Reference [69] and is publicly available.

Chapter 3: Time-Domain Interference Patterns of Nonlinearly Interacting LP_{0m} Modes of a Parabolic GRIN MMF

3.1 (Re-)motivation

As we mentioned in Chapter 1, one of the main objectives of our research has been to probe the interactions between a small number of spatial modes. There continue to be a number of research efforts across the globe that continue to examine the "macroscopic" thermodynamic effects involving a large number of modes, but one of the deliberate choices that we have made throughout the course of our work has been to ask the more fundamental questions: can we experimentally verify and validate the basic theory underlying this research field? Can we produce experimental measurements that can be directly – and at times quantitatively and not just qualitatively – compared with numerical simulations and analytical predictions? Are there new physical nonlinear phenomena that are unique to multimode fibers that we can observe even in the presence of a small number of modes? Can we design controlled experiments that help us better understand the effects of each of the terms in GMMNLSEs Eqs. 2.60?

Of course, as is true with a good part of research in the optical sciences, a lot of what we have done has also been quite exploratory. But these questions have served as useful guiding principles for us in determining the types of experiments in which we are interested. This could

also serve as a valuable perspective for the reader with which to analyze the work presented in Chapters 3-7.

3.2 Chapter Overview

Having established the theoretical framework and numerical tools for understanding spatiotemporal nonlinear optical effects occurring in multimode fibers in Chapter 2, in this and the next few chapters, we will describe our work on experimental investigation of power-dependent spatiotemporal effects in the three types of fibers that we alluded to in Chapter 2: parabolic GRIN MMF, step-index FMF and hollow RCF.

In this chapter, we discuss our very first experiments that involved nonlinearly interacting radially symmetric LP_{0m} modes of a parabolic GRIN fiber. We first write down the coupled NLSEs, based upon the GMMNLSEs that we developed in Section 2.3.2.3, and discuss our experimental methodology. As we will see in Chapter 4, this experiment laid the foundation for the novel tools that we developed for subsequent experiments. In some sense, therefore, the shortcomings of the experiments reported in this chapter serve as motivation for the improved version of our experiment that we discuss in Chapter 4. Having outlined the theory and the experimental methodology, we then conclude the chapter by comparing numerical simulation results with experimental findings.

3.3 Coupled NLSEs

One of the first questions that we asked for our first experiment was: what is the easiest way to excite a combination of spatial modes in an MMF in such a way that the mode superposition

can be controlled to some degree? The answer was to work with the radially symmetric LP_{0m} modes of the fiber, as a combination of these can be excited by aligning the axis of the fiber's input end-face with that of a focused Gaussian laser beam. The mode superposition is controlled by adjusting the spot size of the free-space beam, i.e. by controlling the focal length of the focusing lens.

> *Note*: Although we use the LP mode notation to denote the radially symmetric modes that we describe in Chapters 3 and 4, we reiterate that for $l = 0$, the LP modes are completely equivalent to the hybrid modes denoted by HE and EH modes (see Table 2.1). It is only for $l \neq 0$ that, as we discussed in Chapter 2, the LP modes are not true propagation modes of the fiber. Our choice to use the LP_{0m} mode notation here, as opposed to the fully equivalent HE_{1m} notation, is purely for convenience and for denoting the fact that we work with linear polarized light throughout the experiments and analysis.

In order to get a sense for what we should expect to see when we excite a combination of the radially symmetric LP_{0m} modes in a parabolic GRIN fiber, we revisit the coupled NLSEs first in the linear domain and then in the nonlinear domain. In the absence of any nonlinearity, i.e. at low input powers, we neglect the nonlinear $\mathscr{N}_{phkm}$ terms in Eqs. 2.60 to get:

$$\partial_z A_p(z,t) = i\left(\delta\beta_0^{(p)} + i\delta\beta_1^{(p)}\partial_t - \frac{\beta_2^{(p)}}{2}\partial_t^2\right)A_p(z,t) \tag{3.1}$$

The $\delta\beta_1^{(p)}$ term represents DGD. In the presence of multiple co-propagating spatial modes, it models the temporal broadening of a pulse arising from DGD. The $\beta_2^{(p)}$ term represents group velocity dispersion (GVD), and it changes the phase of each spectral component present in the initial optical pulse. Although this term does not by itself modify the pulse spectrum, it often leads to the temporal broadening of pulses. The remaining first terms in the equations represent

propagation constant mismatch between the modes. For any arbitrary number of spatial modes propagating in a parabolic GRIN fiber, the (approximately) uniform spacing of modal propagation constants shown in Fig. 2.4 leads to the spatial profile exhibiting a periodic oscillation in its spatial profile along the z direction. This is illustrated in Fig. 3.1. The periodicity of this self-imaging phenomenon is given by the self-imaging distance $z_{si} = \frac{\pi a}{\sqrt{2\Delta}}$. As mentioned previously, this self-imaging phenomenon has been shown to lead to unique nonlinear phenomena such as the geometric parametric instability, where the self-imaging effect leads to a Kerr-induced refractive index grating along the z direction [17].

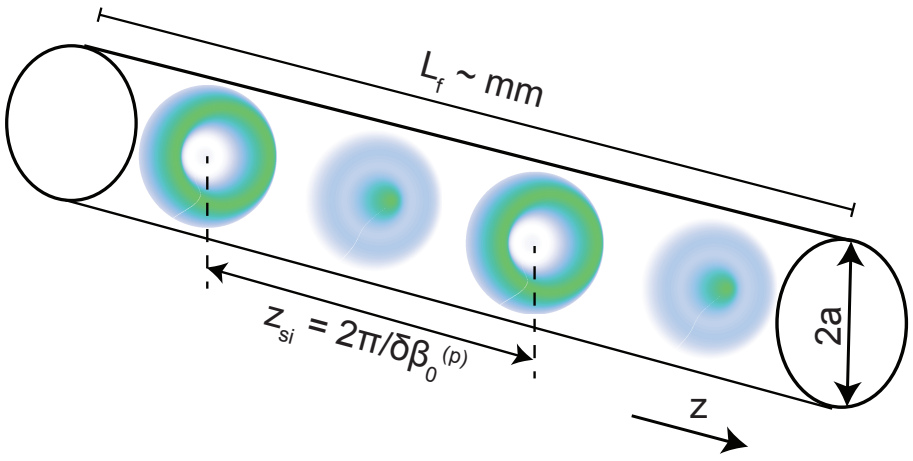

Figure 3.1: Illustration of the self-imaging effect in a parabolic GRIN fiber. For conditions in which all terms in the coupled NLSEs except for the propagation constant mismatch terms can be neglected, the spatial beam pattern exhibits a periodic oscillation along z.

As before, we perform the variable transformation:

$$A'_p(z,t) = A_p(z,t)e^{-i\beta_0^{(p)}z} \tag{3.2}$$

The GMMNLSEs can then be rewritten as:

$$\partial_z A'_p = (-\delta\beta_1^{(p)}\partial_t - i\frac{\beta_2^{(p)}}{2}\partial_t^2)A'_p + i\frac{n_2\omega_0}{c}\mathscr{N}_{phkm}A'^{*}_h A'_k A'_m e^{i\Delta\beta_{phkm}} \tag{3.3}$$

where, as before, $\Delta\beta_{phkm} = \beta_0^{(k)} + \beta_0^{(m)} - \beta_0^{(p)} - \beta_0^{(h)}$. For an input mode combination that consists of only the LP_{0m} modes, the surviving terms are the ones for which $\Delta\beta_{phkm} = 0$ (phase matching) as well as $\mathscr{N}_{phkm} \neq 0$. Upon imposing the resulting selection rules, we obtain the following coupled NLSEs:

$$\partial_z A'_p = (-\delta\beta_1^{(p)}\partial_t - i\frac{\beta_2^{(p)}}{2}\partial_t^2)A'_p + i\frac{n_2\omega_0}{c}(\mathscr{N}_{pppp}|A'_p|^2 + 2\sum_{h\neq p}\mathscr{N}_{pphh}|A'_h|^2)A'_p \tag{3.4}$$

Note that the uniform spacing of the propagation constants can sometimes phase match other terms as well, however, it is worth reiterating that the spacing of propagation constants is only approximate. A more exact calculation reveals that the spacing is non-uniform, and FWM terms "average out" if the product $\Delta\beta_{phkm}z \gg 1$. For our experimental parameters, we found this to be true.

The resulting coupled equations, Eqs. 3.4, consist of only the SPM and XPM terms. This can be shown to mean that $\frac{d}{dz}|A_p|^2 = 0$ – in other words, there is no permanent energy exchange between the spatial modes. Furthermore, we can momentarily neglect the $\delta\beta_1^{(p)}$ and $\beta_2^{(p)}$ terms to write down a simple analytical solution. This is justified for our experimental parameters as we work with short fiber lengths and long pulses – a regime in which the effects of DGD and GVD are minimal [11]. Specifically, the dispersion length can be estimated as:

$$L_D = T_0^2/|\beta_2| \tag{3.5}$$

where T_0 is the width of the optical pulse, and we have dropped the index p from the modal GVD parameter as all modes in this fiber have approximately equal β_2. (This can be seen from differentiating Eq. 2.30 twice with respect to frequency ω.) For our fiber modes, we find that $\beta_2 \approx -27.95$ fs^2/mm. For a pulse width $T_0 \approx 2$ ns, L_D evaluates to the order of 10^8 meters, which is much larger than the fiber length $L_f \approx 40$ m. In other words, the impact of the $\beta_2^{(p)}$ terms can be neglected. Similarly, the temporal spread arising from DGD, estimated as $\delta\beta_1^{(p)} L_f$, evaluates to ≈ 1 ps, which is much smaller than the width of the optical pulse used in our experiments, which is ≈ 2 ns.

With these simplifications, the analytical solution is given as:

$$A'_p(z,t) = A'_p(0,t)e^{i\Gamma_p(t)z} \tag{3.6}$$

In terms of $A_p(z,t)$, we have:

$$A_p(z,t) = A_p(0,t)e^{i\beta_0^{(p)}z}e^{i\Gamma_p(t)z} \tag{3.7}$$

where:

$$\Gamma_p(t) = \frac{n_2\omega_0}{c}(\mathscr{N}_{pppp}|A_p|^2 + 2\sum_{h\neq p}\mathscr{N}_{pphh}|A_h|^2) \tag{3.8}$$

The modes therefore acquire a nonlinear phase shift that is proportional to the square magnitudes of the pulse amplitudes. More specifically, each mode acquires a different nonlinear phase

shift that is determined by the input power distribution in the modes and the different $\mathcal{N}_{pppp}$ and $\mathcal{N}_{pphh}$ parameters. In Fig. 3.2, we illustrate an example result of a *spatiotemporal* overlap of two modes. We show what the on-axis pulse might look like for two spatially overlapping modes that have acquired different nonlinear phase shifts. The instantaneous phase with which the pulses interfere varies with time, resulting in time-domain fringes.

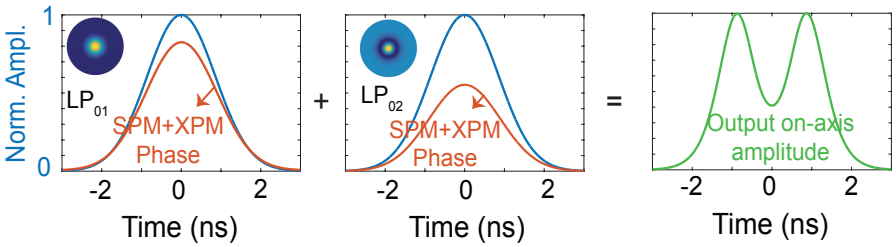

Figure 3.2: Illustration of the creation of time-domain interference fringes arising from differential nonlinear chirps acquired by overlapping spatial modes in a parabolic GRIN fiber. We show an example case for two overlapping LP_{0m} modes. The inset images show the numerically calculated mode intensity profiles. The instantaneous phase with which the pulses in the two modes overlap varies with time, resulting in the time dependence.

3.4 What Does 'Spatiotemporal' Mean?

In order to better appreciate the *spatiotemporal* nature of this phenomenon, it is helpful to write down the expression for the full spatiotemporal field profile emerging from the fiber using Eq. 2.51. Upon dropping the $e^{i\omega_0 t}$ term from Eq. 2.51 for simplicity, and upon using the transverse mode profile functions for LP modes $e_{x,p}(x,y) = \Psi_p$ from Section 2.2.5, we have:

$$E(x,y,z,t) = \sum_p \Psi_p(x,y) A_p(z,t) \tag{3.9}$$

Upon using the analytical solution $A_p(z,t)$ from Eq. 3.7, we can rewrite this equation as:

$$E(x,y,z,t) = \sum_p \Psi_p(x,y) A_p(0,t) e^{i\beta_0^{(p)} z} e^{i\Gamma_p(t) z} \tag{3.10a}$$

$$E(x,y,z,t) = \sum_p \Psi_p(x,y) \sqrt{\eta_p} A_0(t) e^{i\beta_0^{(p)} z} e^{i\Gamma_p(t) z} \tag{3.10b}$$

where $A_0(t)$ describes the input pulse amplitude of the free-space beam that we launch into the fiber and η_p represents the fraction of the overall power that is launched into the pth spatial mode. In other words:

$$A_p(z=0,t) = \sqrt{\eta_p} A_0(t) \tag{3.11}$$

Notice that in the absence of the nonlinear term, i.e. if $\Gamma_p = 0$, the terms on the right hand side of Eqs. 3.10 can be separated into spatial and temporal parts as $E = A_0(t)(\sum_p \Psi_p(x,y)\sqrt{\eta_p} e^{i\beta_0^{(p)} z})$. In other words, the spatial pattern does not depend upon time, and the temporal shape is independent of the spatial coordinates.

However, this separation is *not* possible when $\Gamma_p \neq 0$. The $A_0(t)$ can of course still be factored out, but the remaining terms in the summation would still depend upon all four coordinates: x, y, z as well as t. That is to say that the spatial pattern depends upon time, and the temporal shape of the pulse depends upon where in the transverse coordinates the pulse is measured. This intermingling of spatial and temporal coordinates is unique to multimode fiber nonlinear optics, and is at the heart of what causes these effects to be *spatiotemporal*.

In the following section, we discuss the results of our experiments that conclusively demon-

strate this spatiotemporal nature.

3.5 Experiments

In Fig. 3.3(a), we show a simplified schematic of our experimental setup. For our initial experiments, we used a fiber-based master oscillator power amplifier (MOPA) laser manufactured by NuPhoton®. The laser generated $\sim$ 2 ns optical pulses at 1550 nm with energies in the order of μJ, i.e. peak powers of the order of kW. The Gaussian laser beam is focused onto the input end-face of a $2a = 62.5$ μm parabolic GRIN fiber with a spot size of approximately 49 μm. The fiber's input end-face was placed on a translation stage to allow for fine-tuning of the relative displacement between the fiber axis and the incident Gaussian beam. Upon careful alignment, the beam was aligned to be incident on-axis, which is expected to excite a combination of 9 LP_{0m} with the power distribution shown in Fig. 3.3(c).

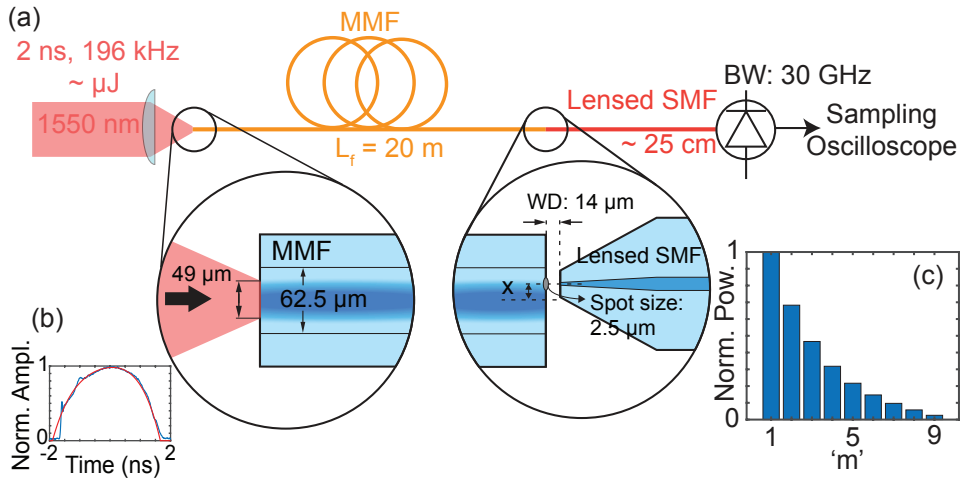

Figure 3.3: (a) Experimental setup for measuring time-domain interference fringes arising from nonlinearly interacting LP_{0m} modes of a parabolic GRIN fiber. (b) (Blue) time-domain measurement of the optical pulse launched into the fiber, (Red) parabolic fit. (c) Calculated launch modal powers of the combination of LP_{0m} modes.

At the output end of the MMF, we sampled the output spatiotemporal profile at various lateral displacements x by using a lensed fiber that has a collection spot size of $\approx$ 2.5 μm. We translate the lensed fiber across the MMF's output end-face to measured the time domain waveform at various values of x using a high bandwidth sampling oscilloscope.

3.6 Results and Discussion

As we discussed before, we can make the following predictions based on Eq. 3.10:

1. The measured temporal pulse profile would depend upon the transverse coordinates x and y
2. Equivalently, the spatial intensity pattern varies with time t

In Fig. 3.4, we demonstrate the variation of the measured pulse profile with the transverse coordinates. The pulse emerging from the fiber was sampled at various values of x, for input pulse energies of $\approx$ 5.2 μJ, corresponding to a peak power of $\approx$ 4kW, for two cases of fiber lengths, 20 and 40 meters.

Firstly, these measurements demonstrate the spatial variation of the pulse shape, as predicted by Eq. 3.10. For the $L_f = 20$ m case, for example, the pulse at $x = 0$ shows distinct temporal fringes with a significant fringe depth, while the pulse measured at, say, $x = 3.84$ μm do not show strong fringes. Secondly, at longer lengths of fiber, because of higher accumulated nonlinearity, we expect to see more temporal fringes. This is seen in Fig.3.4(b). And finally, for both fiber lengths, Fig. 3.4 shows a broad agreement of numerical simulations and experimental observations. Note that the numerical simulations presented here also included the $\delta\beta_1^{(p)}$

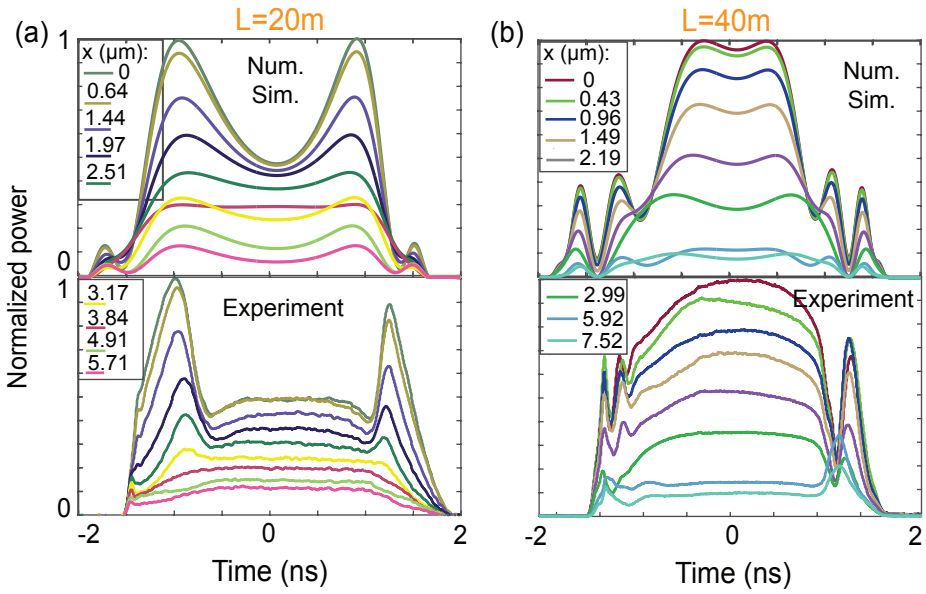

Figure 3.4: Experimental observations and numerical simulations of time-domain interference arising from nonlinearly interacting LP_{0m} modes of a parabolic GRIN fiber. (a) Simulations (top) and experimental measurements (bottom) for fiber length $L_f = 20$ m. (b) Simulations (top) and experimental measurements (bottom) for fiber length $L_f = 40$ m. In both cases, the optical pulse emerging from the fiber is sampled at different x, and the pulse amplitudes are normalized to the peak of the pulse at $x = 0$. Input pulse energy for both cases is ≈ 5.2 μJ.

and $\beta_2^{(p)}$ terms in the NLSEs. The temporal pulse shape used in the simulations corresponds to a transform-limited parabolic pulse fit of the experimentally measured optical pulse exiting the laser source, although the laser likely produced chirped pulses resulting from the fact that it consisted of a few meters of a fiber amplifier.

With these initial experiments, we were able to definitively prove the first of the aforementioned predictions made by Eq. 3.10. The second prediction follows automatically, because a spatial variation of the local time-domain pulse shape is equivalent to a temporal variation of the spatial pattern. However, the shortcomings of our measurements did not allow us to demonstrate this temporal variation in an elegant enough manner.

Additionally, the laser that we used produced pulses that did not seem to be fully transform-limited, and consisted of a short gain-switching peak as shown in Fig. 3.3(b). This resulted from the fact that the device consisted of a long ~ 1 m section of erbium-doped fiber amplifier followed by a single mode fiber before the beam emerged into free space, which would have caused nonlinear chirping and distortion of the pulse.

Another shortcoming of these experiments relate to the mode excitation. Although we could adjust the mode excitation by adjusting the spot size, this method still only provides fairly limited control on what modes are excited. Ideally, in order to study the nonlinear interactions between individual modes, we require a method to control the modes excited in a fiber.

We address all of these issues in the experiments presented in Chapter 4, where we demonstrate the first reported complete spatiotemporal intensity measurements of multimodal nonlinearity.

3.7 Summary

In conclusion, in this chapter we discussed the coupled NLSEs for a combination of LP_{0m} modes of a parabolic index MMF, and used the analytical solutions to predict a *spatiotemporal* nonlinear effect that would result in time domain interference fringes. This type of phenomenon does not have an analog in SMF systems where all frequencies and polarizations reside in a single spatial mode.

We demonstrated broad qualitative agreement between numerical simulation results and experimental observations. At high input powers, the pulse profile emerging from the fiber was shown to vary depending upon the spatial location of sampling, and the number of time-domain

interference fringes was shown to increase at longer lengths of fiber.

Although this experimental study demonstrated the spatiotemporal nature of multimodal nonlinearity, even in the presence of a small number of modes, this version of the experiment also has many limitations. In Chapter 4, we discuss a similar phenomenon occurring in a step-index FMF – except that we are able to exercise much more control over the mode excitation, and also perform spatially resolved measurements with a much higher spatial resolution.

Chapter 4: Spatiotemporal Characterization of Nonlinear Intermodal Interference in a Step-Index FMF

4.1 Chapter Overview

In Chapter 3, we discussed the phenomenon of time domain fringes observed at the output of a multimode fiber that consists of nonlinearly interacting spatial modes. We also identified numerous shortcomings of our initial experiments, and in this chapter, we address these shortcomings and analyze the spatiotemporal measurements of multimodal nonlinearity that we reported in Reference [62].

In Section 4.2, we first discuss the problem of selectively and controllably exciting a small number of spatial modes. We present a unique technique that we developed that involves the direct etching of a phase mask onto the input end-face of a fiber using focused ion beam (FIB) milling. With this technique, we excite a combination of two spatial modes in a step-index FMF with a core diameter of $2a = 20$ μm. This fiber was chosen not only for its small number of spatial modes, but also because nonlinear optics in FMFs is expected to be of interest for mode division multiplexing (MDM) applications.

We then briefly revisit the coupled NLSEs before describing the spatiotemporal characterization tool that we have developed. In short, this technique consists of programmatically scan-

ning the output end-face of a FMF/MMF using a near-field scanning optical microscopy (NSOM) probe, and recording the time-domain waveform at each pixel. Using this data, we reconstruct the spatiotemporal nonlinear evolution of the pulse exiting the fiber.

4.2 Selective Mode Excitation

One of the shortcomings of our experiments reported in Chapter 3 was the lack of control over the modes excited in the fiber. Although tuning the spot size of the laser beam incident on the fiber's input end-face can tune the modal power distribution to some degree, the level of control that it gives is still quite minimal. For example, if we wanted to excite a mode combination of just two specific modes and not others, or if we wanted to excite just one higher order mode selectively, that is not impossible to do by simply adjusting the spot size of input Gaussian beam.

As mentioned above, for the work reported in this chapter, we use a step-index FMF with a core diameter $2a = 20$ μm. We discussed the spatial modes in this fiber, in the LP basis, in Fig. 2.3. The fiber supports 17 spatial modes per polarization at our laser wavelength of $\lambda_0 = 1064$ nm, out of which three are radially symmetric modes. For the phenomenon that we observe in this chapter too, we focus exclusively on the radially symmetric modes.

In Fig. 4.1(a), we show the numerically calculated coupling efficiencies to the three radially symmetric LP_{0m} modes as a function of the input beam radius for an axially aligned Gaussian illumination on the input end-face. As the plot shows, for any spot radius $< a$, where a is the core radius, it is not possible to excite a combination of two modes with roughly equal powers without also launching significant power in the third. It is also not possible to excite a higher order mode, say the LP_{03} mode, selectively.

Note: Although we use the LP mode notation to denote the radially symmetric modes that we describe in Chapters 3 and 4, we reiterate that for $l = 0$, the LP modes are completely equivalent to the hybrid modes denoted by HE and EH modes (see Table 2.1). It is only for $l \neq 0$ that, as we discussed in Chapter 2, the LP modes are not true propagation modes of the fiber. Our choice to use the LP_{0m} mode notation here, as opposed to the fully equivalent HE_{1m} notation, is purely for convenience and for denoting the fact that we work with linear polarized light throughout these experiments and analysis.

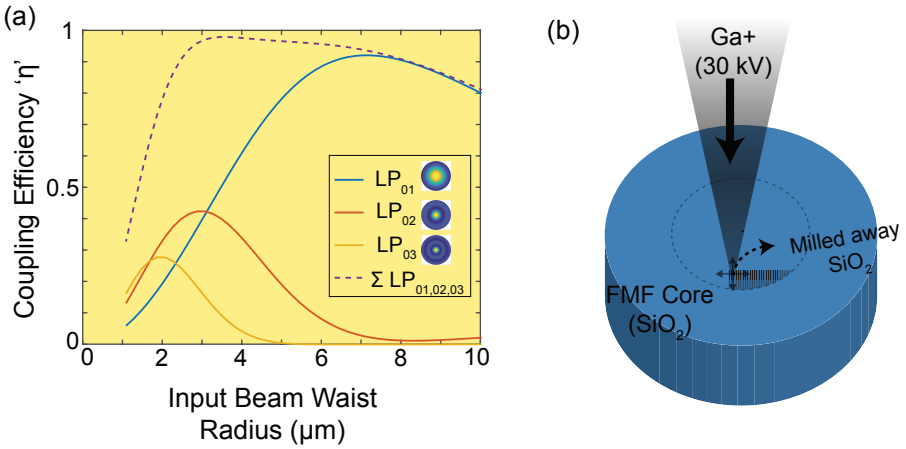

Figure 4.1: (a) Modal coupling efficiencies to the three LP_{0m} modes of the step-index FMF as a function of input Gaussian beam spot radius. (b) Illustration of direct phase mask etching using a focused beam of Ga^{+} ions (FIB milling).

In order to excite a desired mode combination selectively, several methods exist and have been reported in the literature. Phase-only spatial light modulators (SLMs) are by far the most commonly used devices for this purpose [20, 70]. However, the drawback of using SLMs lies in their bulky nature and their difficulty in alignment. Additionally, SLMs based on liquid crystals are prone to damage under high fluence illumination that is typical for nonlinear optical experiments. Free-space devices such as SLMs can also suffer from significant insertion losses, which

can be a hindrance for nonlinear optical experiments. For spatial modes that carry OAM, fork grating patterns, spiral phase plates and q-plates have been used [71, 72]. However, such methods typically suffer from high coupling losses, and are often not applicable for exciting linearly polarized Gaussian-like modes in a fiber.

The method that we employ in this work involves the direct etching of a phase mask onto the fiber input end-face. Our technique has been inspired by a thin-film deposition technique reported in Reference [73]. We differ from the method presented therein, however, in that we etch a phase mask directly onto the input end-face of the fiber, whereas the method suggested in Reference [73] consists of depositing a thin-film grating with film thickness and transparency appropriately chosen to achieve the desired transmissivity. There exist a variety of fabrication methods that can be used for patterning the end-face of a fiber, such as e-beam lithography, thin-film deposition, photolithography and nano-imprinting [74]. We adopt a focused ion beam (FIB) milling technique instead, as it is a convenient prototyping tool that allows for rapid fabrication of multiple samples, each with arbitrary numerically designed shapes.

Fig. 4.1(b) shows a schematic of the FIB milling process. The focused beam of accelerated (30kV) Ga^+ ions removes SiO_2 from the fiber's metal-coated (Au:Pd alloy) input end-face. The metal coating ensures that there is no charge accumulation on the fiber end-face, which can significantly impact the quality of the mill. The ion beam has a focused spot size of approximately 90 nm. The removal of SiO_2 imparts a phase difference between parts of the incoming near-field light beam that propagate through the milled portion and outside the milled portion. Appendix A provides further information on the fabrication process. For a simple disc-shaped mill pattern, the phase mask profile can be expressed as follows in terms of the mill depth d_m and mill radius r_m:

$$\Theta(r) = \begin{cases} (n_{co} - 1)\frac{\omega_0}{c} d_m, & \text{for } r \leq r_m \\ 0, & \text{for } r > r_m \end{cases} \tag{4.1}$$

Further discussion on the FIB fabrication process is provided in Appendix A. With this phase mask etched onto the fiber, the modal coupling efficiencies of the pth mode is given as:

$$\eta_p = \frac{\left| \int \Phi(r) e^{i\Theta(r,\phi)} \Psi_p(r,\phi) dA \right|^2}{\int |\Phi(r)|^2 dA \int |\Psi_p(r,\phi)|^2 dA} \tag{4.2}$$

where $\Phi(r)$ denotes the transverse electric field profile of the focused Gaussian laser beam, and $\Psi_p(r,\phi)$ denotes the modal profile of the pth spatial mode, and is given by Eq. 2.19. Fig. 4.2(a) shows a 3-dimensional graphic of a phase mask design $\Theta(r,\phi)$ that, when etched onto the fiber's input end-face, can excite the higher order LP_{03} mode of the fiber selectively. This is shown in the plot of modal coupling efficiencies calculated using Eq. 4.2, in Fig. 4.2(b). A comparison with Fig. 4.1(a) reveals that this was not possible without the use of a phase mask. We emphasize here that Eq. 4.2 for any arbitrary phase mask profile $\Theta(r,\phi)$, but we focus on a simple binary phase mask that is circularly symmetric so as to simplify the fabrication process.

Fig. 4.2(c) shows the phase mask of interest for the work presented in this chapter. As the modal coupling efficiency plot in Fig. 4.2(d) shows, for an input beam radius above 7 μm, it is possible to excite a combination of the LP_{01} and LP_{02} modes with comparable amplitudes, while excluding the LP_{03} mode. This, too, was not possible without the use of a phase mask as evidenced by the plot in Fig. 4.1(a). Although more complex phase mask designs might provide better overall efficiency and better extinction of the LP_{03} mode, for the purposes of this work, we adopted a simple phase mask design so as to ensure ease of repeatability. It is worth pointing out

that unlike other planar lithographic techniques that are inherently binary, the FIB technique does not constrain the masks to a piecewise uniform etch depth. In other words, the FIB technique is in principle capable of producing smooth variations in the mill pattern. However, binary patterns are easier to control and calibrate. For the remainder of this chapter, we adopt the phase mask shown in Fig. 4.2(c).

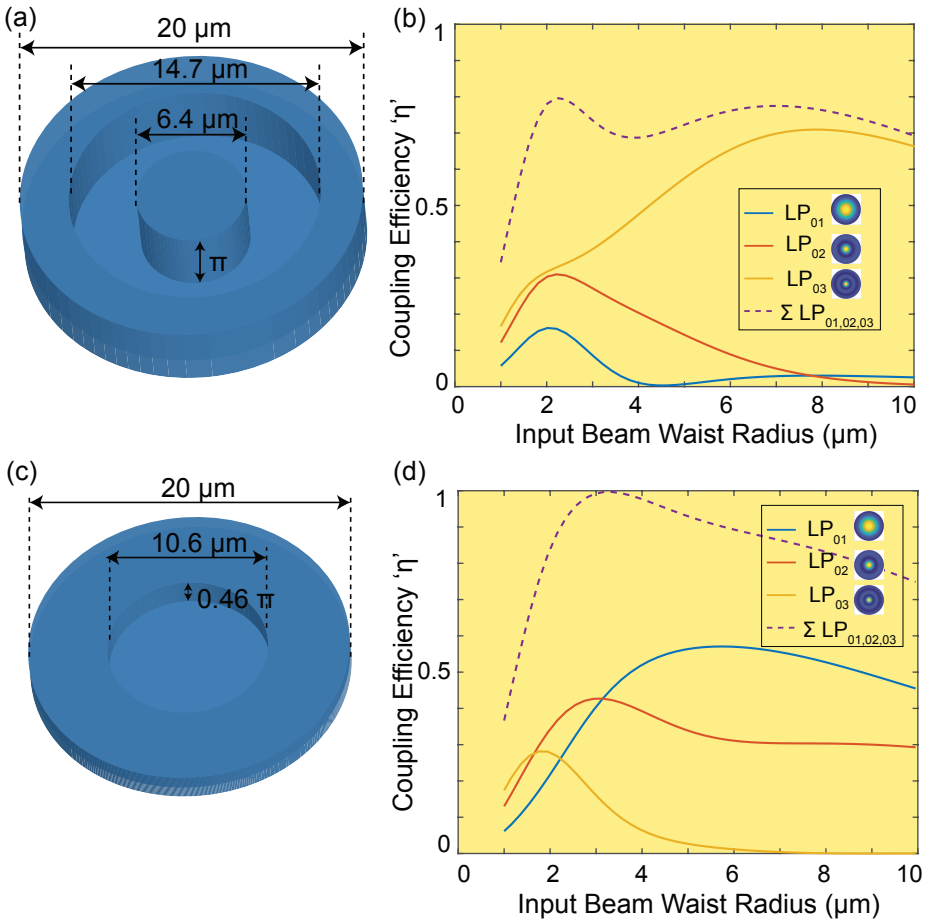

Figure 4.2: (a) 3-dimensional graphic representing the shape $\Theta(r)$ of an example FIB-milled phase mask design that can excite the LP_{03} mode selectively. The bounds of the graphic shown denote the core boundary of the FMF. (b) Modal coupling efficiency plot (calculated) resulting from the use of the phase mask described in part (a), showing coupling efficiency for the three LP_{0m} modes as a function of input Gaussian beam spot radius. (c) 3-dimensional graphic representing the shape $\Theta(r)$ of an FIB-milled phase mask design that can excite a combination of the LP_{01} and LP_{02} modes with comparable powers while ensuring no excitation of the LP_{03} mode. (d) Modal coupling efficiency plot (calculated) resulting from the use of the phase mask described in part (c), showing coupling efficiency for the three LP_{0m} modes as a function of input Gaussian beam spot radius.

4.3 Modeling Bimodal Nonlinear Propagation

The co-propagation of two LP_{0m} modes in the nonlinear regime in the FMF can be modeled using the coupled GMMNLSEs, as we did in Section 3.3. As before, it is helpful to make the following variable transformation:

$$A'_p(z,t) = A_p(z,t)e^{-i\beta_0^{(p)}z} \tag{4.3}$$

where $\beta_0^{(p)}$ represents the linear propagation constant of the pth spatial mode. The GMMNLSEs are then given as:

$$\partial_z A'_p = (-\delta\beta_1^{(p)}\partial_t - i\frac{\beta_2^{(p)}}{2}\partial_t^2)A'_p + i\frac{n_2\omega_0}{c}\mathscr{N}_{phkm}A'^{*}_h A'_k A'_m e^{i\Delta\beta_{phkm}} \tag{4.4}$$

Upon examining the various possible $\mathscr{N}_{phkm}$ and $\Delta\beta_{phkm}$ terms, we obtain the following simplified bimodal NLSEs:

$$\partial_z A'_1 = i\frac{n_2\omega_0}{c}(\mathscr{N}_{1111}|A'_1|^2 + 2\mathscr{N}_{1212}|A'_2|^2)A'_1 \tag{4.5a}$$

$$\partial_z A'_2 = i\frac{n_2\omega_0}{c}(\mathscr{N}_{2222}|A'_2|^2 + 2\mathscr{N}_{1212}|A'_1|^2)A'_2 \tag{4.5b}$$

where we neglect the $\beta_2^{(p)}$ and $\delta\beta_1^{(p)}$ terms as we work with long quasi-CW pulses, and the differential group delay between the two modes is much shorter than the pulse width used in our experiments. In other words, the dispersion length $T_0^2/|\beta_2^{(p)}$ is much longer than the fiber length L_f, and $\delta\beta_1^{(p)}L_f \ll T_0$, where T_0 is the temporal width of the pulse. Note, however, that we

neglect these terms only momentarily to develop an approximate analytical solution with which to help visualize the nonlinear phenomenon, and we retain these linear terms in our numerical simulations of the GMMNLSEs that we present in Section 4.5.

The analytical solutions to Eqs. 4.5 can be expressed as follows:

$$A_1'(z,t) = A_1'(0,t)e^{i\Gamma_1(t)z} \tag{4.6a}$$

$$A_2'(z,t) = A_2'(0,t)e^{i\Gamma_2(t)z} \tag{4.6b}$$

where we have defined $\Gamma_1(t)$ and $\Gamma_2(t)$ as:

$$\Gamma_1(t) = \frac{n_2\omega_0}{c}(\mathscr{N}_{1111}|A_1'|^2 + 2\mathscr{N}_{1212}|A_2'|^2) \tag{4.7a}$$

$$\Gamma_2(t) = \frac{n_2\omega_0}{c}(\mathscr{N}_{2222}|A_2'|^2 + 2\mathscr{N}_{1212}|A_1'|^2) \tag{4.7b}$$

Note that in writing Eqs. 4.7, we have utilized the fact that the modal powers remain constant. This because the remaining terms in the NLSEs Eqs. 4.5 are the (self and cross) phase modulation terms, as a result of which the derivative $\frac{d|A_p|^2}{dz} = 0$. The net intensity at the output of the fiber (i.e. $z = L_f$, where L_f denotes the fiber length) is then given by:

$$\begin{aligned} I(r,\phi,z=L_f,t) &= \frac{1}{2}n_{co}\varepsilon_0 c\,|\mathbf{E}(r,\phi,z=L_f,t)|^2 \\ &= \frac{1}{2}n_{co}\varepsilon_0 c\left|\sum_p \Psi_p(r,\phi)A_p(z=L_f,t)\right|^2 \end{aligned}$$

$$
\begin{aligned}
&= \frac{1}{2} n_{co} \varepsilon_0 c \left| \sum_p \Psi_p(r,\phi) A_p(z=0,t) e^{i\beta_0^{(p)} L_f} e^{i\Gamma_p(t) L_f} \right|^2 \\
&= \frac{1}{2} n_{co} \varepsilon_0 c \left| \sum_p \Psi_p(r,\phi) \sqrt{\eta_p} A_0(t) e^{i\beta_0^{(p)} L_f} e^{i\Gamma_p(t) L_f} \right|^2 \qquad (4.8)
\end{aligned}
$$

where η_p represents the fraction of input power coupled into the pth mode (shown in Figs. 4.2(c) and (d)), n_{co} is the core refractive index and $A_0(t)$ denotes the input pulse amplitude of the free-space beam.

In the linear regime where $\Gamma_p(t) = 0$, the right hand side of Eqs. 4.8 can be separated out into spatial and temporal parts by simply factoring out the $A_0(t)$. The shape of the spatial intensity pattern at the fiber output would then be independent of time, and the pulse shape at the output end-face of the fiber would not depend upon the spatial coordinate at which one samples the waveform.

In the nonlinear regime, however, this separation is no longer true. This is because each mode acquires a different $\Gamma_p(t)$, which in turn occurs because of differences in powers in the modes and differences in the nonlinear coefficients $\mathscr{N}_{1111}$, $\mathscr{N}_{2222}$ and $\mathscr{N}_{1212}$. Eqs. 4.8 can be further simplified as [62]:

$$
\begin{aligned}
I(r,\phi,z=L_f,t) &= \frac{1}{2} n_{co} \varepsilon_0 c |A_0(t)|^2 \left| \sum_p \Psi_p(r,\phi) \sqrt{\eta_p} e^{i\beta_0^{(p)} L_f} e^{i\Gamma_p(t) L_f} \right|^2 \\
&= \frac{1}{2} n_{co} \varepsilon_0 c |A_0(t)|^2 (\eta_1 \Psi_1^2 + \eta_2 \Psi_2^2 + 2\sqrt{\eta_1 \eta_2} \Psi_1 \Psi_2 \cos(\Delta\theta_{NL}(t))) \qquad (4.9)
\end{aligned}
$$

where $\Delta\theta_{NL}$ is given as:

$$\Delta\theta_{NL}(t) = \theta_0 + (\Gamma_1(t) - \Gamma_2(t))L_f \tag{4.10}$$

The phase offset θ_0 denotes the unknown relative linear phase between the two modes at the fiber output. For a perfect fiber where the propagation constants of the two modes and length of the fiber are accurately known, θ_0 is simply equal to $(\beta_0^{(1)} - \beta_0^{(2)})L_f$. However, in a real experiment, neither of these numbers can be easily ascertained with the required degree of precision (i.e. it is challenging to estimate L_f to within one beat length of the modes, which is less than $\sim$ 1 mm). Furthermore, θ_0 depends sensitively on the fiber length, the propagation constants of the modes as well as the relative phase with which the two modes are excited at the input. As a result, in order to be able to directly compare the results of Eq. 4.9 with experimental observations, we treat θ_0 as an unknown linear parameter that must be adjusted in the simulations in order to match the experimentally observed output intensity pattern at low input power.

Because of the time dependence of the input pulse shape $A_0(t)$, the nonlinear phases $\Gamma_p(t)$ – and consequently $\Delta\theta_{NL}(t)$ – depend on time. At high enough input powers, the peak nonlinear phase difference between the modes approaches π, which causes the instantaneous spatial interference pattern formed by the two spatially overlapping modes to appear different at the peak of the input pulse compared to that in the tails of the input pulse. Equivalently, the time-domain waveform at a given transverse spatial coordinate exhibits interference fringes. As we will see in subsequent sections, these predictions of the analytical model are validated by numerical simulations using the SSFM as well as experimental observations.

4.4 Experiments

In Section 4.2, we addressed one limitation of the initial experiments discussed in Chapter 3, relating to the ability to a desired mode combination. Another limitation of those experiments relates to the spatial scanning at the fiber output. Although we were able to resolve the time-domain output spatially, we did not have the capability to do so for the entire 2-dimensional output beam with a high spatial resolution. Here, we report a new technique that we have developed that is capable of this functionality.

For these experiments and for all experiments reported henceforth, we work with a Nd:YAG microchip laser [75] that outputs 720 ps (FWHM) pulses at a wavelength of $\lambda_0 = 1064$ nm and a repetition rate of 1 kHz. We use a plano-convex lens of focal length $f = 25.4$ mm to focus down the free-space Gaussian beam produced by the laser to a spot of radius $r_g = 8.4$ μm onto the input end-face of the patterned FMF. The length of the fiber used in this experiment is $L_f = 1.24$ m. The length has been kept short intentionally so as to minimize the impact of intermodal DGD, and also to minimize any depolarization or linear coupling into undesired spatial modes. The fiber was held in a roughly horizontal position across an optics workbench. The peak power of the pulse coupled into the fiber is estimated to be ≈ 15 kW.

In order to resolve the output beam spatially as well as temporally, we employ a near-field scanning optical microscopy (NSOM) probe that samples the output waveform evanescently. The NSOM probe comprised of a tapered single-mode fiber with a sub-wavelength aperture. The tapered section of the fiber was coated with metal so as to disallow coupling outside of the small coupling aperture at the tip of the probe. We use an NSOM instead of a lensed fiber as it provides superior spatial resolution that is not limited by diffraction. With commercially available NSOM

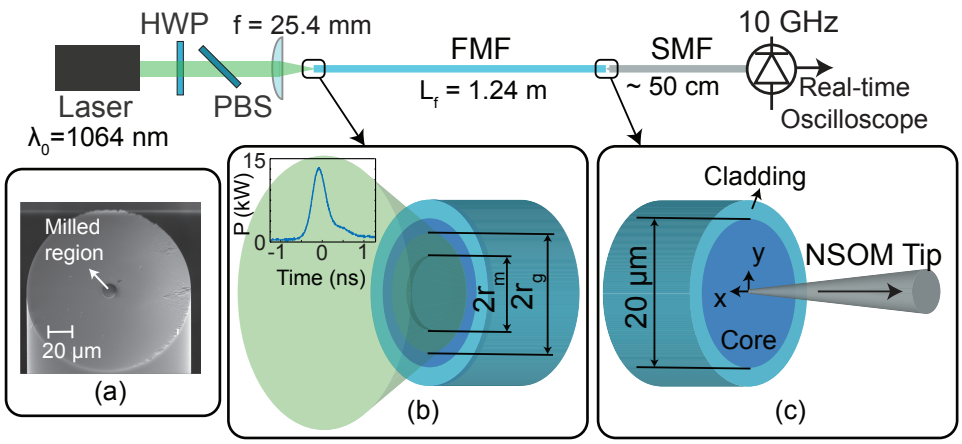

Figure 4.3: Experimental schematic for performing spatiotemporal measurements of multimodal nonlinearity in a step-index FMF. (a) Scanning electron microscopy (SEM) image showing the core + cladding of a $2a = 20$ μm step-index FMF. The dark disc-shaped region at the center is the milled phase mask region. (b) A free-space Gaussian beam is incident on the patterned FMF input end-face. Radius of the Gaussian beam is $r_g = 8.4$ μm. The inset plot shows the experimentally measured time-domain profile of the input optical pulse. (c) An NSOM tip is raster-scanned along the output end-face of the FMF, recording a time-trace at each "pixel". HWP = half wave plate, PBS = polarizing beam splitter.

probes, it is possible to achieve a spatial resolution of ~ 50 nm. For comparison, magnifying the beam before spatially resolving it (as was done in Reference [76], for example) would still be limited by the diffraction limit of the magnifying lens. Even for a lens of high numerical aperture, say $NA = 0.75$, the achievable diffraction-limited resolution is given by $\lambda/2NA \approx 710$ nm at our wavelength of interest, 1064 nm.

We observed in our experiments that the NSOM probes exhibit a polarization-dependence in their collection efficiency. In these experiments, however, this does not cause a problem for our work as we work with linearly polarized light. Care must be taken to characterize this polarization dependency beforehand, however, when working with vector beams and modes.

Light that is coupled into the NSOM probe is guided to a 10 GHz high-speed photoreceiver,

consisting of a transimpedance amplfier of gain 400 V/W, that is connected to a high bandwidth 33 GHz real-time oscilloscope. The time-domain waveform is measured at each "pixel" along a 2-dimensional grid of 20 μm $\times$ 20 μm that covers the entire core region of the FMF. We limited the spatial resolution for these measurements to 400 nm to allow for rapid raster scanning while also achieving a resolution that surpasses the diffraction limit. In order to minimize timing jitter in the time-domain measurements, the oscilloscope was triggered by a second electrical pulse waveform that was generated by sampling a part of the laser output and using another high-speed photodiode (not shown in Fig. 4.3). Finally, the time-domain waveforms recorded at each pixel were processed offline and stitched together to reconstruct the time-dependent nonlinear evolution of the output instantaneous intensity pattern.

4.5 Results and Discussion

4.5.1 Spatially-Resolved Time Domain Waveforms

We begin our discussion first by observing the time-domain interference fringes at different spatial locations. In Fig. 4.4, we show the experimentally measured time traces (in pink) alongside numerically simulated ones (in green), for two example spatial coordinates: $x = 0$ and $x = 4.4$ μm. Notice that the shape of the time-domain pulse measured at the output is different for the two spatial coordinates, just as we predicted using our analytical model. This is the same type of behavior that we saw in the experiments described in Chapter 3.

The on-axis pulse (both simulated and measured, shown in Fig. 4.4(a)) exhibits a local minimum at $t = 0$, which is when the peak intensity of the input pulse occurs. This is a direct result of the fact that for our experimental parameters, the peak nonlinear phase difference be-

tween the two overlapping modes is approximately π. At the tails of the input pulse, however, the nonlinear phase difference between the modes is much lower. This results in a time-domain output that exhibits a "minimum" at $t = 0$ when sampled along the fiber axis. At a different spatial location, such as the $x = 4.4$ μm plot shown in Fig. 4.4(b), the time-domain interference pattern exhibits a different shape. This is a result of the spatial variation of the modal amplitudes $\Psi_p(x, y)$ in Eqs. 4.9.

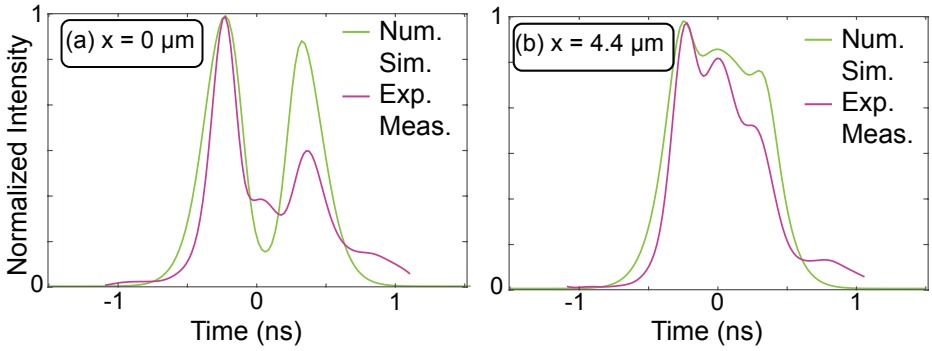

Figure 4.4: Spatially-resolved temporal measurements at the FMF output. Experimentally measured (pink) and numerically simulated (green) temporal pulse shape at two example spatial coordinates: (a) $x = 0$, and (b) $x = 4.4$ μm. Input pulse peak power ≈ 15 kW. (Data originally published in S.K. Dacha et al., Optica 7, 1796-1803 (2020) ©Optical Society of America)

The slight asymmetry observed in the numerical simulation results, shown in Fig. 4.4, arises from the fact that we have included the $\beta_1^{(p)}$ DGD terms in the coupled NLSEs when performing numerical simulations using the SSFM. The additional asymmetry observed in the experimental data arises from the asymmetry in the input pulse itself (shown in Fig. 4.3(b)), and likely also from experimental imperfections in the selective mode coupling described before.

Finally, we note the excellent agreement between simulation and experiment shown in Fig. 4.4. As mentioned before, θ_0 in Eq. 4.10 is treated as an unknown parameter. When

setting a value of θ_0 in order to compare simulated and experimental results, we do the following: we measure the output spatial pattern using a CMOS camera at low input power (i.e. in the absence of nonlinearity), and we tune θ_0 in our simulations to reproduce the same output intensity pattern (also in the linear regime, at low input power). It is worth reiterating that θ_0 is only a free parameter, and adjusting it in our simulations does not have any implications for the time-dependent dynamics observed. In other words, θ_0 only sets the "initial state" of the spatial beam at the tail of the pulse in the absence of any nonlinearity, and does not relate to any of the time-dependent dynamics that are observed thereafter.

4.5.2 Reconstruction of Spatiotemporal Nonlinear Evolution

As mentioned in the description of the experimental setup, the NSOM probe is raster-scanned across the output end-face of the FMF, and time-domain waveforms are recorded at each "pixel" with a spatial resolution of 400 nm. This data is then stitched together offline to reconstruct a time-dependent variation of the instantaneous 2-dimensional intensity pattern exiting the fiber. The temporal resolution achieved with this setup is approximately 100 ps, and is only limited by the bandwidth of the photodiode used in our experiment. The reconstructed patterns, in other words, would show us what one would see if we had a camera capable of sub ns sampling.

As Fig. 4.5 shows, the shape of the 2-dimensional intensity pattern at the output is Gaussian-like at both tails of the pulse, $t = -0.65$ ns and $t = 0.84$ ns. This denotes the intensity pattern formed by the interference of the two spatially overlapping modes that we have excited in the FMF. As the input pulse reaches its peak at $t = 0$, however, the nonlinear phase difference between modes reaches approximately one π, causing the modes to interfere with opposite phase as

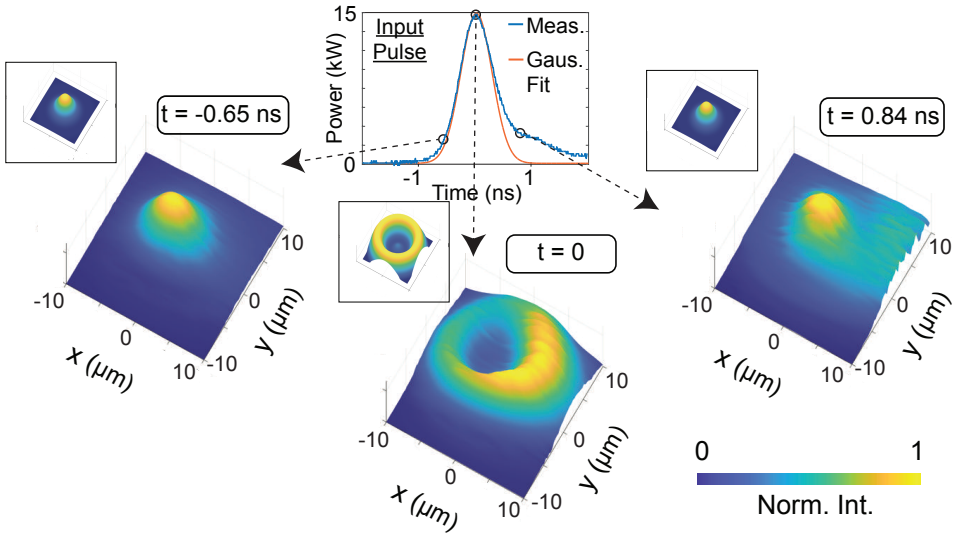

Figure 4.5: Spatiotemporal measurements of nonlinear interaction between the two spatial modes that we excited in the FMF. The instantaneous spatial intensity patterns were reconstructed by a synchronized stitching of the experimentally obtained spatially-resolved temporal measurements. The larger images at the different time instances ($t = -0.65$ ns, $t = 0$ and $t = 0.84$ ns) denote the experimentally obtained images, and the inset images show the results of numerical simulation of the coupled NLSEs. See Supplementary Videos 1 and 2 for movies of experimentally reconstructed and numerically simulated time-dependent spatial patterns. (Data originally published in S.K. Dacha et al., Optica 7, 1796-1803 (2020) ©Optical Society of America)

they did at the tails of the pulse, creating a donut-shaped beam. Once again, numerical simulation results reproduce experimental observations, as the inset images in Fig. 4.5 demonstrate.

Note: Several experimental measurements and numerical simulations reported throughout this thesis are accompanied by movies/video files that show time-dependent evolution of spatial waveforms. For the work described in this chapter, please see Supplementary Videos 1 and 2 for measured and simulated time-dependent variation of the spatial interference pattern caused by nonlinearly interacting LP_{01} and LP_{02} modes.

4.5.3 Thermo-Optic Interference Experiments

In order to further verify that the time-dependent effect that we observe in Fig. 4.5 results from a time-varying modal interference effect, we performed thermo-optic measurements that showed a temperature-dependent mode interference effect that caused similar spatial patterns to appear as in Fig. 4.5. First, the laser was attenuated to a power level where the nonlinear phase shift between the modes was expected to be very low (even at the peak of the input pulse). A short ($\approx$ 20 cm) section of the FMF was placed on a hot plate, and the temperature of the hot plate was slowly varied from 50^0 C to 150^0 C, and the output was imaged using a conventional CMOS camera.

As the temperature increases, the refractive index as well as the length of the $\approx$ 20 cm FMF section exhibit a temperature dependence. The thermal expansion is believed to be the dominant effect in this case based upon estimations of the index change caused by increasing the temperature of SiO_2. Or rather, it was found that the propagation constants of both the modes change roughly equally, which would not result in any significant change in the spatial interference pattern produced by the two modes. The thermal expansion of the fiber, however, does change the overall length of the fiber ever so slightly, as a function of temperature. In other words, tuning the temperature changes the phase with which the modes overlap at the output, thereby creating the variation in spatial patterns observed in Fig. 4.6.

Admittedly, these measurements are somewhat crude in many ways: i) the temperature reported in Fig. 4.6 is only the temperature of the hot plate, not necessarily that of the fiber's core material; ii) there may be a temperature gradient across the fiber cross section because the heating mechanism is not convectional (i.e. the side of the fiber touching the hot plate may be

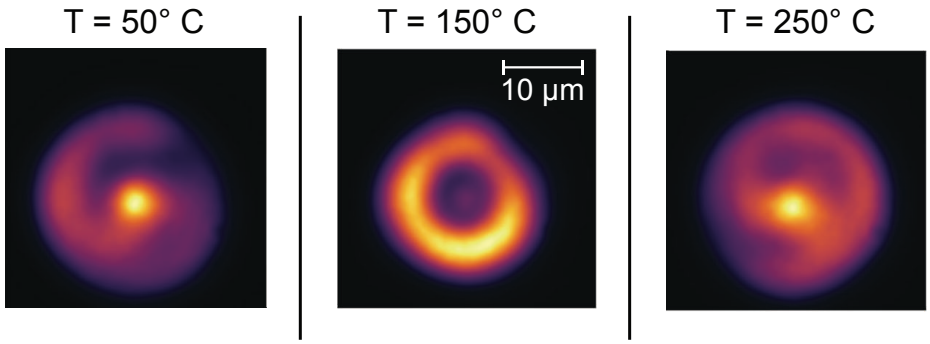

Figure 4.6: Temperature dependent interference patterns created by the two overlapping modes excited in the FMF. Each image was recorded using a conventional CMOS camera at a different hot plate temperature (50^0 C, 150^0 C and 250^0 C). (Data originally published in S.K. Dacha et al., Optica 7, 1796-1803 (2020) ©Optical Society of America)

hotter than the other side), although care was taken to flip the fiber around gently throughout the experiment; iii) increase in temperature of may introduce other perturbations that did not exist before because of thermal deformations.

However, the essential point of these measurements was simply to demonstrate the fact that changing the phase with which the two modes overlap can change the output intensity pattern. In fact, the images shown in Fig. 4.6 not only prove this statement, but they also show the same kind of spatial patterns observed in the spatiotemporal measurements Fig. 4.5. In other words, this demonstrates further that the time-dependent effect that we see in Fig. 4.5 is indeed a result of time-dependent nonlinear phase difference arising from SPM and XPM.

4.6 Summary

In this chapter, we described our work on modeling, simulating and experimentally measuring the nonlinear interactions (SPM and XPM) between two radially symmetric LP_{0m} modes

of a step-index FMF. We selectively excited the LP_{01} and LP_{02} modes using a novel phase mask etching technique that utilizes an accelerated and focused beam of Ga^{+} ions to mill SiO_2 out of the core of the FMF. This makes for a convenient phase mask prototyping technique that allows for the fabrication of very fine features on a fiber end-face.

At the output end, we demonstrated the capability of a powerful spatiotemporal characterization technique that we developed, wherein an NSOM probe scans the output end-face of the FMF and records a time-trace at various transverse spatial coordinates with a sub-wavelength (for our λ_0) spatial resolution of ≈ 400 nm. The temporal resolution obtained in our measurements is below 100 ps, and is only limited by the bandwidth of the photodiode used in our experiments. With commercially available technology, this technique can achieve temporal resolution of 10s of ps and a spatial resolution of well below 100 nm.

Finally, by synchronously stitching together the spatially-resolved temporal waveforms recorded, we were able to reconstruct the full time-dependent nonlinear evolution of the beam exiting the fiber [62]. In the next chapter, we will apply the same spatiotemporal scanning technique to study a different phenomenon in a parabolic GRIN fiber, namely Kerr-induced beam self-cleaning [15].

Chapter 5: Spatiotemporal Characterization of Kerr-induced Beam Self-Cleaning in a Parabolic GRIN MMF

5.1 Chapter Overview

The spatiotemporal characterization technique that we described in Chapter 3 can be utilized to measure any time-varying intensity pattern involving nanosecond pulses. In Chapter 1, we referenced a unique phenomenon that occurs in parabolic GRIN MMFs, namely Kerr-induced beam self-cleaning. The measurements reported in References [14] and [15] only used conventional spatial imaging that recorded the time-averaged output intensity pattern. The spatiotemporal characterization technique described in the previous chapter present an opportunity to better resolve this phenomenon.

Although at the time of our experiments it was broadly accepted that the beam self-cleaning phenomenon resulted from the "instantaneous" Kerr effect, and that it was not a result of the time averaging that a conventional "slow" camera would perform on the spatiotemporal beam exiting the fiber, there was no concrete experimental evidence demonstrating that the instantaneous beam of at the peak of the input pulse at $t = 0$ is self-cleaned while the beam at the tails of the pulses is not. This is the goal of the measurements presented in this chapter. Similar measurements were later reported by the same group that initially reported observation of the phenomenon, in

Reference [76].

A detailed study of Kerr-induced beam self-cleaning is beyond the scope of this thesis, as the main focus of our work has been the study of intermodal nonlinear effects between individual spatial modes. However, in this chapter, we describe the results of applying our spatiotemporal characterization technique to measuring the beam self-cleaning phenomenon. We begin by presenting a brief overview of the phenomenon, then describe our measurements before concluding the chapter.

5.2 Kerr-induced Beam Self-Cleaning

In Section 2.2.5, we discussed the spatial modes of a parabolic GRIN fiber and their properties. One of the unique features of the modes of a parabolic GRIN fiber is the grouping of modes of different l and m into mode groups of equal propagation constant that are also equally spaced from one another. This is illustrated in Fig. 2.4(a). In the nonlinear regime, this allows for energy exchange between various spatial modes via phase-matched four-wave mixing terms in the coupled NLSEs, as described in Section 2.3.2.3. As a result, in the presence of hundreds of spatial modes co-propagating in a parabolic GRIN fiber, a multitude of Kerr nonlinear interactions are possible, including phase modulation of a mode by hundreds of other modes, and the energy inflow and outflow out of modes from and to other modes.

In order to make sense of such complex phenomena, it is not sufficient to look at the interactions between individual modes alone, and it is essential to take a more "macroscopic" view. In Reference [15] (also see Reference [14]), one such complex phenomena was first reported wherein ~ 900 ps optical pulses at $\lambda_0 = 1064$ nm are propagated through 12 m of a $2a = 52.1$

μm parabolic GRIN fiber ($NA = 0.205$) in the nonlinear regime, and the evolution of the time-integrated spatial pattern was studied. The results of their measurements are shown in Fig. 5.1.

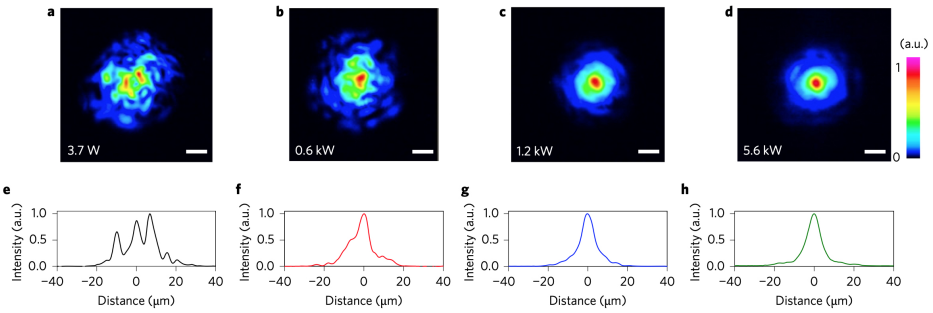

Figure 5.1: Experimental observation of Kerr-induced beam self-cleaning. (a)-(d) Near-field images of the output of the parabolic GRIN fiber ($\lambda_0 = 1064$ nm) for increasing input peak powers. Intensities in each image are normalized to the maximum in that image. Scale bars: 10 μm. (e)-(h) Beam profiles of horizontal cuts (through the center of the images) of images shown in (a)-(d). Fiber length used is 12 m. (Reprinted by permission from Nature Photonics: Krupa et al., Nat. Phot. 11, 237-241 (2017) © Nature)

The input free-space beam is coupled to the fiber so as to intentionally excite a large number of spatial modes. This is evidenced by the fact that at low input powers, the output of the fiber is observed to be a speckle pattern (see Fig. 5.1(a)). As the input power is increased, nonlinear interactions between the modes lead to an apparent "self organization" of the beam exiting the fiber, as the output beam looks like a cleaned up Gaussian beam. Notably, the authors report that spectral measurements reveal that the optical spectrum remains narrow, and most importantly, this phenomenon is observed below the Raman threshold. This indicates that this is purely a Kerr phenomenon and does not involve the dissipative Raman process. (Raman beam cleanup has also been studied previously in parabolic GRIN MMFs [67].)

This so-called self-cleaning phenomenon has attracted considerable curiosity and attention, both from a scientific research perspective but also for its potential applications for biomedical

imaging and high-power beam delivery. Numerous experiments have since reported similar phenomena in other types of fibers and at other wavelengths, including in the anomalous dispersion regime at $\lambda_0 = 1550$ nm. This phenomenon has only recently been explained using a semi-classical wave thermalization model [77]. In even more recent experiments, it has been demonstrated using a mode-resolved characterization method that the modal power distribution in the parabolic GRIN fiber approaches a Rayleigh-Jeans distribution, confirming the predictions of the thermalization model [32].

As mentioned before, a detailed study of this phenomenon is beyond the scope of this thesis. Instead, we focus on utilizing our spatiotemporal characterization technique to demonstrate that the Kerr-induced beam self-cleaning phenomenon is indeed an instantaneous phenomenon, and not an artifact of the time averaging of a conventional camera.

5.3 Spatiotemporal Measurements of Kerr-induced Beam Self-Cleaning

Fig. 5.2 shows the experimental schematic that we adopted for these measurements. We used ≈ 11 m of a $2a = 62.5$ μm parabolic GRIN fiber – the same kind used in measurements reported in Chapter 3. Unlike in the Chapter 3 experiments, however, we now use the $\lambda_0 = 1064$ nm Nd:YAG microchip laser that we used in Chapter 4. The laser produces 1 ns pulses that are coupled into the fiber using a plano convex lens. The input Gaussian beam is intentionally focused to an off-axis spot on the fiber's input end-face in order to excite a large number of modes propagating in the fiber.

For the length of the fiber that we used, we observed via a conventional CMOS camera the beam self-cleaning occurring for an input peak power of approximately 6 kW. At this stage, we

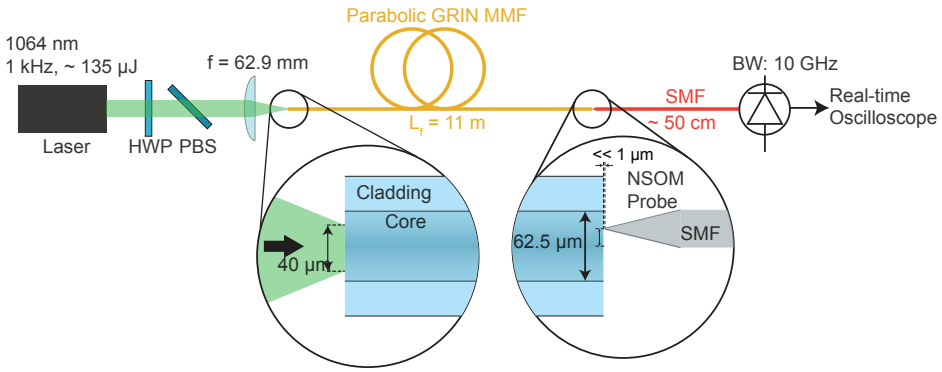

Figure 5.2: Experimental schematic for spatiotemporal measurement of Kerr-induced beam self-cleaning. The fiber used was a ~ 11 m long $2a = 62.5$ μm parabolic GRIN fiber. Peak power of the input pulse was ≈ 6 kW. HWP = half wave plate, PBS = polarizing beam splitter.

inserted the NSOM probe setup from Chapter 4 and performed raster-scanning along the cleaved output end-face of the parabolic index MMF. Because the piezo translation stage that we used for the raster-scanning only had a piezo travel range of 20 μm, our scan was limited to a 20 μm $\times$ 20 μm grid. Care was taken to ensure that the center of the beam exiting the fiber was present within the scanning window.

Fig. 5.3 shows the results of our measurements. At the tail of the pulse at $t = -0.85$ ns, the reconstructed intensity pattern looks like a speckle pattern, revealing the presence of several spatial modes, including many non-radially-symmetric ones. As the pulse approaches its peak at $t = 0$, the beam is now "cleaned up", visibly demonstrating a reduction of the instantaneous M^2 factor. In fact, the observed beam at $t = 0$ is cleaner than what is observed using conventional imaging methods such as those reported in References [14, 15] owing to the fact that we are observing the instantaneous beam at the peak of the pulse as opposed to the time-averaged intensity profile.

These measurements, as predicted, demonstrate the instantaneous nature of this phenomenon.

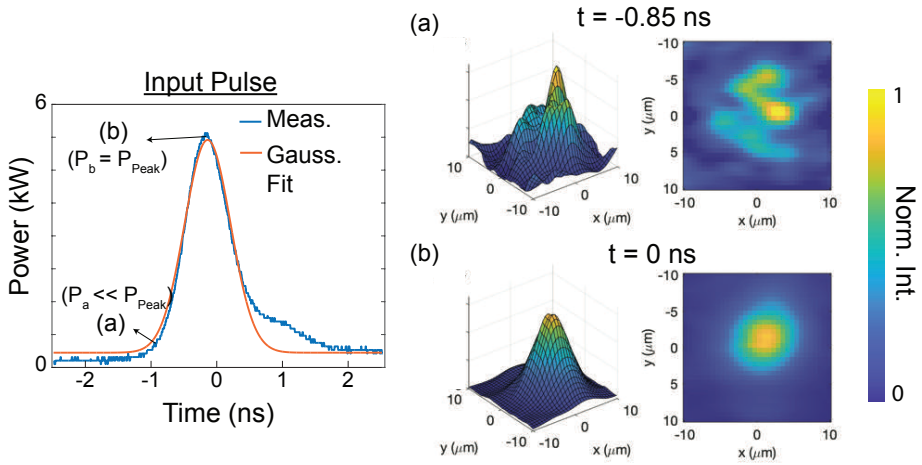

Figure 5.3: Spatiotemporal measurements of Kerr-induced beam self-cleaning. We show the reconstructed intensity pattern at (a) $t = -0.85$ ns (i.e. tail of the input pulse) and at (b) $t = 0$ (i.e. at the peak of the input pulse). The reconstructed intensity at the tail of the pulse shows a speckle pattern, indicating the presence of several spatial modes. At the peak of the pulse, we observe a cleaned up beam, experimentally demonstrating the instantaneous nature of this phenomenon.

As an alternate perspective on what these measurements indicate, one might also say that they further validate the spatiotemporal measurement technique if we begin with the assumption that the phenomenon is indeed instantaneous.

5.4 Summary

In summary, in this chapter, we have demonstrated the use of our spatiotemporal characterization technique to perform unique measurements of the Kerr-induced beam self-cleaning phenomenon. We discussed what the phenomenon entails, and some explanations that researchers have put forth in order to explain it. However, we do not dwell on analyzing the phenomenon or our measurements like we did in Chapters 3 and 4, as that is beyond the scope of this thesis. It is worth noting that similar time-resolved measurements of the phenomenon were reported in

Reference [76] around the same time as we performed our measurements. The authors in Reference [76] first magnify the output beam using a high numerical aperture lens before scanning the magnified beam using a conventional single mode fiber.

In the next chapter, we begin our discussion of nonlinear optical effects involving orbital angular momentum (OAM) fiber modes, which remains, at the time of this writing, a relatively under-studied topic.

Chapter 6: Nonlinear Rotation of Spin-Orbit Coupled States in a Hollow RCF

6.1 Chapter Overview

So far in this thesis, we have described our work with step-index and parabolic index fibers. The final type of fiber that we discuss is the hollow ring core fiber (RCF). As mentioned in Sections 2.2.2.2 and 2.2.6, the high cross-sectional index contrast of this type of fiber increases the effective index difference between the HE and EH modes for all azimuthal and radial mode orders l and m. This leads to the stable propagation of hybrid vector modes in RCFs. As we discussed in Sections 2.2.2.2 and 2.2.6, the hybrid vector modes can be superposed to give rise to the OAM mode basis, where each photon in a given spatial mode has a well-defined orbital angular momentum as well as spin angular momentum. While the high effective index split created by the index profile prevents the $SO_{a(a)}$ mode groups from mixing, mixing between modes within a degenerate $SO_{a(a)}$ group is prohibited by conservation of orbital angular momentum [50].

In this chapter, we discuss our work on nonlinear optical effects involving OAM fiber modes. More specifically, we describe a phenomenon that we observe when two degenerate spin-orbit anti-aligned modes co-propagate in the fiber. The coupled NLSEs describing the problem show great resemblance to those that are used for modeling the well-known nonlinear polarization rotation (NPR) phenomenon in SMFs. Using analytical calculations, numerical simulations, experimental measurements, we describe our discovery of the spin-orbit coupled generalization

of the NPR phenomenon.

6.2 Light Carrying OAM

Light that carries orbital angular momentum is described by a characteristic phase function $e^{iL\phi}$, where L is an integer and is known as the topological charge of the beam. The orbital angular momentum associated with each photon in such a beam is given by $L\hbar$ [37]. Light beams as well as fiber modes that carry OAM have received significant attention in a wide range of scientific research areas such as classical and quantum communication [78–84], optical metrology [85, 86], quantum optics [87–89], particle trapping and optical tweezers [90–92]. In fact, Arthur Ashkin received the Nobel Prize for Physics in 2018 for the invention of optical tweezers [93], as they have since proven to be a critical experimental tool for research in atomic and molecular physics and biophysics.

> *Note*: Thus far in this thesis, we have denoted the azimuthal mode number by l where $l = 0, 1, 2, ...$ However, as we saw in Section 2.2.2.2, the topological charge of an OAM beam is related to the $l \geq 0$ of the constituent HE and EH modes but can also be negative. As a result, we denote the topological charge of OAM beams throughout this thesis by capital L, which is allowed to be negative. With this notation, $L = \pm l$, or equivalently, $l = |L|$. The L is not to be confused with the notation for the length of the fiber, which we denote throughout this thesis by L_f.

The study of OAM light in the context of optical fibers has come to be of particular interest, owing in large part to the newly developed high confinement index geometries such as the hollow RCF discussed in Section 2.2.6. Technically, the mathematics of the OAM mode basis that we

discussed in Section 2.2.2.2 applies in any type of index geometry, and the OAM mode basis can, in principle, be used to describe light propagation in any circularly symmetric multimode fiber. However, in conventional optical fibers with step and parabolic index profiles, the effective index separation between the four possible modes for a given l and m would be nearly (but not exactly) zero. This results in strong coupling between the 4 HE and EH modes, and results in the formation of the maximally mixed LP mode basis described in Section 2.2.2.1. In fibers such as the hollow RCF, however, the high cross-sectional index contrast increases the effective index difference between the HE and EH modes, resulting in *stable* propagation of OAM modes that do not mix with each other in the linear regime, even in the presence of bends and perturbations [39].

In comparison to research that examines linear propagation of OAM modes in fibers, nonlinear propagation remains relatively understudied, and many questions remain unanswered. As is the theme of this thesis, nonlinear effects in RCFs, too, are of considerable interest from a telecommunications (SDM) as well as from a fundamental physics perspective. Some recent studies do exist, however, that study OAM propagation in the nonlinear regime. Recently, octave-wide supercontinuum generation was observed in the same hollow RCF as the one used in this work, where the entire supercontinuum resides in the same spatial mode [26]. The mechanism that allows for such a broad spectrum to reside in the same spatial mode despite the fact that the fiber supports multiple spatial modes has been attributed to the breaking of the near degeneracy between the spin-orbit aligned and anti-aligned modes, and to the high degree of selectivity of nonlinear products that results from the conservation of OAM [26, 63]. Parametric FWM has also recently been observed in the same type of fiber, demonstrating the possibility for generating OAM-carrying light pulses at user-defined wavelengths [63].

Here, we report a novel phenomenon that can be understood as a generalization of the well-known nonlinear polarization rotation effect occurring in SMFs.

6.2.1 Spin-Orbit Interaction

In this work, we use the same hollow RCF that was used in [26, 63]. As mentioned above and in Section 2.2.6, the index profile of this fiber was tailored to support stable propagation of OAM modes. In order to better understand how this comes about, consider the first order polarization correction term to the modal propagation constant Eq. 2.8. Although the high index contrast of the hollow RCF necessitates the use of a full vectorial mode solver, significant analytical insight can nonetheless be gained by studying the fiber using the tools of the weakly guiding approximation.

As we discussed in Section 2.2.2.2, the OAM mode basis is comprised of a complex superposition of the HE and EH modes. In any given fiber – including in the step and parabolic index fibers – the HE and EH modes have slightly different propagation constants. The magnitude of this difference depends upon the modal intensity profiles and the cross-sectional refractive index gradient via Eq. 2.8. The hollow RCF is therefore simply designed to increase this difference by way of tailoring the index profile to have a large gradient. Because the SO_a and SO_{aa} modes are combinations of the $even$ and odd HE and EH modes respectively according to Eqs. 2.14, an effective index split between the HE and EH modes is equivalent to an effective index split between the SO_a and SO_{aa} modes.

Looked at differently, the effective index difference between the SO_a and SO_{aa} modes can be understood by recognizing the fact that the "polarization correction" term in Eq. 2.8 depends

upon not just the spatial intensity shape, but also the polarization and phase of the electric field. In other words, for a mode that has a given polarization, the effective index depends upon its spatial phase – in other words the OAM. This is known as the spin-orbit coupling effect, where effective indices (equivalently, propagation constants) and group velocities of modes depend upon the OAM as well as the polarization – or more specifically, their relative alignment [40, 94, 95].

Reference [40] discusses the different regimes of spin-orbit interaction (SOI) as follows. In the scalar approximation, which is valid for conventional step- and parabolic-index fibers, all OAM modes of a given $|L|$ possess the same effective index. This is defined as the regime of negligible SOI. Fibers such as the one used in this work exhibit weak SOI, where modes with aligned and anti-aligned OAM and SAM possess different effective and group indices. The strong SOI case is described in Reference [40] as applicable for fiber index profiles that have a much thinner guiding ring index layer. In this regime, superpositions of free-space OAM and SAM beams with specific relative amplitudes and phases behave as individual modes. Such modes are defined by a given total angular momentum, and consist of a spatially-varying elliptical state of polarization. However, they are neither OAM nor SAM eigenstates and are not propagation-invariant modes in free space.

6.2.2 Spin-Orbit Coupled States

The term "spin-orbit coupled state" is defined as any general superposition of the "weak SOI" $\mathrm{SO}_{(a)a}$ fiber modes. Here, we specifically consider a superposition of the two degenerate $L = \pm 10$ SO_{aa} modes. Fig. 6.1(a) shows the intensity, polarization and spatial phase patterns of the two modes. The $L = \pm 10$ SO_{a} modes are not relevant for the work here, and are therefore not

shown, but Section 2.2.6 offers further discussion. Fig. 6.1(b) shows an unequal superposition of the two modes ($\alpha \neq 1$). Because the two modes have opposite helicities of polarization, an unequal superposition of them yields an elliptical state of polarization. However, since the modes also have opposite helicities of their spatial phase (OAM), the orientation of the resulting ellipse is spatially non-uniform. The ellipse orientation exhibits a periodicity with a period $2\pi/(2|L|) = 18^0$. As we will see in subsequent sections, a change in the relative phase between the two overlapping modes because of nonlinear SPM and XPM results in a power-dependent rotation of this pattern.

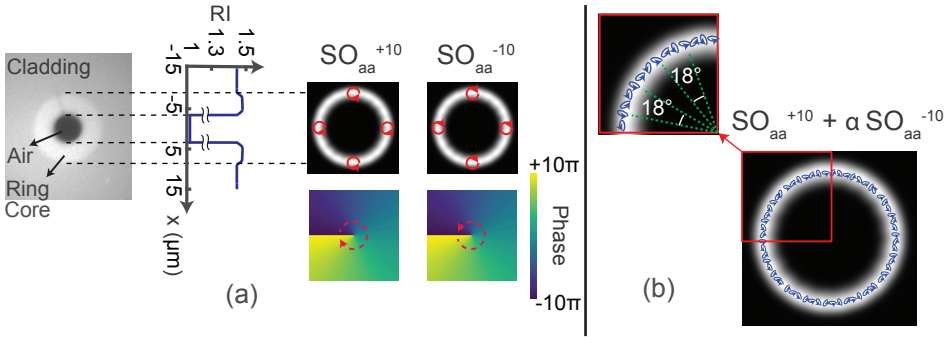

Figure 6.1: (a) $|L| = 10$ spin-orbit anti-aligned (SO_{aa}) modes of the hollow RCF used in this work. Each of the modes has a circular state of polarization that has opposite helicity as its phase (i.e. OAM). (b) 'Spin-orbit coupled state': An unequal superposition ($\alpha \neq 1$) of the two degenerate $|L| = 10$ SO_{aa} modes. This superposition consists of a spatially varying elliptical state of polarization. The ellipticity of the local ellipses remains the same, but the orientation of the ellipse exhibits a periodicity with period $2\pi/(2|L|) = 18^0$.

6.3 Coupled NLSEs for Nonlinear Rotation of Spin-Orbit Coupled States

6.3.1 Theory

In order to understand the nonlinear evolution of the spin-orbit coupled state described above, it is once again helpful to write down the coupled NLSEs. We begin by first writing down the NLSEs in the hybrid HE and EH mode basis, and then convert the NLSEs to the OAM mode basis using Eqs. 2.14. One can also write down the NLSEs directly in the OAM basis starting from Eqs. 2.60, but in this case, it is instructive to start in the hybrid mode basis for reasons that will become clear soon.

Because we work with the two SO_{aa} modes, which both comprise only of the EH modes that are completely degenerate with each other, the coupled NLSEs are given as [71]:

$$\frac{\partial B_1}{\partial z} = i\frac{n_2\omega_0}{c}\mathscr{N}_{1111}\left(|B_1|^2B_1 + \frac{2}{3}|B_2|^2B_1 + \frac{1}{3}B_2^2B_1^*\right) \tag{6.1a}$$

$$\frac{\partial B_2}{\partial z} = i\frac{n_2\omega_0}{c}\mathscr{N}_{1111}\left(|B_2|^2B_2 + \frac{2}{3}|B_1|^2B_2 + \frac{1}{3}B_1^2B_2^*\right) \tag{6.1b}$$

where we have denoted the slowly-varying pulse envelopes of the EH modes as $B_p(z,t)$. We now transform these equations into the OAM mode basis using the relations in Eqs. 2.14. The coupled NLSEs for the slowly-varying pulse envelopes in the OAM basis $A_p(z,t)$ are given as:

$$\frac{\partial A_1}{\partial z} = i\frac{2n_2\omega_0}{3c}\mathscr{N}_{1111}\left(|A_1|^2A_1 + 2|A_2|^2A_1\right) \tag{6.2a}$$

$$\frac{\partial A_2}{\partial z} = i\frac{2n_2\omega_0}{3c}\mathscr{N}_{1111}\left(|A_2|^2A_2 + 2|A_1|^2A_2\right) \tag{6.2b}$$

As the right hand side of Eqs. 6.2 shows, only the SPM and XPM terms survive upon performing the transformation to the OAM basis, while the equations in the hybrid mode basis Eqs. 6.1 also contain a phase-matched FWM term. This suggests that although phase-matched power exchange the two EH modes is possible, the power in each of the two SO_{aa} modes remains constant, and the two SO_{aa} modes interact nonlinearly via SPM and XPM alone.

The reader may already recognize that Eqs. 6.1 resemble the coupled NLSEs that describe nonlinearly interacting $\hat{\mathbf{x}}$ and $\hat{\mathbf{y}}$ polarization states in an isotropic single mode fiber, while Eqs. 6.2 also resemble the SMF case when written in the circular polarization basis. In SMFs, the equations in the circular polarization basis show that when the left and right circular states have *unequal* but non-zero power – i.e. when the net state of polarization is *elliptical* – they acquire a power-dependent nonlinear phase difference arising from SPM and XPM. This power-dependent phase difference leads to a power-dependence of the orientation of the net elliptical state of polarization. Equivalently, the instantaneous Stokes vector in the Poincaré sphere rotates about the S_3 axis by an angle that is proportional to the nonlinear phase difference between the left and right circularly polarized basis states. The degree of rotation about the S_3 axis depends upon the ellipticity of the propagating mode. This is the well-known nonlinear polarization rotation effect [11].

Here, we argue by analogy that a similar effect occurs. However, the presence of the additional spatial degree of freedom leads to this phenomenon having a spatial dimension as well. More specifically, we saw in Fig. 6.1(b) that an unequal superposition of the two modes leads to

a spatially non-uniform elliptical state of polarization, where the local ellipse orientation rotates along the azimuthal coordinate. The exact orientation of the overall pattern – or equivalently, the orientation of the ellipse at any given transverse coordinate – is determined by the phase with which the two modes overlap. In the presence of SPM and XPM, as described in Eqs. 6.2, the modes acquire a power-dependent phase difference. As a result, the entire polarization distribution exhibits a power-dependent rotation. Equivalently, the polarization ellipse at one fixed transverse spatial coordinate can be said to rotate about its axis in a power-dependent manner.

In SMFs, the NPR phenomenon involves purely polarization states. In this case, however, the polarization as well as spatial phases of the modes – as well as the coupling between them – are key to making this phenomenon possible. In other words, this is a spin-orbit coupled generalization of NPR.

6.3.2 Numerical Simulations

We numerically simulate this phenomenon by solving the coupled NLSEs in Eqs. 6.2 using the SSFM. As mentioned in Section 2.2.6, the modes are computed using a vector finite-difference mode solver from Reference [53]. The results of these simulations are shown in Supplementary Video 3 attached with this thesis (also accessible under 'Supplementary Material' in Reference [71]), snapshots of which are shown in Fig. 6.2. As the results presented in Supplementary Video 3 show, the instantaneous orientation of the polarization pattern varies with time as a result of SPM and XPM between the two interacting modes.

Because of the added spatial degree of freedom, this phenomenon can be easily observed by imaging the output beam through a linear polarizer. For example, imaging the beam shown

in Fig. 6.1(b) through a linear polarizer results in the appearance of $2|L| = 20$ lobes in the imaged intensity pattern. The orientation of this lobe pattern depends upon the phase with which the two modes overlap. The power-dependent rotation effect described above, therefore, results in a power-dependent rotation of the lobe intensity pattern, as shown on the right hand side of Supplementary Video 3 and Fig. 6.2. The rotation of the intensity pattern is much easier to observe experimentally than the rotation of a spatially-varying state of polarization.

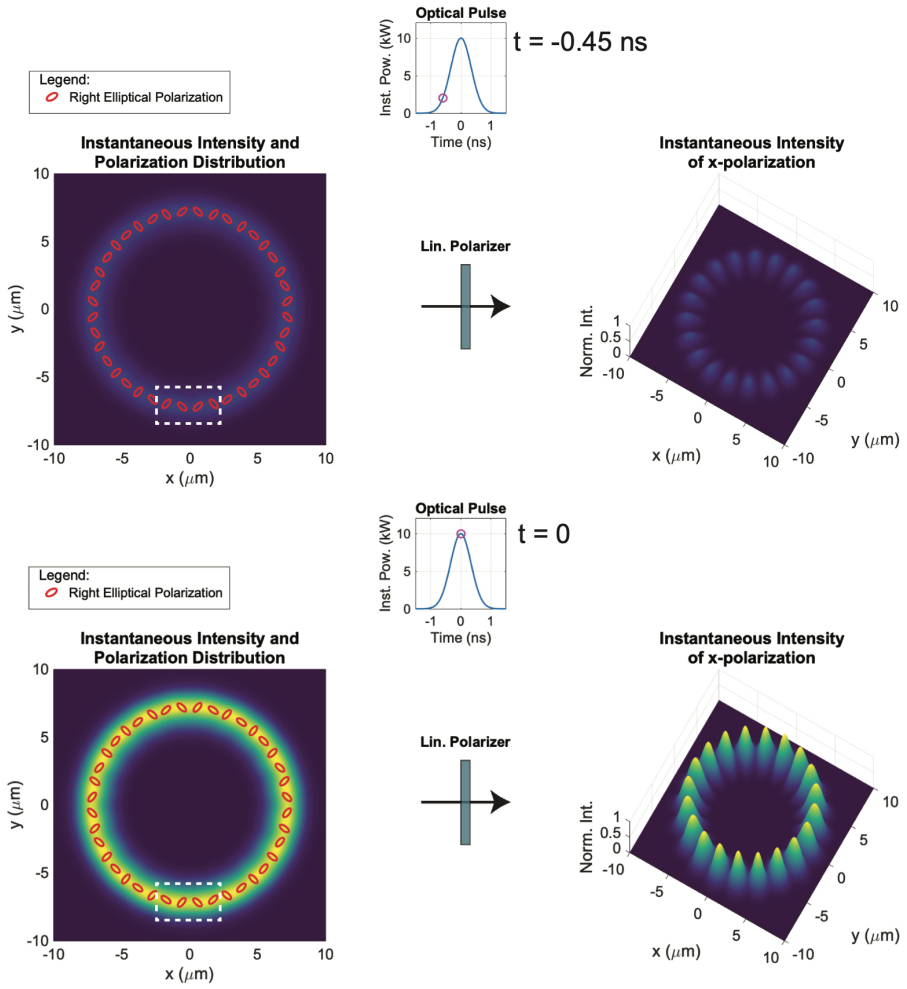

Figure 6.2: Snapshots of Supplementary Video 3, which shows numerical simulation of nonlinear rotation of our mode superposition. (Top) Instantaneous distribution of polarization and instantaneous lobe pattern along the rising edge of the input pulse, at $t = -0.45$ ns. (Bottom) At the peak of the input pulse $t = 0$, the instantaneous polarization distribution, as well as the lobe intensity pattern, can be observed to be rotated relative to that at $t = -45$ ns. This is seen by observing, for example, the ellipses within the dashed white box at $t = -0.45$ ns and $t = 0$. (Data originally published in S.K. Dacha et al., Opt. Exp. Vol. 30, No. 11, 18481-18495 (2022) ©Optical Society of America)

In fact, the experimental setup required to observe this effect can be simplified further by imaging the output of the fiber using a conventional "slow" CCD/CMOS camera. The rotation experienced by the lobe pattern for a given peak power can be ascertained by simply measuring

the rotation of the lobes seen in the time-averaged image. At higher input powers, the lobes undergo significant rotation within the duration one one pulse, resulting in a "smearing out" of the time-averaged lobe images. However, the rotation at the peak of the input pulse is still evident from the time-averaged image via the position of bright lobes over a smeared out background. Simulations of this behavior are shown in Supplementary Video 4.

In the following sections, we describe our experimental results wherein we demonstrate a power-dependent rotation of the time-averaged lobe intensity pattern.

6.4 Generation of OAM Beams

Several methods exist for generating light beams that contain well-defined OAM. The mechanism underlying the generation of OAM varies from one method to another. For example, spiral phase plates [96], forked gratings [97] and mode converters [98] all consist of elements that contain a phase discontinuity. These techniques are polarization insensitive, meaning that the generated beams can have any state of polarization, but have a uniform polarization across the beam.

Other methods such as q-plates [99], J-plates [100] and p-plates [101] all couple the beam's OAM with its polarization. Such methods are typically based on the Pancharatnam-Berry (PB) geometric phase. Because we are interested in generating a combination of the two $L = \pm 10$ SO_{aa} modes, we employ a q-plate of appropriate q value in this work. Fig. 6.3 summarizes the functionality of a q-plate.

Liquid crystal (LC) technology is most commonly used for fabricating q-plates. In this work, we employ a custom fabricated transmissive dielectric metasurface q-plate. Metasurface

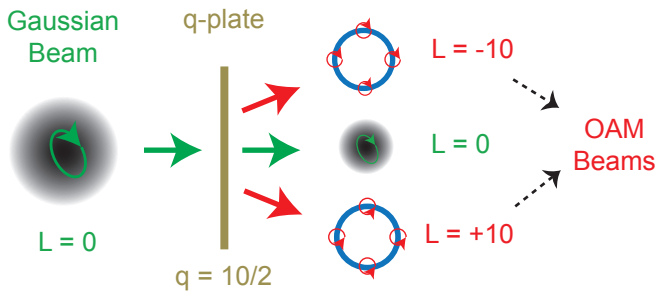

Figure 6.3: Schematic summarizing the functionality of a q-plate. For an input Gaussian beam with an elliptical state of polarization, the output of a q-plate of $q = |L|/2$ consists of a combination of two $|L| = 10$ SO_{aa} OAM beams, along with an unconverted Gaussian component. The conversion efficiency of a q-plate is often defined as the ratio of output power in OAM beams to the total input power.

devices offer the capability to structure a light beam on the sub-wavelength scale, and they allow for simultaneous control of polarization as well as phase. They also have higher damage thresholds compared to conventional LC devices, which makes them ideal for use in nonlinear optical experiments.

6.5 Experiments

The metasurface q-plate used in our experiments was fabricated by our collaborators at NIST. The metasurface consists of high aspect-ratio amorphous silicon nanofins laid out on a 2-dimensional Cartesian grid [102]. Fig. 6.4(a) shows an illustration of the "unit cells" that span the device. The spacing between adjacent unit cells is ≈ 400 nm. Each nanofin is approximately 272 nm long, 104 nm wide and 760 nm tall, and each acts as a half-wave plate for a laser beam at wavelength $\lambda_0 = 1064$ nm. The q-plate functionality is achieved via a rotation of the nanofin fast axis orientation along the azimuthal coordinates of the grid. The fast axis orientation of a nanofin is given by $\Theta_{NF} = |L|\phi/2$, where ϕ is the azimuthal coordinate with respect to the center of the

2-dimensional pattern, as shown in Fig. 6.4(b). We have provided a detailed recipe for fabrication in Reference [71].

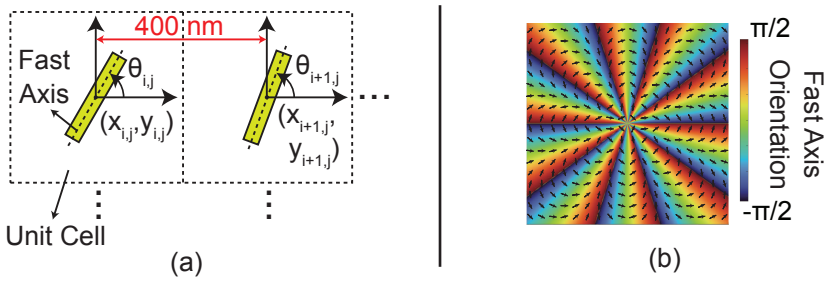

Figure 6.4: Description of metasurface q-plate with $q = |L|/2 = 10/2$. (a) Schematic illustrating a unit cell consisting of a 272 nm $\times$ 104 nm $\times$ 760 nm amorphous Silicon nanofin. Spacing between adjacent unit cells is $\approx$ 400 nm. (b) The q-plate profile showing the spatial variation of the fast axis orientation. The orientation of a nanofin at an azimuthal coordinate ϕ is given by $\theta_{NF} = |L|\phi/2$.

Fig. 6.5 shows a schematic of our setup for these experiments. We use the same laser as we described in Chapters 4, 5 that outputs $\approx$ 720 ps (FWHM) Gaussian-shaped optical pulses at $\lambda_0 = 1064$ nm. The power control optics remain the same as well, consisting of a half-wave plate and a polarizing beam splitter (PBS). The fabricated transmissive metasurface q-plate is inserted before the input end-face of a $L_f \approx 1$ m long section of hollow RCF. A free-space quarter wave plate (QWP) is used to tune the state of polarization of the Gaussian beam that is incident on the q-plate. The output consists of a combination of the $|L| = 10$ SO_{aa} modes as illustrated in Fig. 6.3. The q-plate that we fabricated was measured to have a conversion efficiency of $\approx$ 20 %. The unconverted $L = 0$ part of the beam was prevented from coupling into the fiber by choosing the focal length of the aspheric lens used in the experiment to focus the $|L| = 10$ beams into the guiding core layer while focusing the Gaussian component into the air section at the center [103]. This is confirmed by the linear characterization measurements reported below. In sum, this setup

offers the capability to tunably excite a combination of the two $|L| = 10$ SO_{aa} modes in the RCF. The relative power is conveniently adjusted using the free-space QWP.

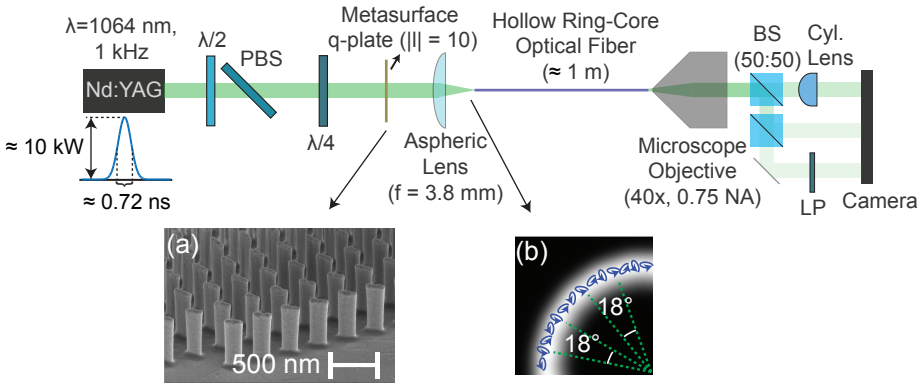

Figure 6.5: Schematic of experimental setup used for observing nonlinear rotation of spin-orbit coupled states. Inset (a) shows a scanning electron micrograph of part of the fabricated metasurface q-plate. Inset (b) shows the beam entering the fiber for excitation of the two SO_{aa} modes, consisting of a spatially-varying state of elliptical state of polarization. At the output end, the beam exiting the RCF is imaged using polarization and OAM-resolving optics. PBS = polarizing beam splitter, $\lambda/2(4)$ = half (quarter) wave plate, LP = linear polarizer.

The output of the fiber is characterized to measure the OAM as well as polarization content using free-space optics. The beam is first magnified using an infinity-corrected microscope objective with a numerical aperture of 0.75 and magnification 40x. A cylindrical lens converts a portion of the magnified beam from a Laguerre-Gaussian (LG) beam to a Hermite-Gauss (HG) beam. Counting the number of dark fringes in the resulting HG beams reveals the $|L|$ value of the output beam [98]. A linear polarizer is employed to observe the $\hat{\mathbf{x}}$ polarized part of the output beam.

The spatiotemporal measurement technique used in Chapters 4 and 5 is not ideal for the measurements discussed here, as the near-field scanning method does not allow for sufficient space to insert a linear polarizer – and observing the output beam through a linear polarizer is of

key importance for these experiments. As we discussed in Section 6.3.2, time-averaged methods such as conventional CCD/CMOS cameras prove sufficient for observing the phenomenon of interest here.

6.6 Demonstration of Tunable Excitation of SO_{aa} Modes

We begin our analysis of experimental observations by first demonstrating the tunability of excitation afforded by the metasurface q-plate. As mentioned above, the ratio of powers in the two SO_{aa} modes is adjusted using the QWP shown in Fig. 6.5. In Fig. 6.6, we show experimentally measured images (originally published in Reference [71]) at low input power, in the absence of any optical nonlinearity. The QWP setting is tuned such that the state of polarization of the Gaussian laser beam incident on the q-plate varies from left circular to right circular. For each case, we show images of the overall intensity pattern, the $\hat{\mathbf{x}}$ polarized intensity, and the corresponding HG mode pattern observed when the output beam is imaged through a linear polarizer.

For a circularly polarized Gaussian beam incident on the q-plate, the free-space output consists of a combination of a pure OAM beam alongside the remnant unconverted portion of the Gaussian beam. The latter is not guided through the fiber, as we described above, and the output of the fiber shows a clean $L = +10$ SO_{aa} mode. This is seen by counting the number of dark fringes in the cylindrical lens measurement corresponding to this case shown in Fig. 6.6. The absence of the unconverted Gaussian portion is evident by further observing that the image does not show a bright region at the center of the image, which would be observed if significant power from the unconverted beam coupled into the fiber.

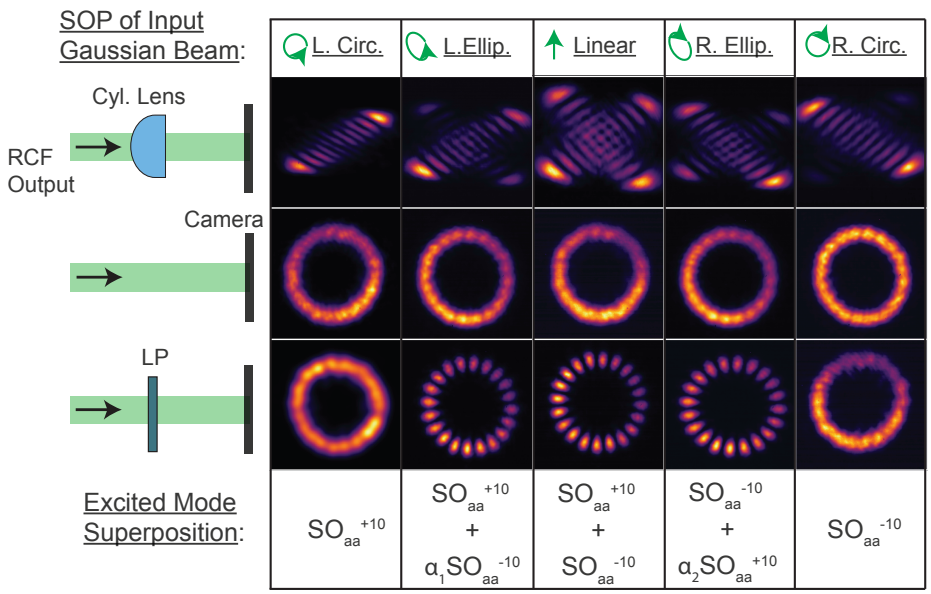

Figure 6.6: Tunable excitation of the two $|L| = 10$ SO_{aa} modes in the RCF. The output images are shown for input states of polarizations of the Gaussian laser beam being left circular, left elliptical, linear, right elliptical and right circular. For each case, we show: (Top) image of the HG mode pattern indicating the OAM content, (Middle) image of the overall intensity pattern, and (Bottom) image of the $\hat{\mathbf{x}}$ polarized intensity pattern. All images shown are experimentally measured. We also denote the mode superposition achieved for each case. $\alpha_{1(2)} < 1$. (Data originally published in S.K. Dacha et al., Opt. Exp. Vol. 30, No. 11, 18481-18495 (2022) ©Optical Society of America)

Similarly, for the right circularly polarized case, we see that the output consists of a pure $L = -10$ SO_{aa} mode, except with the orientation of the resulting HG pattern being opposite that of the $L = +10$. In both of these cases, both the overall intensity profile as well as the $\hat{\mathbf{x}}$ polarized intensity show full rings without the appearance of any lobes. This is fully consistent with numerically calculated mode profiles.

For elliptically and linearly polarized inputs, we see in Fig. 6.6 that the output consists of a combination of the two SO_{aa} modes. This results in the appearance of $2|L| = 20$ lobes in the $\hat{\mathbf{x}}$ polarized intensity patterns while not showing any lobes in the full intensity pattern. This is,

once again, consistent with the calculated mode superposition profiles. These measurements thus demonstrate tunable excitation of the two SO_{aa} modes.

In order to observe the nonlinear rotation effect described above, we are interested in exciting an unequal combination of the two modes. In the measurements that we discuss below, the QWP is set to positions that allow for this unequal excitation

6.7 Demonstration of Nonlinear Rotation of Spin-Orbit Coupled States

We study two main cases here, one corresponding to the case of a dominant $L = -10$ mode, where the power ratio between the two modes is $P_{V+}/P_{V-} \approx 0.15$, and another case with a dominant $L = +10$ mode with $P_{V+}/P_{V-} \approx 5.88$. In Fig. 6.7, we show numerically simulated and experimentally obtained time-averaged images for both of these cases, at three different peak powers of the pulse propagating in the fiber. A rotational wheel grid has been overlaid on top of all images for aid in visualizing the rotation.

The images shown in Fig. 6.7 clearly demonstrate the nonlinear rotation that we predicted in Section 6.3.2. For the dominant $L = -10$ case, for example, both simulated and measured images show a counter-clockwise rotation. In the dominant $L = +10$ case, meanwhile, the images show a clockwise rotation. This is in agreement with both theory as well as intuition, as the sense of rotation is determined by whether the nonlinear phase difference between the modes $\Delta\Theta_{NL} = \Theta_{NL,+10} - \Theta_{NL,-10}$, where $\Theta_{NL,\pm 10}$ denotes the nonlinear phase of the $L = \pm 10$ mode, is a growing positive number or a falling negative number as the power is increased.

In both cases, the lobe pattern diminishes in contrast as the power is increased. This is a result of the fact that at higher powers, significant time-dependent rotation of the lobe pattern

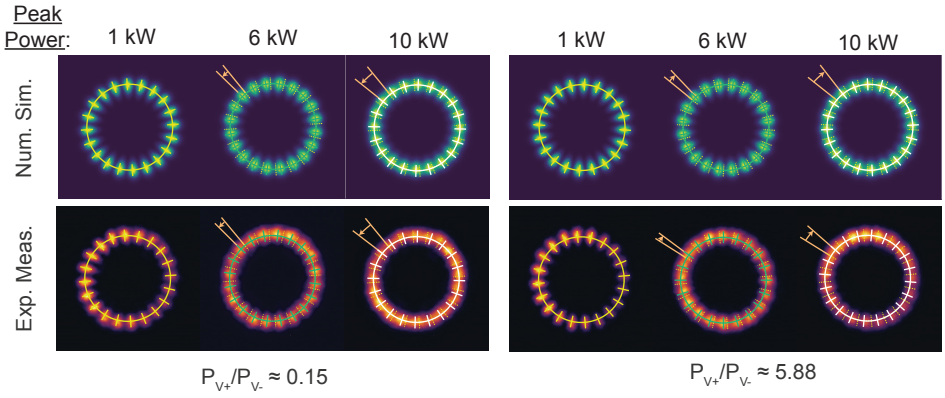

Figure 6.7: Demonstration of nonlinear rotation of an unequal combination of the two $|L| = 10$ SO_{aa} modes in the RCF. (Top row) Numerically simulated time-averaged images of the beam emerging from the fiber as imaged through a linear polarizer. (Bottom row) Experimentally obtained time-averaged images of the fiber output imaged through a linear polarizer. Images in both rows are shown for increasing peak powers, and for two different cases: for the dominant $L = -10$ case and the dominant $L = +10$ case. A rotational wheel grid with a uniform angular spacing of $2\pi/(2|L|)$ is overlaid on all images to aid in visual interpretation of observed rotation. The arrows indicate the direction and amount of rotation observed. For experimentally obtained images, the rotational wheel grid is aligned with the lobes using the image processing technique described below to avoid human error with noisy images. (Data originally published in S.K. Dacha et al., Opt. Exp. Vol. 30, No. 11, 18481-18495 (2022) ©Optical Society of America)

occurs within the duration of a single pulse. When time-averaged, this results in the smearing out. This is analogous to the apparent "depolarization" observed when studying the NPR phenomenon in SMFs using short optical pulses that are averaged over in time when using slower polarization characterization equipment.

These results are much more visually obvious and appreciable when viewed as a movie. Supplementary Video 4 shows numerical simulation results, and Supplementary Videos 5 and 6 show experimental results shown in Fig. 6.7. (Supplementary Videos are also accessible under 'Supplementary Material' in Reference [71].)

6.8 Image Processing

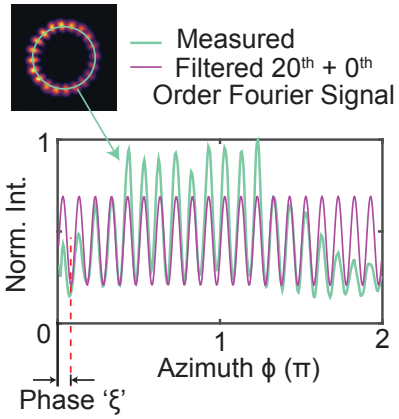

Figure 6.8: Summary of the image processing technique employed to measure the power-dependent rotation and smearing out of experimentally obtained time-averaged lobe patterns. Rotation is measured as a change in the Fourier phase ξ of the filtered signal, while smearing out is quantified as the ratio of amplitudes of the 0^{th} and $\pm 20^{\text{th}}$ Fourier components. (Data originally published in S.K. Dacha et al., Opt. Exp. Vol. 30, No. 11, 18481-18495 (2022) ©Optical Society of America)

In order to better make sense of the rotation observed in Fig. 6.7, and in order to avoid the element of human error, we employ an image processing technique that is summarized in Fig. 6.8. A concentric ring of an appropriate radius is overlaid on top of the measured time-averaged lobe pattern, and the intensity along the ring is extracted. After performing Fourier filtering, we retain only the 0^{th} and $\pm 20^{\text{th}}$ components. The $\pm 20^{\text{th}}$ components are chosen because we are looking for patterns that correspond to the $2|L| = 20$ lobes. The filtered signal is denoted in pink, while the original signal is denoted in green in Fig. 6.8. The close match of the two curves show that most of the essential information of the signal is retained by this procedure while noise is filtered out. The rotation of the lobe pattern δ is then measured as a change in the Fourier phase

ξ. The two are related as:

$$\delta = 18^{\circ}\xi/(2\pi) \tag{6.3}$$

The smearing out of the time-averaged lobe patterns is quantified by defining the 'lobe contrast' as the ratio between the amplitudes of the 0^{th} and $\pm 20^{\text{th}}$ Fourier components.

Fig. 6.9(a) shows the measured and simulated rotations of the time-averaged images upon use of the image processing algorithm described above. Firstly, the plot shows that the dominant $L = \pm 10$ cases exhibit opposite senses of rotation, as we discussed above already. Secondly, even for the dominant $L = -10$ case, we repeated the measurement for two different values of modal power ratio, namely $P_{V+}/P_{V-} \approx 0.15$ and $P_{V+}/P_{V-} \approx 0.32$. While the direction of rotation is the same in these two cases, Fig. 6.9(a) shows that the magnitude of rotation is different. This is consistent with the analytical expectation that the amount of rotation depends upon the modal power ratio. Finally, we observe from the red plot in Fig. 6.9(a) that for the control case of approximately equal power in the two modes, we observe minimal rotation.

Figs. 6.9(b) and 6.9(c) show simulated and measured lobe contrast, respectively, as a function of power. In all cases except for the control cases of input circular polarization (that excites only a pure SO_{aa} mode) and input linear polarization (that excites an equal combination of the two SO_{aa} modes), the simulated as well as measured images exhibit significant reduction in the mode contrast. In other words, they demonstrate smearing out of the lobe patterns at higher input powers as a result of time-averaging. For the control case corresponding to equal power in the two modes, there is little rotation observed, as a result of the fact that equal powers in the two SO_{aa} modes is equivalent to exciting one pure EH mode. For the control case corresponding to

a single OAM mode excited, lobes do not appear even when imaged through a linear polarizer, as explained in Fig. 6.6. As a result, the lobe contrast remains close to 0.

Finally, we note the sources of noise in the images described and analyzed here. These include alignment imperfections at the input coupling as well as at the output imaging ends, fabrication defects in the fiber and in metasurface q-plate, non-uniformity in input illumination as well as errors arising from the image processing algorithms. In order to ensure that the findings presented here are reliable, an error analysis was performed. The error bars displayed in Fig. 6.9 correspond to one standard deviation of observed pattern rotation and lobe contrast value, which was based upon collecting multiple time-averaged images for each data point and estimating the deviation of these quantities. Despite these sources of error, however, we note the excellent agreement between simulations and experimental observations in Figs. 6.7 and 6.9.

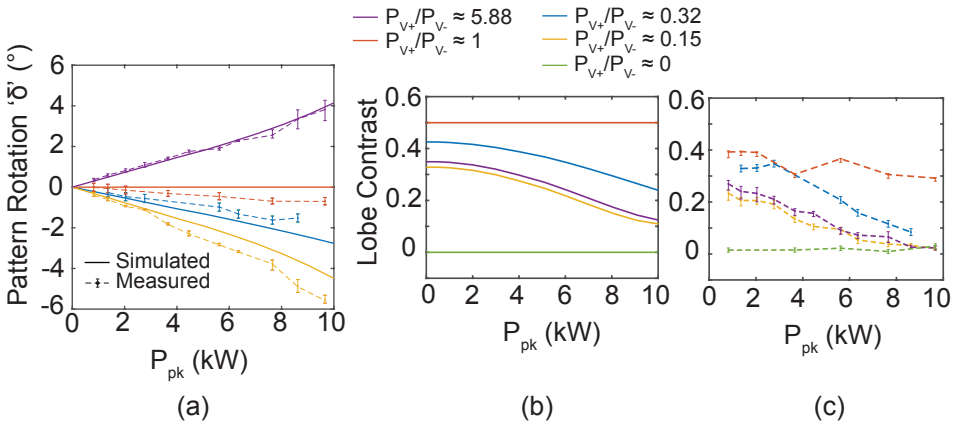

Figure 6.9: Results of image processing of measured time-averaged lobe images. (a) Rotation δ of measured and simulated images as a function of input power. (b) Reduction in lobe contrast in simulated images as a result of time-averaging. (c) Reduction in lobe contrast in measured images as a result of time-averaging. For (a)-(c), control cases of input SOP being linear and circular are also shown. Simulation plots are solid lines, experimental plots are dotted lines. (Data originally published in S.K. Dacha et al., Opt. Exp. Vol. 30, No. 11, 18481-18495 (2022) ©Optical Society of America)

6.9 Summary

In this chapter, we described our observation of a spin-orbit coupled generalization of the well-known nonlinear polarization rotation phenomenon. This phenomenon was observed in a hollow RCF that consisted of a tailored refractive index profile that allows for stable linear propagation of OAM modes and prevents linear mixing between the modes. We excited a combination of the two degenerate $L = \pm 10$ SO_{aa} modes using a metasurface q-plate. Using this setup, we demonstrated tunable excitation of the two modes by the convenient adjustment of a free-space QWP.

In order to observe the nonlinear rotation effect, we set the QWP to excite an unequal mixture of the two modes in the fiber. The resulting mode superposition consists of a spatially non-uniform elliptical state of polarization as displayed in Fig. 6.1. The ellipticity of the local elliptical state of polarization remains the same across the beam, but the orientation of the ellipse changes along the azimuthal direction. The exact orientation of the polarization pattern – or equivalently, the orientation of the ellipse at a given transverse spatial coordinate – is determined by the phase with which the two modes overlap.

The phase between the modes changes as a function of input power as a result of SPM and XPM, resulting in a power-dependent rotation of the polarization pattern. This was experimentally observed by imaging the output beam through a linear polarizer on a conventional camera. Image processing of the measured images and comparison with numerical simulations revealed close agreement between the two.

Although these measurements present an important step in furthering the literature on nonlinearly interacting OAM modes, many other interesting and important problems remain to be

studied. In the next and final chapter, we present some concluding remarks for this thesis, and present an outlook toward potentially interesting problems that may be worth pursuing in this research field.

Chapter 7: Conclusions & Outlook

In Chapter 1, we began our discussion on the 'why' of this research field where I claimed that this is a topic that should be of broad interest for not just the fiber optics community or even the optics community, but the scientific community overall. Through my description of the many novel and complex phenomena that we have observed and others in the field have, I hope first and foremost that MMNLFO has piqued your scientific interest and curiosity, and I hope that I have convinced you of the many possibilities that MMNLFO offers to the scientific community. As we discussed throughout this thesis, nonlinear phenomena in MMFs are not only of interest for SDM-based telecommunication technology, but they also pave the way for numerous other practical applications such as high power supercontinuum and ultrashort pulsed light sources, multimode amplifiers, high power optical beam delivery technology, optical metrology, quantum optics and communication, frequency and spatial mode conversion and biomedical imaging. MMNLFO is also fascinating from a fundamental physics perspective, not only thanks to the aforementioned parallels between the nonlinear wave equation to the equation describing bosonic gases and BECs, but also as it offers a unique perspective into other nonlinear coupled mode systems such as water waves [104].

Despite the fact that multimode fibers have existed for longer than single mode fibers have, we are only now beginning to develop an understanding of nonlinear propagation of multimodal

pulses. The surge in interest in the past decade has been motivated in part by the increasing need for SDM technology, and has been realized by recent theoretical [60, 61, 105], computational [53, 69] and experimental advances in the field. At the time of writing of this thesis, new tools continue to be developed, new applications continue to be identified, and new phenomena continue to be uncovered in the vast jungle of possibilities that MMNLFO is.

In this thesis, we report our humble attempt to push the envelope further. As we stated in Chapter 1, one of our research objectives was to shed more light on the "micro" picture, namely the nonlinear interactions between individual modes. In Chapter 3, we described our first efforts in that direction, where we saw that the radially symmetric modes of a parabolic GRIN fiber exhibit time-domain interference fringes that vary with power, fiber length as well as the transverse spatial coordinate, thereby demonstrating the spatiotemporal nature of nonlinear propagation in MMFs. In Chapter 4, we addressed the many limitations of those initial experiments and discussed a similar nonlinear mode interference effect occurring in a step-index FMF. With an improved characterization technique, we were able to demonstrate the first reported spatiotemporal measurements of multimodal nonlinearity [62]. In our effort to control the modes that were excited in the FMF, we also developed a technique with which to excite modes of a fiber selectively and efficiently. In Chapter 5, we utilized the spatiotemporal measurement technique once again to demonstrate that the Kerr-induced beam self-cleaning phenomenon in a time-resolved manner.

Finally, in Chapter 6, we described nonlinear experiments with the modes of a hollow RCF. We excited a superposition of a pair of degenerate SO_{aa} modes using a metasurface q-plate, and using analytical tools, numerical simulations and experimental evidence, we showed the occurrence of a spin-orbit coupled generalization of the well-known nonlinear polarization

rotation effect [71].

7.1 Future Directions

Although we have considered and worked on numerous interesting problems in the field over the past few years, many unstudied and unanswered problems still come to mind. Here, we outline a few such problems that could be of interest for future research.

7.1.1 Modulation Instability Phenomena

Modulation instability (MI) is a well-known phenomenon in single mode fibers, where a quasi-CW pulse propagating in the nonlinear regime can break up into a train of short pulses spontaneously, leading to the appearance of spectral sidebands [11]. MI requires anomalous dispersion ($\beta_2 < 0$) to occur in the case of a single polarization mode propagating in an SMF, but it can occur even in the normal dispersion ($\beta_2 > 0$) regime in the presence of two nonlinearly interacting polarization or spatial modes. MI has already been studied and observed in step and parabolic index fibers [16, 34, 36].

Modulation instability has also been studied in the context of OAM-carrying fiber modes of a ring core fiber [63], but so far there appears to be only one reported work that has considered the problem, and many questions remain unanswered. OAM modes in RCFs are excellent candidates for studying modulation instability because of the high contribution of waveguide dispersion to the overall dispersion experienced by the modes. More specifically, it is now known that for an input laser wavelength that would typically lie in the normal dispersion regime of fused silica, for example $\lambda_0 = 1064$ nm, the higher order modes of a RCF can in fact exhibit anomalous dispersion

at those wavelengths [26, 63]. As a result, different regimes of dispersion can be examined in the same fiber with the same light source by simply exciting a different spatial mode.

Recent experiments that we have conducted have yielded observations that hint at interesting phenomena arising from the fact that even if a single spatial mode is excited in an RCF and even if there is no linear coupling to other modes, nonlinear coupling still remains. Studying this problem could be experimentally challenging, and ideally it requires a way to resolve the output beam into the constituent modes. Although mode-resolved techniques have been demonstrated already [70], they are typically limited to linearly polarized modes of a conventional fiber. Further advancements in such characterization techniques might therefore be needed to be able to resolve the vector modes of a ring core fiber.

7.1.2 Spatiotemporally Resolved Polarization

A fascinating extension to the spatiotemporal near-field scanning technique that we described in Chapter 4 would be the capability to resolve the output not just in space and time, but also in polarization. As we described in Chapters 4 and 6, our method can be used for linearly polarized modes emerging from a conventional fiber. However, the polarization sensitivity of NSOM probes yields the method unusable for vector modes. Furthermore, even if the NSOM probe were not polarization sensitive, the near-field scanning method does not allow for the insertion of free-space polarization components in between the fiber and the probe. Exactly how one might extract the capability to spatially resolve the polarization of the output beam therefore remains an immense experimental challenge. However, such a technique could potentially unlock very interesting insights into the nonlinear rotation phenomenon that we described in Fig.

6.2 and Supplementary Video 3 in Chapter 6.

7.1.3 Applications of MMNLFO to Photonic Reservoir Computing

It is somewhat ironic that this is an idea that appears in the 'future directions' section of my thesis, as the work that we have carried out originally began with a discussion between me and my advisor on the possibility to use multimode fibers for photonic reservoir computing. However, we quickly realized that much remains to be understood about the nature of light propagation in MMFs, and so we decided that that would form my dissertation topic instead.

Photonic reservoir computing is a fast growing research field [106], and there already a few papers on using few-mode fibers to perform dendrite-like computational tasks in an efficient manner [107]. However, much remains to be done to advance research in this field. Given the complexity that MMFs offer in the nonlinear regime, MMNLFO could serve as a powerful platform to build machine learning algorithms, such as reservoir computing, on.

In every thesis on MMNLFO that you come across, you are likely to find a completely different set of ideas for future directions of research, and many of these ideas, if realized, have the potential to make great impact in natural and computer sciences research overall. To me, it is deeply fascinating and a little amusing that such great possibilities exist within a mere strand of glass.

Appendix A: FIB Mask Fabrication

In Chapter 4, we described the design of an FIB phase mask for achieving selective excitation of the radially symmetric LP_{0m} modes of a step-index FMF. Here, we briefly describe the fabrication method employed. Fig. A.1 shows a photograph of a custom fiber holder that was designed for the specific purpose of mounting it in a focused ion beam instrument. Although FIB has been used in the fiber context before, at the time of this fabrication, there were not very many guides on how to mount a fiber inside such an instrument.

The mount shown in Fig. A.1 is the final version of multiple iterations and a few different designs that we tried out. The structure of the mount consists of a bottom stem that was designed to be mounted in the slots provided inside the FIB instrument that we used. The top part consisted of a cuboidal section that held the fiber in a machined v-groove at a 55^0 degree angle to the vertical to match the angle of the incoming ion beam. The entire mount was milled in a machine shop from a single cubical block of steel. Conductive carbon tape and a colloidal silver paste were used to hold the fiber in place, and also to help dissipate charge.

The fiber end-face was first cleaved before it was stuck onto the mount as shown in Fig. A.1. The entire mount was then placed in a sputter deposition instrument where the fiber end-face was sputter-coated with a $\approx 80:20$ alloy of Au:Pd in a high vacuum chamber for approximately 120 seconds at a current setting of ≈ 15 mA. The mount was then transferred to the FIB instrument

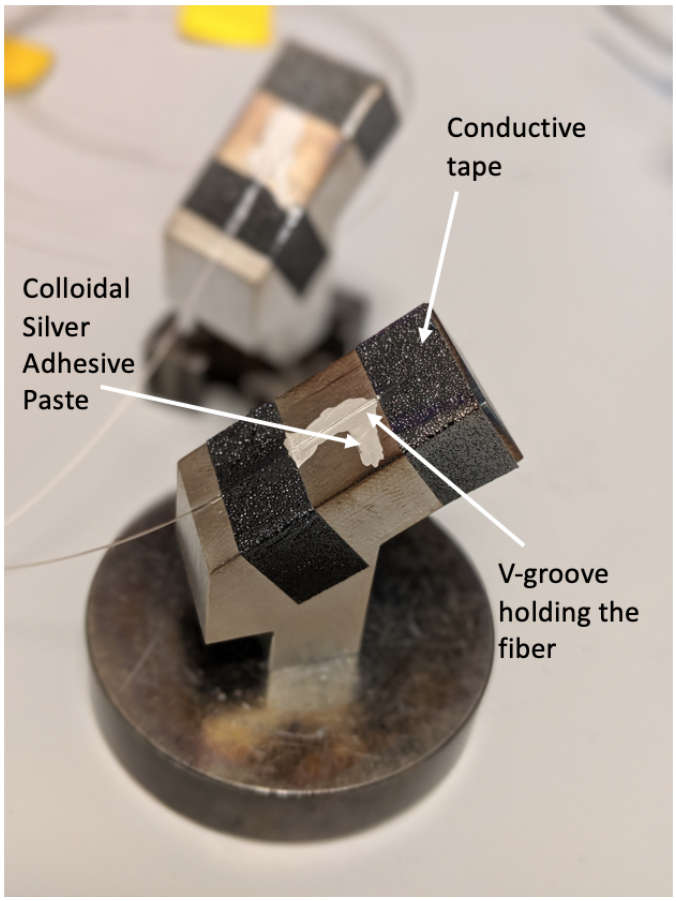

Figure A.1: Custom-designed fiber holder for FIB mask fabrication. The fiber is held at a 55^0 angle relative to the vertical so as to match the angle at which the ion beam is incident on the fiber.

(TESCAN GAIA3).

Scanning electron micrographs were obtained using the instrument's SEM functionality at a voltage setting of 20 kV. The FIB milling was performed by first ensuring that the ion beam is focused properly, and test patterns were performed on a trial fiber to ensure quality milling. The ion current was chosen based upon the desired mask size and geometry, but it was typically of the order of $0.1 - 0.5$ nA. It was found that using a small neutralization electron current during the milling process was useful in dissipating any excess Ga^+ charge that may accumulate on

the exposed fiber end-face, ensuring sharp edges in the mill pattern. The desired mill-depth was achieved upon iterations of calibrating instrument mill time vs depth measured using SEM tilt-corrected depth measurements. After the mill process completed, the fiber was dismounted from the v-groove, and the end-face was cleaned by carefully dipping it in an Aqua Regia solution to dissolve the metal.

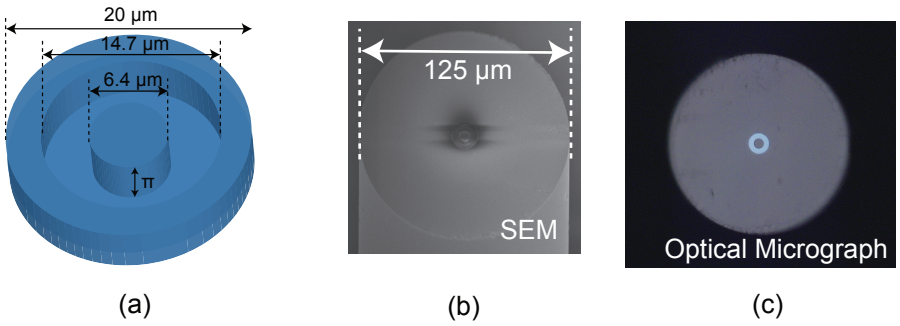

Figure A.2: (a) Desired mask design for example case of exciting the higher order LP_{03} mode selectively in a $2a = 20$ μm step-index FMF. Graphic shows the core area only. (b) Scanning electron micrograph showing the milled cross-section of the fiber. (c) Optical micrograph showing the milled mask pattern, imaged using a 50x magnifying lens.

Fig. A.2 shows the result of the entire process. Fig. A.2(a) shows an example mask design that is capable of exciting the higher order LP_{03} mode selectively, as we discussed in Chapter 4. Figures A.2(b) and A.2(c) show scanning electron and optical micrographs respectively of the fiber cross-section upon completion of the milling and metal removal processes. More complex designs may be achieved using this technique depending upon the desired feature sizes.

Appendix B: Example Calculations for $\mathscr{N}_{phkm}$ and $\Delta\beta_{phkm}$ for OAM Modes

Throughout this thesis, we have used the GMMNLSEs Eqs. 2.60 to model nonlinear interactions between a the spatial modes of fibers. In Chapter 6, we give the NLSEs for the two $|L| = 10$ SO_{aa} modes, but we do not provide a derivation there. In particular, it is worth asking the question of what other nonlinear terms exist if the equations were to be written for all 4 $|L| = 10$ OAM modes.

Additionally, most literature in the field of MMNLFO focuses on scalar modes, and in some cases vector HE and EH modes. However, as we saw from Eqs. 2.14, the OAM mode basis consists of modes that are not only vectorial in nature, but also complex. The form of the GMMNLSEs that we have used in Eqs. 2.60 is completely consistent with complex vector beams [61]. Here, we describe an instructive example which may be useful for a reader that is new to MMNLFO in the context of complex vector modes.

B.1 Coupled NLSEs and Mode Definitions

We begin our discussion by writing down the coupled NLSEs:

$$\partial_z A'_p = (-\delta\beta_1^{(p)}\partial_t - i\frac{\beta_2^{(p)}}{2}\partial_t^2)A'_p + i\frac{n_2\omega_0}{c}\mathscr{N}_{phkm}A'^{*}_h A'_k A'_m e^{i\Delta\beta_{phkm}} \tag{B.1}$$

where we have written the equations in terms of $A'_p(z,t) = A_p(z,t)e^{-i\beta_0^{(p)}z}$.

As we mentioned in Section 2.3.2.3, the $\Delta\beta_{phkm}$ is the phase matching term, whereas $\mathscr{N}_{phkm}$ is given by (from Eq. 2.61):

$$\mathscr{N}_{phkm} = \frac{2}{3}\int\int(\mathbf{e}_p^* \cdot \mathbf{e}_m)(\mathbf{e}_k \cdot \mathbf{e}_h^*)dxdy + \frac{1}{3}\int\int(\mathbf{e}_p^* \cdot \mathbf{e}_h^*)(\mathbf{e}_k \cdot \mathbf{e}_m)rdrd\phi \tag{B.2}$$

We express the 4 $|L| = 10$ modes as follows:

$$\mathbf{e}_1 = F_L(r)e^{iL\phi}\hat{\sigma_+} \tag{B.3a}$$

$$\mathbf{e}_2 = F_L(r)e^{-iL\phi}\hat{\sigma_-} \tag{B.3b}$$

$$\mathbf{e}_3 = F_L(r)e^{iL\phi}\hat{\sigma_-} \tag{B.3c}$$

$$\mathbf{e}_4 = F_L(r)e^{-iL\phi}\hat{\sigma_+} \tag{B.3d}$$

The first two modes are the spin-orbit aligned modes, while the last two are the spin-orbit aligned modes. For these modes, we have, as we discussed in Section 2.2.6:

$$\beta_0^{(1)} = \beta_0^{(2)} \neq \beta_0^{(3)} = \beta_0^{(4)} \tag{B.4}$$

B.2 Phase Matching

We begin by setting the first index p to 3, denoting that we want to write the NLSE for the $\mathbf{e}_3$ mode. For a nonlinear term to be phase-matched, we require that $\Delta\beta_{phkm} = \Delta\beta_{3hkm} = 0$.

In general, for 4 modes under consideration, there are $4 \times 4 \times 4 = 64$ possible combinations

of $3hkm$. Imposing the constraint $\Delta\beta_{3hkm} = 0$, however, reduces the number of terms needed to be calculated. This is because possible values of hkm for which $\Delta\beta_{3hkm} = \beta_0^{(k)} + \beta_0^{(m)} - \beta_0^{(h)} - \beta_0^{(3)} = 0$ are the following sets:

- k is either 3 or 4, m and h are either 1 or 2 OR m and h are either 3 or 4
- m is either 3 or 4, k and h are either 1 or 2 OR k and h are either 3 or 4

These possibilities are listed (in a less confusing manner) in the first columns of Tables B.1, B.2, B.3 and B.4. We are now left with 32 possible terms. For all other possibilities of $3hkm$, $\Delta\beta_{3hkm}$ can be shown to be $\neq 0$.

B.3 Calculation of Nonlinear Coefficients

We now evaluate whether the $\mathscr{N}_{3hkm}$ coefficients are non-zero for the remaining $3hkm$ terms. In doing this calculation, we adopt the following convention for the dot product of complex vectors [61]:

$$|\mathbf{V}|^2 = \mathbf{V}^* \cdot \mathbf{V} = |V_x|^2 + |V_y|^2 \tag{B.5}$$

where $\mathbf{V}$ is some complex valued vector with cartesian components V_x and V_y. Note that with this notation, we have:

$$\hat{\sigma_+} \cdot \hat{\sigma_+} = \frac{(\hat{\mathbf{x}} + i\hat{\mathbf{y}})}{2} \cdot \frac{(\hat{\mathbf{x}} + i\hat{\mathbf{y}})}{2} = 0 \tag{B.6}$$

and

$$\hat{\sigma_+} \cdot \hat{\sigma_-} = \frac{(\hat{\mathbf{x}} + i\hat{\mathbf{y}})}{2} \cdot \frac{(\hat{\mathbf{x}} - i\hat{\mathbf{y}})}{2} = 1 \tag{B.7}$$

which is counter-intuitive.

We first show the calculation for an example $\mathscr{N}_{3hkm}$ term, and later list only whether the constituent terms in $\mathscr{N}_{3hkm}$ are zero or non-zero in Tables B.1, B.2, B.3 and B.4. Consider the case $3hkm = 3131$. The first integral in Eq. B.2, say $\mathscr{N}_1$, can be calculated as:

$$\begin{aligned}
\mathscr{N}_1 &= \frac{2}{3}\int\int(\mathbf{e}_3^* \cdot \mathbf{e}_1)(\mathbf{e}_1 \cdot \mathbf{e}_3^*) r dr d\phi \\
&= \frac{2}{3}\int\int\Big((F_L(r)e^{iL\phi}\hat{\sigma_-})^* \cdot (F_L(r)e^{iL\phi}\hat{\sigma_+})\Big)\Big((F_L(r)e^{iL\phi}\hat{\sigma_+}) \cdot (F_L(r)e^{iL\phi}\hat{\sigma_-})^*\Big) r dr d\phi \\
&= 0
\end{aligned} \tag{B.8}$$

where in the last step, we find that the integral is zero because both the first and second terms in the integrand product involve the dot product $\hat{\sigma_+} \cdot \hat{\sigma_+}$, which is 0.

The second term in the nonlinear coefficient, $\mathscr{N}_2$, can be calculated as:

$$\begin{aligned}
\mathscr{N}_2 &= \frac{1}{3}\int\int(\mathbf{e}_3^* \cdot \mathbf{e}_1^*)(\mathbf{e}_1 \cdot \mathbf{e}_3) r dr d\phi \\
&= \frac{1}{3}\int\int\Big((F_L(r)e^{iL\phi}\hat{\sigma_-})^* \cdot (F_L(r)e^{iL\phi}\hat{\sigma_+})^*\Big)\Big((F_L(r)e^{iL\phi}\hat{\sigma_+}) \cdot (F_L(r)e^{iL\phi}\hat{\sigma_-})\Big) r dr d\phi \\
&= \frac{1}{3}\int\int |F_L|^4(r)\Big(e^{-iL\phi}e^{-iL\phi}\Big)\Big(e^{iL\phi}e^{iL\phi}\Big) r dr d\phi \\
&= \frac{2\pi}{3} I_r
\end{aligned} \tag{B.9}$$

where in the penultimate step we have made use of the identity $\hat{\sigma_+} \cdot \hat{\sigma_-} = 1$. The 2π results from the azimuthal part of the integral, and I_r is the radial integral defined as follows:

$$I_r = \int \int |F_L|^4(r) r dr \tag{B.10}$$

Similarly, the nonlinear coefficients $\mathscr{N}_{3hkm}$ can be calculated for other allowed combinations of the indices $3hkm$. In Tables B.1, B.2, B.3 and B.4, we list the resulting $\mathscr{N}_1$ and $\mathscr{N}_2$ terms for all combinations of $3hkm$ for which $\Delta\beta_{3hkm} = 0$.

Following these calculations, we finally end up with the coupled NLSE for the $p = 3$ mode. However, this equation can be generalized to any p mode, with p being any number from 1 to 4, since we have not made any assumptions that are particular to $p = 3$. The resulting NLSEs are then given as:

$$\partial_z A'_p = (-\delta\beta_1^{(p)}\partial_t - i\frac{\beta_2^{(p)}}{2}\partial_t^2)A'_p + i2\pi I_r \frac{n_2\omega_0}{c}\left(\frac{2}{3}|A'_p|^2 + \frac{4}{3}\sum_{h\neq p}|A'_h|^2\right)A'_p \tag{B.11}$$

Table B.1: Zero and Nonzero $\mathscr{N}_{phkm}$ Coefficients for $|L| = 10$ OAM Modes - Part 1

$3hkm$	$\mathscr{N}_1 = \frac{2}{3}\int\int(\mathbf{e}_p^* \cdot \mathbf{e}_m)(\mathbf{e}_k \cdot \mathbf{e}_h^*)dxdy$ $(\times 2\pi I_r)$	$\mathscr{N}_2 = \frac{1}{3}\int\int(\mathbf{e}_p^* \cdot \mathbf{e}_h^*)(\mathbf{e}_k \cdot \mathbf{e}_m)dxdy$ $(\times 2\pi I_r)$	$\mathscr{N}_{phkm}$ $(\times 2\pi I_r)$
3131	0	1/3	1/3
3232	2/3	0	2/3
3333	2/3	0	2/3
3434	0	1/3	1/3
3132	0	0	0
3231	0	0	0
3334	0	0	0
3433	0	0	0

Table B.2: Zero and Nonzero $\mathscr{N}_{phkm}$ Coefficients for $|L| = 10$ OAM Modes - Part 2

$3hkm$	$\mathscr{N}_1 = \frac{2}{3}\int\int(\mathbf{e}_p^* \cdot \mathbf{e}_m)(\mathbf{e}_k \cdot \mathbf{e}_h^*)dxdy$ $(\times 2\pi I_r)$	$\mathscr{N}_2 = \frac{1}{3}\int\int(\mathbf{e}_p^* \cdot \mathbf{e}_h^*)(\mathbf{e}_k \cdot \mathbf{e}_m)dxdy$ $(\times 2\pi I_r)$	$\mathscr{N}_{phkm}$ $(\times 2\pi I_r)$
3141	0	0	0
3242	0	0	0
3343	0	0	0
3444	0	0	0
3142	0	0	0
3241	0	0	0
3344	0	0	0
3443	2/3	1/3	1

Table B.3: Zero and Nonzero $\mathscr{N}_{phkm}$ Coefficients for $|L| = 10$ OAM Modes - Part 3

$3hkm$	$\mathscr{N}_1 = \frac{2}{3}\int\int(\mathbf{e}_p^* \cdot \mathbf{e}_m)(\mathbf{e}_k \cdot \mathbf{e}_h^*)dxdy$ $(\times 2\pi I_r)$	$\mathscr{N}_2 = \frac{1}{3}\int\int(\mathbf{e}_p^* \cdot \mathbf{e}_h^*)(\mathbf{e}_k \cdot \mathbf{e}_m)dxdy$ $(\times 2\pi I_r)$	$\mathscr{N}_{phkm}$ $(\times 2\pi I_r)$
3113	2/3	1/3	1
3223	2/3	0	2/3
3333	2/3	0	2/3
3443	2/3	1/3	1
3123	0	0	0
3213	0	0	0
3343	0	0	0
3433	0	0	0

Table B.4: Zero and Nonzero $\mathscr{N}_{phkm}$ Coefficients for $|L| = 10$ OAM Modes - Part 4

$3hkm$	$\mathscr{N}_1 = \frac{2}{3}\int\int(\mathbf{e}_p^* \cdot \mathbf{e}_m)(\mathbf{e}_k \cdot \mathbf{e}_h^*)dxdy$ $(\times 2\pi I_r)$	$\mathscr{N}_2 = \frac{1}{3}\int\int(\mathbf{e}_p^* \cdot \mathbf{e}_h^*)(\mathbf{e}_k \cdot \mathbf{e}_m)dxdy$ $(\times 2\pi I_r)$	$\mathscr{N}_{phkm}$ $(\times 2\pi I_r)$
3114	0	0	0
3224	0	0	0
3334	0	0	0
3444	0	0	0
3124	0	0	0
3214	0	0	0
3344	0	0	0
3434	0	1/3	1/3

Appendix C: List of Publications

- **Sai Kanth Dacha**, Wenqi Zhu, Amit Agrawal, Kenneth J. Ritter, and Thomas E. Murphy, "Nonlinear rotation of spin-orbit coupled states in hollow ring-core fibers," Opt. Express 30, 18481-18495 (2022)

- **Sai Kanth Dacha** and Thomas E. Murphy, "Spatiotemporal characterization of nonlinear intermodal interference between selectively excited modes of a few-Mode fiber", Optica 7, 1796-1803 (2020)

- **S. K. Dacha**, W. Zhu, A. Agrawal, and T. E. Murphy, "Kerr-induced Rotation of Mixed Orbital Angular Momentum States in Hollow Ring-Core Fibers," in Optical Fiber Communication Conference (OFC) 2022, paper W2A.13

- **S. K. Dacha** and T. E. Murphy, "(2+1)D Spatiotemporal Characterization of Nonlinear Interactions between Selectively Excited Spatial Modes of a Few-Mode Fiber," in Conference on Lasers and Electro-Optics, OSA Technical Digest (Optical Society of America, 2020), paper FTh3A.6

- **S. K. Dacha** and T. E. Murphy, "Time-Domain Interference of Nonlinearly Interacting Spatial Modes in a Multimode Fiber," 2018 Conference on Lasers and Electro-Optics (CLEO), 2018

Bibliography

[1] Z.I. Alferov. The History and Future of Semiconductor Heterostructures. *Semiconductors*, 32:1–14, 1998.

[2] R.J. Mears, L. Reekie, I.M. Jauncey, and D.N. Payne. Low-noise erbium-doped fibre amplifier operating at 1.54 μm. *Electronics Letters*, 23(19):1026–1028, 1987.

[3] Kwan Chi Kao and G. A. Hockham. Dielectric-fibre surface waveguides for optical frequencies. 1966.

[4] M.G. Taylor. Coherent detection method using DSP for demodulation of signal and subsequent equalization of propagation impairments. *IEEE Photonics Technology Letters*, 16(2):674–676, 2004.

[5] P.J. Winzer and R.-J. Essiambre. Advanced Optical Modulation Formats. *Proceedings of the IEEE*, 94(5):952–985, 2006.

[6] Weizhao Tang, Lucianna Kiffer, Giulia Fanti, and Ari Juels. Strategic latency reduction in blockchain peer-to-peer networks, *arXiv 2205.06837*, 2022.

[7] G.P. Agrawal. *Fiber-Optic Communication Systems*. Wiley, 2021.

[8] Kiyoshi Fukuchi, Tadashi Kasamatsu, Masao Morie, Risato Ohhira, Toshiharu Ito, Kayato Sekiya, Daisaku Ogasahara, and Takashi Ono. 10.92-Tb/s (273 × 40-Gb/s) triple-band/ultra-dense WDM optical-repeatered transmission experiment. In *Optical Fiber Communication Conference and International Conference on Quantum Information*, page PD24. Optica Publishing Group, 2001.

[9] A.R. Chraplyvy, A.H. Gnauck, R.W. Tkach, J.L. Zyskind, J.W. Sulhoff, A.J. Lucero, Y. Sun, R.M. Jopson, F. Forghieri, R.M. Derosier, C. Wolf, and A.R. McCormick. 1-Tb/s transmission experiment. *IEEE Photonics Technology Letters*, 8(9):1264–1266, 1996.

[10] C. E. Shannon. A mathematical theory of communication. *The Bell System Technical Journal*, 27(3):379–423, 1948.

[11] Govind Agrawal. *Nonlinear Fiber Optics*. Elsevier, 5 edition, 2012.

[12] D. J. Richardson, J. M. Fini, and L. E. Nelson. Space-division multiplexing in optical fibres. *Nat. Photon.*, 7(5):354–362, 2013.

[13] René-Jean Essiambre and Robert W. Tkach. Capacity Trends and Limits of Optical Communication Networks. *Proceedings of the IEEE*, 100(5):1035–1055, 2012.

[14] Zhanwei Liu, Logan G. Wright, Demetrios N. Christodoulides, and Frank W. Wise. Kerr self-cleaning of femtosecond-pulsed beams in graded-index multimode fiber. *Opt. Lett.*, 41(16):3675–3678, Aug 2016.

[15] K. Krupa, A. Tonello, B. M. Shalaby, M. Fabert, A. Barthélémy, G. Millot, S. Wabnitz, and V. Couderc. Spatial beam self-cleaning in multimode fibres. *Nat. Photon.*, 11(4):237–241, 2017.

[16] Logan G. Wright, Zhanwei Liu, Daniel A. Nolan, Ming-Jun Li, Demetrios N. Christodoulides, and Frank W. Wise. Self-organized instability in graded-index multimode fibres. *Nat. Photon.*, 10(12):771–776, 2016.

[17] Katarzyna Krupa, Alessandro Tonello, Alain Barthélémy, Vincent Couderc, Badr Mohamed Shalaby, Abdelkrim Bendahmane, Guy Millot, and Stefan Wabnitz. Observation of Geometric Parametric Instability Induced by the Periodic Spatial Self-Imaging of Multimode Waves. *Phys. Rev. Lett.*, 116:183901, May 2016.

[18] K. Krupa, C. Louot, V. Couderc, M. Fabert, R. Guenard, B. M. Shalaby, A. Tonello, D. Pagnoux, P. Leproux, A. Bendahmane, R. Dupiol, G. Millot, and S. Wabnitz. Spatiotemporal characterization of supercontinuum extending from the visible to the mid-infrared in a multimode graded-index optical fiber. *Opt. Lett.*, 41(24):5785–5788, Dec 2016.

[19] W. H. Renninger and F. W. Wise. Optical solitons in graded-index multimode fibres. *Nat. Commun.*, 4(1):1719, 2013.

[20] L. Rishøj, B. Tai, P. Kristensen, and S. Ramachandran. Soliton self-mode conversion: revisiting Raman scattering of ultrashort pulses. *Optica*, 6(3):304–308, Mar 2019.

[21] M. A. Eftekhar, L. G. Wright, M. S. Mills, M. Kolesik, R. Amezcua Correa, F. W. Wise, and D. N. Christodoulides. Versatile supercontinuum generation in parabolic multimode optical fibers. *Opt. Express*, 25(8):9078–9087, Apr 2017.

[22] Joseph C. Jing, Xiaoming Wei, and Lihong V. Wang. Spatio-temporal-spectral imaging of non-repeatable dissipative soliton dynamics. *Nat. Commun.*, 11(1):2059, 2020.

[23] Hamed Pourbeyram and Arash Mafi. Photon pair generation with tailored frequency correlations in graded-index multimode fibers. *Opt. Lett.*, 43(9):2018–2021, May 2018.

[24] Katarzyna Krupa, Alessandro Tonello, Alain Barthélémy, Tigran Mansuryan, Vincent Couderc, Guy Millot, Philippe Grelu, Daniele Modotto, Sergey A. Babin, and Stefan Wabnitz. Multimode nonlinear fiber optics, a spatiotemporal avenue. *APL Photonics*, 4(11):110901, 2019.

[25] Logan G. Wright, Demetrios N. Christodoulides, and Frank W. Wise. Spatiotemporal mode-locking in multimode fiber lasers. *Science*, 358(6359):94–97, 2017.

[26] G. Prabhakar, L. Rishoj, P. Gregg, P. Kristensen, and S. Ramachandran. Octave-wide supercontinuum generation of light-carrying orbital angular momentum. *Opt. Express*, 27:11547–11556, 4 2019.

[27] Ioannis N. Papadopoulos, Salma Farahi, Christophe Moser, and Demetri Psaltis. High-resolution, lensless endoscope based on digital scanning through a multimode optical fiber. *Biomed. Opt. Express*, 4(2):260–270, Feb 2013.

[28] Rafael R. Gattass and Eric Mazur. Femtosecond laser micromachining in transparent materials. *Nature Photonics*, 2(4):219–225, Apr 2008.

[29] Koji Sugioka and Ya Cheng. Ultrafast lasers—reliable tools for advanced materials processing. *Light: Science & Applications*, 3(4):149–149, Apr 2014.

[30] J. Garnier, A. Fusaro, K. Baudin, C. Michel, K. Krupa, G. Millot, and A. Picozzi. Wave condensation with weak disorder versus beam self-cleaning in multimode fibers. *Physical Review A*, 100(5), November 2019.

[31] J Rogel-Salazar. The Gross–Pitaevskii equation and Bose–Einstein condensates. *European Journal of Physics*, 34(2):247–257, jan 2013.

[32] Hamed Pourbeyram, Pavel Sidorenko, Fan O. Wu, Nicholas Bender, Logan Wright, Demetrios N. Christodoulides, and Frank Wise. Direct observations of thermalization to a Rayleigh–Jeans distribution in multimode optical fibres. *Nature Physics*, Apr 2022.

[33] R. Dupiol, A. Bendahmane, K. Krupa, A. Tonello, M. Fabert, B. Kibler, T. Sylvestre, A. Barthelemy, V. Couderc, S. Wabnitz, and G. Millot. Far-detuned cascaded intermodal four-wave mixing in a multimode fiber. *Opt. Lett.*, 42(7):1293–1296, Apr 2017.

[34] R. Dupiol, A. Bendahmane, K. Krupa, J. Fatome, A. Tonello, M. Fabert, V. Couderc, S. Wabnitz, and G. Millot. Intermodal modulational instability in graded-index multimode optical fibers. *Opt. Lett.*, 42(17):3419–3422, Sep 2017.

[35] Abdelkrim Bendahmane, Katarzyna Krupa, Alessandro Tonello, Daniele Modotto, Thibaut Sylvestre, Vincent Couderc, Stefan Wabnitz, and Guy Millot. Seeded intermodal four-wave mixing in a highly multimode fiber. *J. Opt. Soc. Am. B*, 35(2):295–301, Feb 2018.

[36] Lei Li, Jinyong Leng, Pu Zhou, and Jinbao Chen. Modulation instability induced by intermodal cross-phase modulation in step-index multimode fiber. *Appl. Opt.*, 58(16):4283–4287, Jun 2019.

[37] L. Allen, M. W. Beijersbergen, R. J. C. Spreeuw, and J. P. Woerdman. Orbital angular momentum of light and the transformation of Laguerre-Gaussian laser modes. *Phys. Rev. A*, 45:8185, 6 1992.

[38] Charles Brunet, Pravin Vaity, Younès Messaddeq, Sophie LaRochelle, and Leslie A Rusch. Design, fabrication and validation of an OAM fiber supporting 36 states. *Opt. Express*, 22:26117–26127, 10 2014.

[39] P. Gregg, P. Kristensen, and S. Ramachandran. Conservation of orbital angular momentum in air-core optical fibers. *Optica*, 2(3):267–270, Mar 2015.

[40] P. Gregg, P. Kristensen, A. Rubano, S. Golowich, L. Marrucci, and S. Ramachandran. Enhanced spin orbit interaction of light in highly confining optical fibers for mode division multiplexing. *Nat. Commun.*, 10:1–8, 10 2019.

[41] A. Ghatak and K. Thyagarajan. *An Introduction to Fiber Optics*. Cambridge University Press, 1998.

[42] A.W. Snyder and J. Love. *Optical Waveguide Theory*. Springer US, 2012.

[43] Nenad Bozinovic. *Orbital angular momentum in optical fibers*. OpenBU, 2013.

[44] D. Gloge. Optical power flow in multimode fibers. *The Bell System Technical Journal*, 51(8):1767–1783, 1972.

[45] D. Gloge and E. A. J. Marcatili. Multimode theory of graded-core fibers. *The Bell System Technical Journal*, 52(9):1563–1578, 1973.

[46] Robert Olshansky. Mode Coupling Effects in Graded-Index Optical Fibers. *Appl. Opt.*, 14(4):935–945, Apr 1975.

[47] D. Marcuse. *Theory of Dielectric Optical Waveguides, 2nd ed.* Elsevier Science, 1991.

[48] Zimu Zhu. *Nonlinear optical pulse propagation in multimode waveguides*. Cornell eCommons, 2020.

[49] A. Bjarklev. Microdeformation losses of single-mode fibers with step-index profiles. *Journal of Lightwave Technology*, 4(3):341–346, 1986.

[50] Zelin Ma and Siddharth Ramachandran. *Propagation stability in optical fibers: role of path memory and angular momentum*, pages 213–228. De Gruyter, 2021.

[51] Siddharth Ramachandran, Poul Kristensen, and Man F. Yan. Generation and propagation of radially polarized beams in optical fibers. *Opt. Lett.*, 34(16):2525–2527, Aug 2009.

[52] H.G. Unger. *Planar Optical Waveguides and Fibres*. Oxford engineering science series. Clarendon Press, 1977.

[53] Arman B. Fallahkhair, Kai S. Li, and Thomas E. Murphy. Vector Finite Difference Modesolver for Anisotropic Dielectric Waveguides. *J. Lightwave Technol.*, 26(11):1423–1431, Jun 2008.

[54] Michael Steinke. Full-Vectorial Fiber Mode Solver Based on a Discrete Hankel Transform. *Photonics*, 8(10), 2021.

[55] Maitreyi Sangal, Christoph H. Keitel, and Matteo Tamburini. Observing light-by-light scattering in vacuum with an asymmetric photon collider. *Phys. Rev. D*, 104:L111101, Dec 2021.

[56] R.W. Boyd. *Nonlinear Optics*. Elsevier Science, 2020.

[57] Y. Kodama and A. Hasegawa. Nonlinear pulse propagation in a monomode dielectric guide. *IEEE Journal of Quantum Electronics*, 23(5):510–524, 1987.

[58] K.J. Blow and D. Wood. Theoretical description of transient stimulated Raman scattering in optical fibers. *IEEE Journal of Quantum Electronics*, 25(12):2665–2673, 1989.

[59] P. V. Mamyshev and S. V. Chernikov. Ultrashort-pulse propagation in optical fibers. *Opt. Lett.*, 15(19):1076–1078, Oct 1990.

[60] Francesco Poletti and Peter Horak. Description of ultrashort pulse propagation in multimode optical fibers. *J. Opt. Soc. Am. B*, 25(10):1645–1654, Oct 2008.

[61] Cristian Antonelli, Mark Shtaif, and Antonio Mecozzi. Modeling of Nonlinear Propagation in Space-Division Multiplexed Fiber-Optic Transmission. *J. Lightwave Technol.*, 34:36–54, 1 2016.

[62] Sai Kanth Dacha and Thomas E. Murphy. Spatiotemporal characterization of nonlinear intermodal interference between selectively excited modes of a few-mode fiber. *Optica*, 7(12):1796–1803, Dec 2020.

[63] X. Liu, E. N. Christensen, K. Rottwitt, and S. Ramachandran. Nonlinear four-wave mixing with enhanced diversity and selectivity via spin and orbital angular momentum conservation. *APL Photonics*, 5:010802, 1 2020.

[64] Yuzhe Xiao, René-Jean Essiambre, Marc Desgroseilliers, Antonia M. Tulino, Roland Ryf, Sami Mumtaz, and Govind P. Agrawal. Theory of intermodal four-wave mixing with random linear mode coupling in few-mode fibers. *Opt. Express*, 22(26):32039–32059, Dec 2014.

[65] Logan G. Wright, William H. Renninger, Demetrios N. Christodoulides, and Frank W. Wise. Spatiotemporal dynamics of multimode optical solitons. *Opt. Express*, 23(3):3492–3506, Feb 2015.

[66] Zimu Zhu, Logan G. Wright, Demetrios N. Christodoulides, and Frank W. Wise. Observation of multimode solitons in few-mode fiber. *Opt. Lett.*, 41(20):4819–4822, Oct 2016.

[67] Nathan B. Terry, Thomas G. Alley, and Timothy H. Russell. An explanation of SRS beam cleanup in graded-index fibers and the absence of SRS beam cleanup in step-index fibers. *Opt. Express*, 15(26):17509–17519, Dec 2007.

[68] Pleban Ross, Afrouz Azari, Reza Salem, and Thomas E. Murphy. General-purpose symmetrized split-step software (SSPROP). `https://photonics.umd.edu/software/ssprop/`.

[69] Logan G. Wright, Zachary M. Ziegler, Pavel M. Lushnikov, Zimu Zhu, M. Amin Eftekhar, Demetrios N. Christodoulides, and Frank W. Wise. Multimode Nonlinear Fiber Optics: Massively Parallel Numerical Solver, Tutorial, and Outlook. *IEEE Journal of Selected Topics in Quantum Electronics*, 24(3):1–16, 2018.

[70] Zimu Zhu, Logan G. Wright, Joel Carpenter, Dan Nolan, Ming-Jun Li, Demetrios N. Christodoulides, and Frank W. Wise. Mode-Resolved Control and Measurement of Nonlinear Pulse Propagation in Multimode Fibers. In *Conference on Lasers and Electro-Optics*, page FTh4E.7. Optical Society of America, 2018.

[71] Sai Kanth Dacha, Wenqi Zhu, Amit Agrawal, Kenneth J. Ritter, and Thomas E. Murphy. Nonlinear rotation of spin-orbit coupled states in hollow ring-core fibers. *Opt. Express*, 30(11):18481–18495, May 2022.

[72] Zhenwei Xie, Shecheng Gao, Ting Lei, Shengfei Feng, Yan Zhang, Fan Li, Jianbo Zhang, Zhaohui Li, and Xiaocong Yuan. Integrated (de)multiplexer for orbital angular momentum fiber communication. *Photon. Res.*, 6(7):743–749, Jul 2018.

[73] Chin-Lin Chen. Excitation of higher order modes in optical fibers with parabolic index profile. *Appl. Opt.*, 27(11):2353–2356, Jun 1988.

[74] Gorgi Kostovski, Paul R. Stoddart, and Arnan Mitchell. The Optical Fiber Tip: An Inherently Light-Coupled Microscopic Platform for Micro- and Nanotechnologies. *Adv. Matter.*, 26(23):3798–3820, 2014.

[75] J. J. Zayhowski and A. Mooradian. Single-frequency microchip nd lasers. *Opt. Lett.*, 14(1):24–26, Jan 1989.

[76] Y. Leventoux, G. Granger, K. Krupa, A. Tonello, G. Millot, M. Ferraro, F. Mangini, M. Zitelli, S. Wabnitz, S. Février, and V. Couderc. 3D time-domain beam mapping for studying nonlinear dynamics in multimode optical fibers. *Opt. Lett.*, 46(1):66–69, Jan 2021.

[77] F. Mangini, M. Gervaziev, M. Ferraro, D. S. Kharenko, M. Zitelli, Y. Sun, V. Couderc, E. V. Podivilov, S. A. Babin, and S. Wabnitz. Statistical mechanics of beam self-cleaning in GRIN multimode optical fibers. *Opt. Express*, 30(7):10850–10865, Mar 2022.

[78] Nenad Bozinovic, Yang Yue, Yongxiong Ren, Moshe Tur, Poul Kristensen, Hao Huang, Alan E. Willner, and Siddharth Ramachandran. Terabit-scale orbital angular momentum mode division multiplexing in fibers. *Science*, 340:1545–1548, 2013.

[79] Jian Wang, Jeng Yuan Yang, Irfan M. Fazal, Nisar Ahmed, Yan Yan, Hao Huang, Yongxiong Ren, Yang Yue, Samuel Dolinar, Moshe Tur, and Alan E. Willner. Terabit free-space data transmission employing orbital angular momentum multiplexing. *Nat. Photonics*, 6:488–496, 6 2012.

[80] B Ung, P Vaity, L Wang, Y Messaddeq, L A Rusch, and S LaRochelle. Few-mode fiber with inverse-parabolic graded-index profile for transmission of OAM-carrying modes. *Opt. Express*, 22:18044–18055, 7 2014.

[81] Fan Zhang, Kaiheng Zou, Yixiao Zhu, and Zhennan Zheng. 1.44 Tb/s free-space IM-DD transmission employing OAM multiplexing and PDM. *Opt. Express*, 24:3967–3980, 2 2016.

[82] A. Mair, A. Vaziri, G. Weihs, and A. Zeilinger. Entanglement of the orbital angular momentum states of photons. *Nature*, 412:313–316, 7 2001.

[83] Lorenzo Marrucci, Ebrahim Karimi, Sergei Slussarenko, Bruno Piccirillo, Enrico Santamato, Eleonora Nagali, and Fabio Sciarrino. Spin-to-orbital conversion of the angular momentum of light and its classical and quantum applications. *J. Opt.*, 13:064001, 4 2011.

[84] David Bacco, Daniele Cozzolino, Beatrice Da Lio, Yunhong Ding, Karsten Rottwitt, and Leif Katsuo Oxenlowe. Quantum communication with orbital angular momentum. In *2020 22nd International Conference on Transparent Optical Networks (ICTON)*, pages 1–4. IEEE Computer Society, 2020.

[85] Aniceto Belmonte, Carmelo Rosales-Guzmán, and Juan P. Torres. Measurement of flow vorticity with helical beams of light. *Optica*, 2:1002–1005, 11 2015.

[86] E Otte and C Denz. Optical trapping gets structure: Structured light for advanced optical manipulation. *Appl. Phys. Rev.*, 7:41308, 2020.

[87] Mario Krenn, Mehul Malik, Manuel Erhard, and Anton Zeilinger. Orbital angular momentum of photons and the entanglement of Laguerre–Gaussian modes. *Philos. Trans. R. Soc. A*, 375, 2 2017.

[88] Robert Fickler, Geoff Campbell, Ben Buchler, Ping Koy Lam, and Anton Zeilinger. Quantum entanglement of angular momentum states with quantum numbers up to 10,010. *Proc. Natl. Acad. Sci. U.S.A.*, 113:13642–13647, 11 2016.

[89] Jonathan Leach, Barry Jack, Jacqui Romero, Anand K. Jha, Alison M. Yao, Sonja Franke-Arnold, David G. Ireland, Robert W. Boyd, Stephen M. Barnett, and Miles J. Padgett. Quantum correlations in optical angle-orbital angular momentum variables. *Science*, 329:662–665, 8 2010.

[90] A. Ashkin. Acceleration and Trapping of Particles by Radiation Pressure. *Phys. Rev. Lett.*, 24:156, 1 1970.

[91] David G. Grier. A revolution in optical manipulation. *Nature*, 424:810–816, 2003.

[92] Yuanjie Yang, Yu Xuan Ren, Mingzhou Chen, Yoshihiko Arita, and Carmelo Rosales-Guzmán. Optical trapping with structured light: a review. *Adv. Photonics*, 3:034001, 5 2021.

[93] René-Jean Essiambre. Arthur Ashkin: Father of the optical tweezers. *Proceedings of the National Academy of Sciences*, 118(7):e2026827118, 2021.

[94] S. Ramachandran, P. Gregg, P. Kristensen, and S. E. Golowich. On the scalability of ring fiber designs for OAM multiplexing. *Opt. Express*, 23(3):3721–3730, Feb 2015.

[95] Miles J. Padgett, Siddharth Ramachandran, Steven D. Johnson, and Zelin Ma. Measurement of the spin-orbit coupling interaction in ring-core optical fibers. *OSA Continuum*, 2:2975–2982, 10 2019.

[96] S. S.R. Oemrawsingh, J. A.W. Van Houwelingen, E. R. Eliel, J. P. Woerdman, E. J.K. Verstegen, J. G. Kloosterboer, and G. W. T Hooft. Production and characterization of spiral phase plates for optical wavelengths. *Appl. Opt.*, 43:688–694, 1 2004.

[97] V. Yu Bazhenov, M. S. Soskin, and M. V. Vasnetsov. Screw Dislocations in Light Wavefronts. *J. Mod. Opt.*, 39:985–990, 1992.

[98] M. W. Beijersbergen, L. Allen, H. E.L.O. van der Veen, and J. P. Woerdman. Astigmatic laser mode converters and transfer of orbital angular momentum. *Opt. Commun.*, 96:123–132, 2 1993.

[99] Andrea Rubano, Bruno Piccirillo, Filippo Cardano, and Lorenzo Marrucci. Q-plate technology: a progress review [Invited]. *J. Opt. Soc. Am. B*, 36:D70–D87, 5 2019.

[100] Robert C. Devlin, Antonio Ambrosio, Noah A. Rubin, J. P. Balthasar Mueller, and Federico Capasso. Arbitrary spin-to–orbital angular momentum conversion of light. *Science*, 358:896–901, 11 2017.

[101] Marco Piccardo and Antonio Ambrosio. Arbitrary polarization conversion for pure vortex generation with a single metasurface. *Nanophotonics*, 10:727–732, 1 2020.

[102] William R McGehee, Wenqi Zhu, Daniel S Barker, Daron Westly, Alexander Yulaev, Nikolai Klimov, Amit Agrawal, Stephen Eckel, Vladimir Aksyuk, and Jabez J McClelland. Magneto-optical trapping using planar optics. *New J. Phys.*, 23(1):013021, 2021.

[103] Ronald L. Phillips and Larry C. Andrews. Spot size and divergence for Laguerre Gaussian beams of any order. *Appl. Opt.*, 22(5):643–644, Mar 1983.

[104] K.A. Belibassakis and G.A. Athanassoulis. A coupled-mode system with application to nonlinear water waves propagating in finite water depth and in variable bathymetry regions. *Coastal Engineering*, 58(4):337–350, 2011.

[105] Peter Horak and Francesco Poletti. *Multimode Nonlinear Fibre Optics: Theory and Applications*, chapter 1, pages 1–24. IntechOpen, 2012.

[106] Guy Van der Sande, Daniel Brunner, and Miguel C. Soriano. Advances in photonic reservoir computing. *Nanophotonics*, 6(3):561–576, 2017.

[107] Silvia Ortín, Miguel C. Soriano, Ingo Fischer, Claudio R. Mirasso, and Apostolos Argyris. Optical dendrites for spatio-temporal computing with few-mode fibers. *Opt. Mater. Express*, 12(5):1907–1919, May 2022. Publisher: Optica Publishing Group.